

Advanced Vehicle Modelling

7.1 Background

Modern road vehicles are complex machines with a large number of subsystems, sensors, and distributed computing capabilities. Reduced development times, in combination with stringent cost constraints, make product developers increasingly reliant on high-fidelity models and simulation tools. These tools allow engineers to evaluate complete vehicles, vehicle components, or active controllers in complex driving environments.

Typical vehicle models describe the motion of multiple interconnected rigid bodies, and may include flexible components. Flexible finite-element-type modelling methods are often used to describe the chassis or other components of both cars and motorcycles. Common also is the use of model reduction techniques that retain only the modes of interest [245–247]. In many vehicle modelling studies rigid-body models with lumped stiffness suffice; we will confine our consideration to these cases.

The aim of this chapter is to discuss some of the modelling techniques used to replicate the important features of car, motorcycle, and driver dynamics. These more ‘advanced’ vehicle models will include a number of features that were neglected in models described in Chapters 4 and 5, including suspensions with anti-dive and/or anti-squat geometries, environmental influences such as aerodynamic effects, three-dimensional road geometries, and tyre models of the type described in Chapter 3.

We begin in Section 7.2 by discussing car and motorcycle trim conditions. Vehicular trim is of importance in its own right, and as part of the development of linearized models that consider small-perturbation conditions. Included under the ‘trim’ banner are lateral and longitudinal load-transfer, squat, dive, pitch, and roll behaviours. In Section 7.3 we consider three-dimensional road modelling, which is required for modelling all road vehicles. In order to represent roads with sufficient fidelity, and without needless complication, we will base our road modelling on the geometry of *ribbons*. One application of road modelling relates to the solution of optimal control problems such as minimum-time and minimum-fuel problems of the type discussed in Chapter 9. A closely related topic is vehicle positioning on the road, which is a kinematics topic treated in Section 7.4. A car model with a quasi-static suspension model, slipping tyres, and aerodynamics maps suitable for simulation on three-dimensional roads is discussed in Section 7.5. Driver and rider modelling is reviewed in Section 7.6, with a focus on cognitive, stretch-reflex, and passive responses. Section 7.7 addresses the problem of modelling motorcycles, as well as several of their subsystems such as tyres, structural flexibilities, suspensions, and powertrains.

7.2 Vehicle trim

7.2.1 Longitudinal load transfer in cars and motorcycles

The longitudinal load transfer, and acceleration and deceleration limits, of a straight-running vehicle are considered in this section. Formulae that are based on longitudinal and vertical force balances under constant acceleration/braking, and a moment balance around the vehicle's centre of mass, are derived and used to shed light on some of the important issues; see Figure 7.1. Longitudinal and vertical force balances, and a pitch

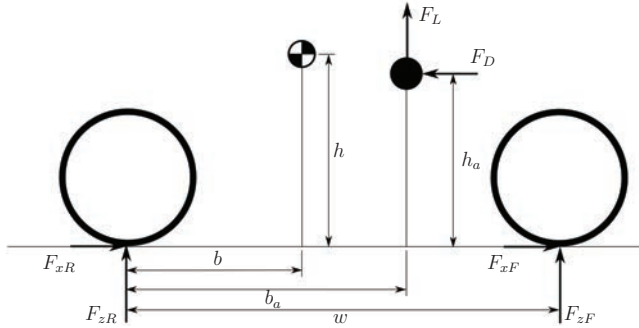


Figure 7.1: Forces acting on an accelerating/braking car.

moment balance, give

$$m\ddot{x}_G = F_{xF} + F_{xR} - F_D \quad (7.1)$$

$$0 = F_{zF} + F_{zR} - mg + F_L \quad (7.2)$$

$$I_F\dot{\omega}_F + I_R\dot{\omega}_R \pm I_e\dot{\omega}_e = F_{zR}b - F_{zF}(w - b) - (F_{xF} + F_{xR})h + F_D(h - h_a) - F_L(b_a - b). \quad (7.3)$$

The mass of the vehicle is m , \ddot{x}_G is the longitudinal acceleration of the vehicle's mass centre, I_F and I_R are the front- and rear-axle spin moments of inertia, $\dot{\omega}_F$ and $\dot{\omega}_R$ are the front- and rear-axle angular accelerations, I_e is the engine spin moment of inertia,¹ $\dot{\omega}_e$ is the engine's spin acceleration, F_D and F_L are the aerodynamic drag and lift forces,² h and h_a are the heights of the mass and aerodynamic centres respectively, w is the wheelbase, and b and b_a are the distances between the rear-axle ground-contact point and the centre of mass and the aerodynamic centre of pressure. The longitudinal

¹ The engine spin axis is assumed parallel to the wheel axles. A positive sign is used when the engine spin direction is the same as that of the road wheels.

² The drag and lift forces are computed using $F_D = \frac{1}{2}\rho C_D A \dot{x}_G^2$ and $F_L = \frac{1}{2}\rho C_L A \dot{x}_G^2$, respectively, where ρ is the density of air; C_D and C_L are the drag and lift coefficients respectively. For cars $C_D A$ is in the range 0.5–1.0 m², A is in the range 1.8–2.2 m², while C_L is between –3 (in the case of high downforce related to wings) and 0.3 [248]; see also Section 7.5.6. In the case of motorcycles, $C_D A$ is in the range 0.3–0.6 m², A is in the range 0.3–0.9 m², and C_L is in the range 0.1–0.2 [6]; see also Section 7.7.5.

forces at the front and rear axles are F_{xF} and F_{xR} respectively. The normal forces on the front and rear axles are F_{zF} and F_{zR} respectively.

Equations (7.1)–(7.3) can be solved for the total longitudinal force $F_x = F_{xF} + F_{xR}$, and the front- and rear-axle vertical loads F_{zF} and F_{zR} respectively:

$$F_x = m\ddot{x}_G + F_D \quad (7.4)$$

$$F_{zF} = mg\frac{b}{w} - m\ddot{x}_G\frac{h}{w} - F_D\frac{h_a}{w} - F_L\frac{b_a}{w} - \frac{I_F}{w}\dot{\omega}_F - \frac{I_R}{w}\dot{\omega}_R \mp \frac{I_e}{w}\dot{\omega}_e \quad (7.5)$$

$$F_{zR} = mg\frac{w-b}{w} + m\ddot{x}_G\frac{h}{w} + F_D\frac{h_a}{w} - F_L\frac{w-b_a}{w} + \frac{I_F}{w}\dot{\omega}_F + \frac{I_R}{w}\dot{\omega}_R \pm \frac{I_e}{w}\dot{\omega}_e. \quad (7.6)$$

The first terms in (7.5) and (7.6) represent the static vertical loads on the axles, the second terms relate to load transfers due to the longitudinal acceleration of the vehicle (and attract a factor of h/w), the third terms are drag-related load-transfer terms (with h_a/w factors), the fourth terms are aerodynamic lift-force load-transfer terms,³ the fifth and sixth terms represent load-transfer effects related to the wheel-spin inertias, and the seventh terms are the load transfer related to the engine-spin inertia. The wheel-spin inertias increase slightly the total load transfer to the rear axle. The engine-spin inertia may either increase (when revving in the wheels' spin direction) or reduce (when rotating in the direction opposite to that of the wheel-spin)⁴ the total load transfer. The terms related to spin-inertia effects are usually small and will be neglected from now on.

In rear-wheel-drive (RWD) vehicles the longitudinal tyre force F_{xR} and dynamic normal load transfer \hat{F}_{zR} at the rear axle (see equation (7.6)):

$$\begin{aligned} \hat{F}_{zR} &= F_{zR} - mg\frac{w-b}{w} \\ &= m\ddot{x}_G\frac{h}{w} + F_D\frac{h_a}{w} - F_L\frac{w-b_a}{w} + \frac{I_F}{w}\dot{\omega}_F + \frac{I_R}{w}\dot{\omega}_R \pm \frac{I_e}{w}\dot{\omega}_e \end{aligned}$$

Negligible

combine to produce a resultant force along the *load-transfer line*, the associated angle with respect to the horizontal is the *load-transfer angle*; see the left-hand side of Figure 7.2. When neglecting aerodynamic forces and spin-inertia influences, the longitudinal tyre force ($m\ddot{x}_G$) and the normal load transfer ($m\ddot{x}_G h/w$) generated under acceleration combine to give a resultant force at the load-transfer angle of

³ Instead of applying F_D and F_L at the aerodynamic centre of pressure, one can apply F_D in the ground plane and two lift forces F_{Lf} and F_{Lr} at the front and rear axle respectively. Equations (7.5) and (7.6) show that

$$F_{Lf} = F_D\frac{h_a}{w} + F_L\frac{b_a}{w} \quad F_{Lr} = -F_D\frac{h_a}{w} + F_L\frac{w-b_a}{w}. \quad (7.7)$$

Note that computing b_a and h_a from F_{Lf} , F_{Lr} , and F_D does not give a unique solution.

⁴ A counter-rotating engine reduces slightly the risk of lifting the front wheel of an accelerating motorcycle [249].

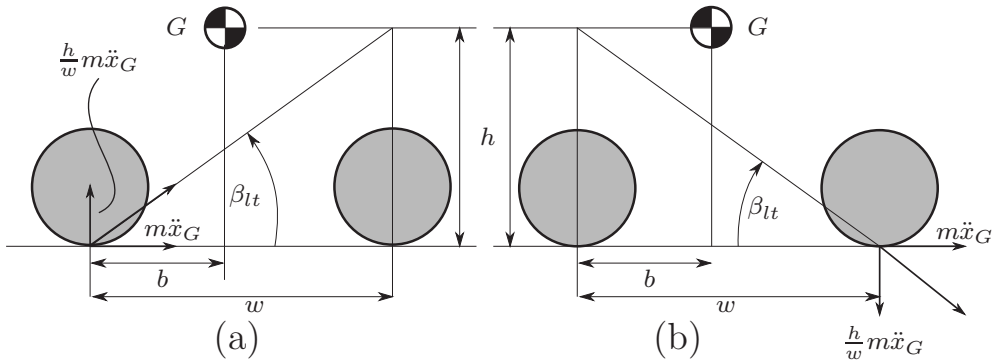


Figure 7.2: Load-transfer line (under acceleration) and the related load-transfer angle β_{tl} in the case that aerodynamic forces are neglected. (a) corresponds to a RWD, while figure (b) corresponds to a FWD vehicle.

$$\beta_{tl} = \arctan \frac{h}{w}. \quad (7.8)$$

The load-transfer line connects the rear-wheel ground-contact point and a point at the height of the centre of mass above the front axle; refer again to the left-hand side of Figure 7.2. In FWD vehicles, the load-transfer line joins the front-wheel ground-contact point and a point at the height of the centre of mass above the rear axle.

In the case of a vehicle under braking, load-transfer lines can be drawn at the front and rear axles, whose inclination angles depend on the force distribution from the front and rear axles; see Figure 7.3. Suppose that the ratio of the front- and rear-axle braking forces is defined as⁵

$$\gamma = \frac{F_{xF}}{F_{xR}}. \quad (7.9)$$

This ratio is called the *brake balance*, or *brake bias*. The load-transfer angles at the front and rear axles are given by

$$\beta_{lt}^R = \arctan \left(\frac{\gamma + 1}{1} \frac{h}{w} \right) \quad \beta_{lt}^F = \arctan \left(\frac{\gamma + 1}{\gamma} \frac{h}{w} \right). \quad (7.10)$$

These load-transfer lines intersect at the height of the centre of mass, and at a distance $\frac{w}{\gamma+1}$ from the rear contact point.⁶ This intersection point is sometimes called the *braking centre* or *acceleration centre* [250], and is located halfway between the axles when $\gamma = 1$, and coincides with the centre of mass when $\gamma = \frac{w}{b} - 1$.

⁵ An alternative definition employed by some authors is $\hat{\gamma} = \frac{F_{xF} F_{xR}}{F_{xF} + F_{xR}} = \frac{\gamma}{\gamma + 1}$.

⁶ In a reference frame centred on the rear-wheel ground-contact point, the rear-axle load-transfer line is described by $z = -\tan \beta_{lt}^R x$, while the front-axle load-transfer line is given by $z = \tan \beta_{lt}^F (x - w)$, with β_{lt}^R and β_{lt}^F given by (7.10). Eliminating z from these equations gives $x = \frac{w}{\gamma+1}$, which when introduced in either the rear or front load lines gives $z = -h$.

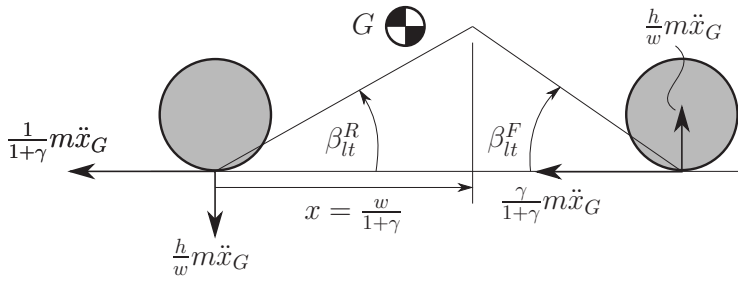


Figure 7.3: Load-transfer lines and related angles β_{tl} under braking (aerodynamic forces neglected).

The peak longitudinal acceleration of a vehicle is limited by the engine power and tyre friction. If we assume for simplicity that all the engine power P_e is used to generate the longitudinal tyre force (i.e. we neglect losses in the powertrain and tyres), we have from (7.4) that

$$\frac{\ddot{x}_G}{g} = \frac{P_e}{mg} \frac{1}{\dot{x}_G} - \frac{F_D}{mg} \quad (7.11)$$

and so the aerodynamic drag F_D reduces the maximum achievable acceleration. Also, given the maximum engine power P_e , the higher the speed \dot{x}_G the lower the achievable maximum acceleration \ddot{x}_G/g (in g s).

The maximum acceleration can also be restricted by the tyre force μF_z ; μ is the friction coefficient and F_z is the tyre normal load. In the case of an AWD vehicle, (7.4) can be rewritten as

$$\frac{\ddot{x}_G}{g} = \mu \frac{F_{zF}}{mg} + \mu \frac{F_{zR}}{mg} - \frac{F_D}{mg}. \quad (7.12)$$

Following the introduction of the normal loads (7.5)–(7.6) into (7.12), one obtains

$$\frac{\ddot{x}_G}{g} = \mu \left(1 - \frac{F_L}{mg} \right) - \frac{F_D}{mg}. \quad (7.13)$$

If the aerodynamic forces are neglected, and the AWD vehicle has both axles engaged at their limits, there holds

$$\frac{\ddot{x}_G}{g} = \mu. \quad (7.14)$$

In the case of a FWD vehicle, the second term on the right-hand side of (7.12) does not apply, and the acceleration limit is

$$\frac{\ddot{x}_G}{g} = \frac{\mu}{w + \mu h} \left(b - \left(h_a + \frac{w}{\mu} \right) \frac{F_D}{mg} - b_a \frac{F_L}{mg} \right). \quad (7.15)$$

In the case of a RWD vehicle, the first term on the right-hand side of (7.12) does not apply, and the acceleration limit becomes

$$\frac{\ddot{x}_G}{g} = \frac{\mu}{w - \mu h} \left(w - b + \left(h_a - \frac{w}{\mu} \right) \frac{F_D}{mg} - (w - b_a) \frac{F_L}{mg} \right). \quad (7.16)$$

A comparison between (7.15) and (7.16) shows that the drag force is detrimental to FWD vehicles, while it is beneficial to the friction-related acceleration limit of RWD vehicles. Aerodynamic lift forces are always detrimental to the acceleration limit. Raising the height of the centre of mass is beneficial to RWD vehicles, while is detrimental to FWD vehicles. The maximum acceleration performance of a RWD vehicle is obtained when the centre of mass is over the rear axle. In general, RWD vehicles have higher friction-related acceleration limits as compared with FWD vehicles.⁷ Not unexpectedly, AWD vehicles are superior to both RWD and FWD vehicles, as shown by (7.13).

Since braking torques are applied to each wheel of most road vehicles, vehicular braking analysis is identical to the acceleration analysis of an AWD vehicle. The friction-related maximum deceleration, under the assumption of optimal engagement of both axles, follows from (7.13) and is given by

$$-\frac{\ddot{x}_G}{g} = \mu \left(1 - \frac{F_L}{mg} \right) + \frac{F_D}{mg}. \quad (7.17)$$

Optimal braking occurs when the longitudinal braking force normalized by the normal load at the front axle, is the same as the longitudinal braking force normalized by the normal load at the rear axle. That is,

$$\frac{F_{xF}}{F_{zF}} = \frac{F_{xR}}{F_{zR}}. \quad (7.18)$$

The optimal brake ratio is obtained by substituting (7.5) and (7.6) into (7.18) to obtain

$$\gamma_{opt} = \frac{b - \frac{\ddot{x}_G}{g}h - \frac{F_D}{mg}h_a - \frac{F_L}{mg}b_a}{w - b + \frac{\ddot{x}_G}{g}h + \frac{F_D}{mg}h_a - \frac{F_L}{mg}(w - b_a)}. \quad (7.19)$$

Since $\ddot{x}_G < 0$ under braking, (7.19) increases as the deceleration increases. That is, the ratio of the front-axle brake force to the rear-axle brake force increases as the severity of braking increases.

Motorcycles typically have independent front and rear brakes and the brake balance is determined by the rider. In most passenger cars the brake balance is fixed and therefore only optimal for some fixed nominal deceleration. For deceleration levels above optimal, the rear axle is over-engaged and oversteering can occur due to high levels of rear-axle tyre slippage. For deceleration levels below optimal, the front axle is over-engaged and understeering can occur. Hard braking in wet conditions may result in front-axle sliding, while hard braking on dry road may result in rear-axle slippage (the tyre friction limit is reached for a deceleration level above optimal).

⁷ If aerodynamic forces are neglected, and we assume that $b = w/2$ for a fair comparison, the ratio of the RWD acceleration limit (7.16) to the FWD acceleration limit (7.15) is $(w + \mu h)/(w - \mu h) > 1$.

In the case of motorcycles, high h/w values lead to large load transfers and it is possible to lift the front wheel under acceleration (the *wheelie*), or lift the rear tyre while braking (the *stoppie*).

The wheelie acceleration limit is computed using (7.5) by setting $F_{zF} = 0$, which gives

$$\frac{\ddot{x}_G}{g} = \frac{b}{h} - \frac{F_D}{mg} \frac{h_a}{h} - \frac{F_L}{mg} \frac{b_a}{h}. \quad (7.20)$$

The aerodynamic drag and lift force reduce the wheelie-related acceleration limit. When the aerodynamic terms are neglected, the acceleration limit is related to the position of the centre of mass, by the b/h factor. High acceleration limits are obtained by moving the centre of mass forwards and downwards, that is, large b and small h . Motorcycles equipped with a low-power engine, or when they are running on a low-friction surface, may not be able to reach the acceleration limit given in (7.20).

The stoppie limit is computed by setting $F_{zR} = 0$ in (7.5), to give

$$-\frac{\ddot{x}_G}{g} = \frac{w-b}{h} + \frac{F_D}{mg} \frac{h_a}{h} - \frac{F_L}{mg} \frac{w-b_a}{h}. \quad (7.21)$$

It is clear that aerodynamic drag increases the stoppie-related deceleration limit, while aerodynamic lift has an opposite effect. When the aerodynamic terms are neglected, the maximum deceleration is related to the position of the centre of mass through the factor $(w-b)/h$. High deceleration limits are obtained by moving the centre of mass rearwards and downwards, that is, large $w-b$ and small h . Motorcycles running on a low-friction surface may not be able to reach the deceleration limit given in (7.21).

In sum, the vehicle's acceleration limit is determined by the engine power (7.11), the tyre friction limit (7.13)–(7.16), or the wheelie limit (7.20), whichever is smallest. The braking limit is set by the braking torque, which is usually large by design, the tyre friction limit (7.17) and the stoppie limit (7.21), whichever is smallest. Better estimates of the acceleration limit can be obtained with more complex models that include the suspension (the suspension may move the mass centre when accelerating or braking). Other influences could include the engine map, the gearbox, and so on.

A number of typical design parameters can be selected on the basis of the above relationships, while neglecting aerodynamic and spin-inertia influences. In this way speed-independent design parameters such as the geometric and inertial quantities may be selected.

Example 7.1 Compute the optimal brake ratio and acceleration limits at 1 m/s and 50 m/s for a motorcycle with $m=275$ kg (including rider), $w=1.50$ m, $b=0.70$ m, $h=h_a=0.65$ m, $C_DA=0.35$ m², $\rho=1.2$ kg/m³ ($F_D=0.5\rho C_DA\dot{x}_G^2$), $C_LA=0$ ($F_L=0.5\rho C_LA\dot{x}_G^2$), $P_e=150$ kW, and $\mu=1.23$. The inverse of the optimal brake ratio (7.19) is shown in Figure 7.4. At high speeds the brake balance at the rear wheel increases significantly as compared with lower-speed scenarios. The engine-related acceleration limits (7.11) are 55g and 0.91g at 1 m/s and 50 m/s respectively, the friction-related acceleration limits are 1.40g and 1.21g (7.16), the wheelie-related acceleration limits are 1.08g and 0.88g (7.20), the friction-related braking limits (7.17) are $-1.23g$ and

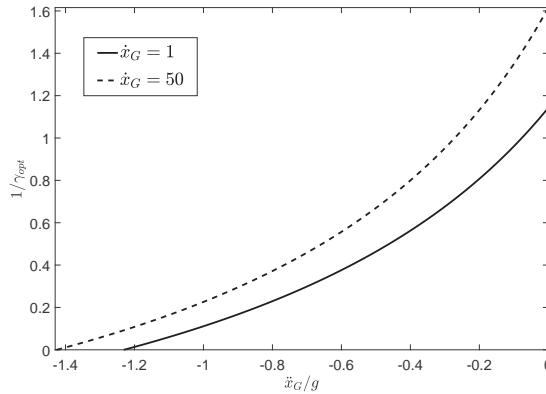


Figure 7.4: Reciprocal of the optimal braking ratio γ_{opt} as a function of the normalized deceleration \ddot{x}_G/g .

$-1.43g$, and the stoppie-related braking limits (7.21) are $-1.23g$ and $-1.43g$ (the friction and stoppie limits coincide in this example, because $\mu = (w - b)/h$ and $h = h_a$).

7.2.2 Squat, dive, and pitch

A vehicle's acceleration determines the load on the front and rear axles (see (7.5) and (7.6)), and these forces will usually be accompanied by suspension travel. The suspension geometry may be designed to reduce this motion, in order to prevent rear-end 'squat' under acceleration (anti-squat behaviour), or front-end 'dive' under braking (anti-dive behaviour). The related fundamentals will be discussed in this section for both cars and motorcycles.

Key quantities used in the analysis of suspension behaviour are *load-transfer lines*, which are given by (7.10) in the case that aerodynamic forces are neglected, and *anti-squat* or *anti-dive* lines (collectively known as *support lines* [250]), which are the lines along which load-transfer forces produce no suspension travel. Sometimes the anti-squat and anti-dive lines/angles are simply called squat and dive lines/angles—hereafter these names should be considered synonymous.

Rear end in motorcycles (chain transmission). We begin our analysis with the rear suspension of an accelerating motorcycle equipped with a chain-drive transmission by studying the equilibrium of the swingarm. Figure 7.5 shows that the moment balance around the swingarm pivot P (the moment due to the weight of the swingarm is neglected, because it is small relative to the other moments) is

$$M_s = F_{zR}l_s \cos \theta - F_{xR}(r_R + l_s \sin \theta) + F_c(r_W - l_s \sin(\theta - \mu_u)), \quad (7.22)$$

in which $M_s = F_s \tau_s$ is the restoring moment produced by the suspension system. The suspension force is F_s , and τ_s is the velocity ratio between the suspension travel and

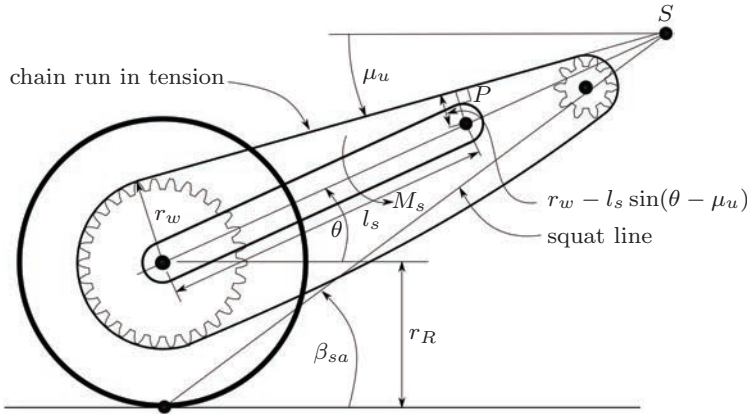


Figure 7.5: Squat angle β_{sa} , squat line, and squat point S in the case of a chain transmission.

the swingarm angular rotation.⁸ The swingarm length is l_s , θ is the swingarm angle, r_R the rear-tyre radius, and F_c is the chain force acting on the upper chain run that has an angle μ_u .⁹ If the rear-wheel spin inertia is neglected, a moment balance around the wheel pivot gives $F_c = F_{xR}r_R/r_w$, which can be substituted into (7.22) to give

$$M_s = F_{zR}l_s \cos \theta - F_{xR}l_s \sin \theta - F_{xR}\frac{r_R}{r_w}l_s \sin(\theta - \mu_u). \quad (7.23)$$

At standstill, when $F_{xR} = 0$, (7.23) simplifies to

$$M_s^{st} = mg\frac{w-b}{w}l_s \cos \theta. \quad (7.24)$$

Subtracting (7.24) from (7.23) gives

$$\hat{M}_s = \hat{F}_{zR}l_s \cos \theta - F_{xR}l_s \left(\sin \theta + \frac{r_R}{r_w} \sin(\theta - \mu_u) \right), \quad (7.25)$$

where $\hat{M}_s = M_s - M_s^{st}$ and $\hat{F}_{zR} = F_{zR} - mg(w-b)/w$ (see (7.6)) are the moment and load variations with respect to static conditions. In the case that $\hat{M}_s = 0$, there is no change in the swingarm trim relative to static conditions. When $\hat{M}_s > 0$ the suspension compresses relative to static conditions, while $\hat{M}_s < 0$ produces an extension of the suspension. In the case $\hat{M}_s = 0$ (7.25) can be rewritten as

$$\frac{\hat{F}_{zR}}{F_{xR}} = \frac{\sin \theta + \frac{r_R}{r_w} \sin(\theta - \mu_u)}{\cos \theta}, \quad (7.26)$$

which defines the anti-squat condition. The tangent of the load transfer angle β_{lt} is given by $\frac{\hat{F}_{zR}}{F_{xR}}$; see Section 7.2.1. When $\hat{M}_s = 0$, the tangent of the anti-squat angle β_{sa} is

⁸ Several motorcycle suspensions will be analysed in Section 7.7.6.

⁹ The kinematic analysis leading to the computation of chain angles will be given in Section 7.7.7.

given by the right-hand side of (7.26). Under the assumption that aerodynamic forces are negligible, the load-transfer angle can be expressed in purely kinematic terms, $\tan \beta_{lt} = h/w$ (7.8). In the case of a chain transmission, the anti-squat line joins the rear contact point and a point S , which is at the intersection of the swingarm centre line and the upper chain line;¹⁰ see Figure 7.6 (a).

In order to monitor the rear suspension behaviour under acceleration, we define the *anti-squat ratio*:¹¹

$$\mathcal{A} = \frac{\tan \beta_{sa}}{\tan \beta_{lt}}. \quad (7.27)$$

The suspension compresses (extends) when $\mathcal{A} < 1$ ($\mathcal{A} > 1$), while retaining its static value when $\mathcal{A} = 1$.

The case of the braking motorcycle is now analysed, with a view to determining the support angle. No suspension motion is obtained when the load-transfer line at the rear wheel during braking is aligned with the support line. Under braking the chain is either slack (the engine is disengaged and the braking effort comes from the rear brake), or the lower chain run is in tension (the engine is ‘braking’ the rear wheel). It should be remembered that with motorcycles, moderate to firm braking must be conducted predominantly on the front wheel, as suggested by (7.19).

When braking with a slack chain (7.22) holds with $F_c = 0$. Subtracting (7.24) from (7.22) gives

$$\hat{M}_s = \hat{F}_{zR} l_s \cos \theta - F_{xR} (r_R + l_s \sin \theta), \quad (7.28)$$

where $\hat{F}_{zR} < 0$ (rear tyre load reduces) and $F_{xR} < 0$ (rear tyre brake force). Solving (7.28) with $\hat{M}_s = 0$ for $\frac{\hat{F}_{zR}}{F_{xR}}$ gives the slack-chain support angle

$$\tan \beta_{sa} = \frac{(r_R + l_s \sin \theta)}{l_s \cos \theta}. \quad (7.29)$$

In this case the support line connects the rear-wheel ground-contact point and the swingarm pivot; see Figure 7.6 (b).

When the lower chain run is in tension, the suspension moment balance (7.22) is

$$M_s = F_{zR} l_s \cos \theta - F_{xR} (r_R + l_s \sin \theta) - F_c (r_w - l_s \sin(\mu_l - \theta)). \quad (7.30)$$

A moment balance around the rear-wheel centre, while neglecting the rear-wheel spin inertia, gives $M_b + F_c r_w + F_{xR} r_R = 0$, where M_b is the rear brake moment (generated by the callipers) and thus (7.30) can be rewritten as

¹⁰ For a reference frame centred on the rear-wheel ground-contact point, the swingarm line is described by $z = -x \tan \theta - r_R$, with the chain line described by $z = -x \tan \mu_u - r_R - r_w / \cos \mu_u$. By eliminating z , one obtains the x -coordinate of the squat point as $x_S = r_w \cos \theta / \sin(\theta - \mu_u)$, which can be substituted into the swingarm line to obtain $z_S = -(r_w \sin \theta + r_R \sin(\theta - \mu_u)) / \sin(\theta - \mu_u)$. The tangent of the anti-squat angle is thus $\tan \beta_{sa} = -z_S / x_S$.

¹¹ Some authors use the term *squat-line* instead of anti-squat line, and define the *squat ratio* as $\mathcal{R} = \tan \beta_{lt} / \tan \beta_{sa}$ [6].

$$M_s = F_{zR}l_s \cos \theta - F_{xR}l_s \left(\sin \theta + \frac{r_R}{r_w} \sin(\mu_l - \theta) \right) + M_b \left(1 - \frac{l_s}{r_w} \sin(\mu_l - \theta) \right). \quad (7.31)$$

Setting $M_b = 0$ (pure engine braking) gives

$$\hat{M}_s = \hat{F}_{zR}l_s \cos \theta - F_{xR}l_s \left(\sin \theta + \frac{r_R}{r_w} \sin(\mu_l - \theta) \right). \quad (7.32)$$

The support line is computed by solving (7.32) with $\hat{M}_s = 0$ for $\frac{\hat{F}_{zR}}{F_{xR}}$ to give the following support angle in the engine-braking case

$$\tan \beta_{sa} = \frac{\sin \theta + \frac{r_R}{r_w} \sin(\mu_l - \theta)}{\cos \theta}. \quad (7.33)$$

In this case the squat point S is at the intersection of the swingarm centre line and the lower chain run line, as can be shown using the arguments given in footnote 10; see Figure 7.6 (c).

In sum, different brake strategies result in different squat point locations and thus different rear-suspension equilibria. Whenever the load-transfer line is below the support line (i.e. when $\beta_{lt}^R < \beta_{sa}$) the rear suspension compresses under braking. Reducing the brake bias (7.9) increases the suspension compression, because β_{lt}^R is reduced.

Rear end in motorcycles (shaft transmissions). The swingarm equilibrium in the case of shaft transmission is similar to the slack-chain case. Subtracting (7.24) from (7.22) with $F_c = 0$ (no chain force) gives

$$\hat{M}_s = \hat{F}_{zR}l_s \cos \theta - F_{xR}(r_R + l_s \sin \theta). \quad (7.34)$$

The related support angle is obtained by solving (7.34) for \hat{F}_{zR}/F_{xR} when $\hat{M}_s = 0$ to give β_{sa} in (7.29). In this case the squat point S is again coincident with the swingarm pivot; see Figure 7.6 (b).

With a typical motorcycle dataset, the anti-squat ratio, when accelerating the vehicle in the shaft transmission case, tends to be significantly greater than one ($\beta_{sa} \gg \beta_{lt}$). Thus large suspension extensions would be experienced with a shaft transmission in combination with a standard swingarm. For this reason, most motorcycles with shaft drive transmissions are equipped with a four-bar linkage in place of a swingarm. In this way squat ratios of approximately unity can be obtained; the squat point is at the intersection of the two rocker extensions; see Fig 7.6 (d).

Rear end in cars. There is a wider variety of suspension layouts in cars as compared with motorcycles. In each case, for small displacements around an equilibrium, the side projection of the suspension motion can be represented as a rotation around an instantaneous velocity centre of a ‘virtual swingarm’ with length l_s . Before going into a detailed analysis, we must distinguish between solid drive (or ‘live’) axles and independent axle suspensions.

The suspension motion of a RWD car with a solid-drive-axle configuration is dynamically equivalent to a motorcycle with a shaft-drive transmission; see Figure 7.7 (a).

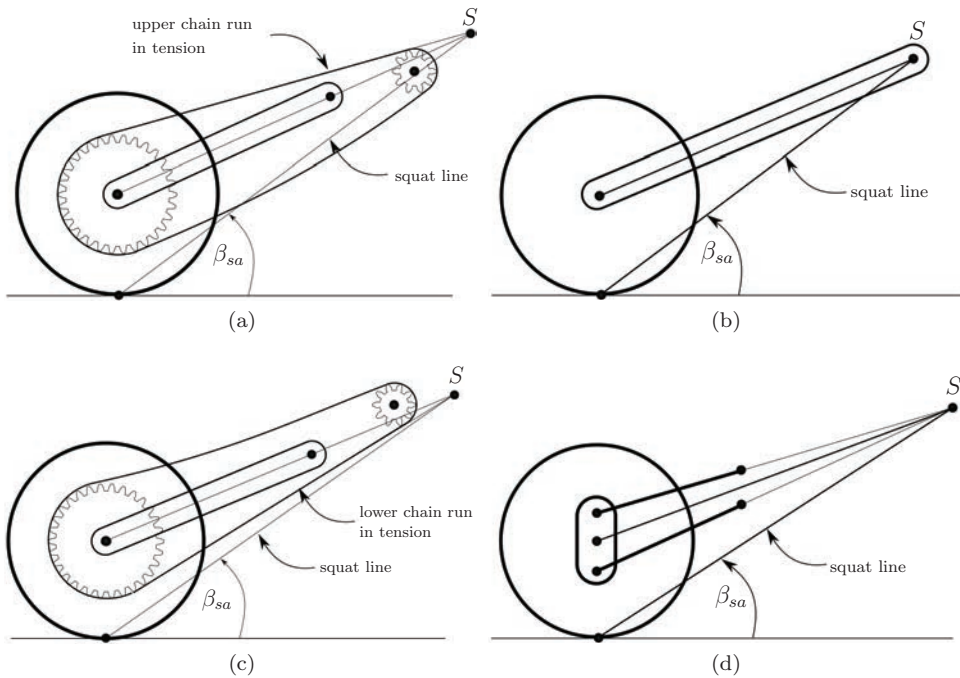


Figure 7.6: Squat line, squat point S , and squat angle β_{sa} in the case of (a) swingarm with upper chain in tension; (b) swingarm with shaft drive; (c) swingarm with lower chain in tension; (d) four-bar linkage with shaft drive.

For that reason (7.34) still applies, with l_s the distance between the wheel centre and the instantaneous velocity centre of the wheel carrier, and the support line joins the rear-wheel ground-contact point and the velocity centre [113, 251]. When the load-transfer line has the same inclination angle as the support line, zero suspension travel is obtained under acceleration.

In the case of a RWD car with an independent suspension, where the differential is attached to the chassis, (7.34) no longer holds and must be replaced by

$$\hat{M}_s = \hat{F}_{zR} l_s \cos \theta - F_{xR} (r_R + l_s \sin \theta) + M_p, \quad (7.35)$$

where M_p is the externally applied propulsive moment. A moment balance around the wheel centre, under the assumption of negligible spin inertia, gives $M_p = F_{zR} r_R$, and (7.35) becomes

$$\hat{M}_s = \hat{F}_{zR} l_s \cos \theta - F_{xR} l_s \sin \theta. \quad (7.36)$$

The inclination of the anti-squat line is obtained from (7.36) when $\hat{M}_s = 0$:

$$\tan \beta_{sa} = \frac{\hat{F}_{zR}}{F_{xR}} = \tan \theta. \quad (7.37)$$

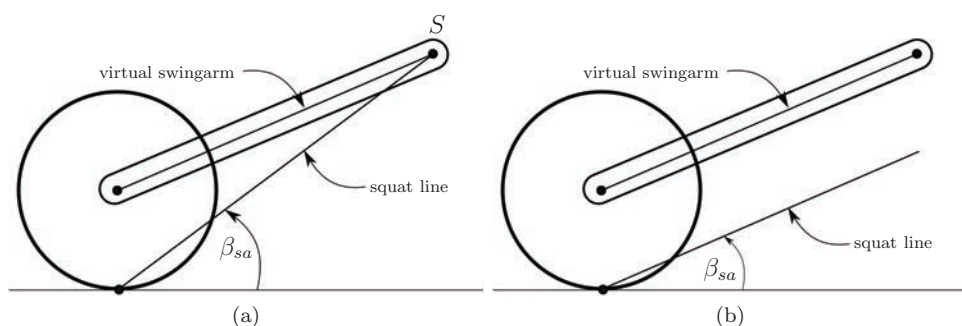


Figure 7.7: Squat line and squat angle β_{sa} in the case of cars with (a) solid axle with a differential mounted on it; (b) independent suspension with the differential mounted on the chassis.

This shows that the anti-squat line is now parallel to the ‘virtual swingarm’; see Figure 7.5. Full anti-squat behaviour, that is, zero suspension travel under acceleration, is obtained when the load-transfer line has the same inclination as the ‘virtual swingarm’. When braking on the front wheel, (7.34) again holds, since the braking moment acts on the wheel and reacts on the unsprung mass (not the chassis) and the support angle is given by (7.29).

Front end in motorcycles. Motorcycles are almost invariably RWD. Under braking, the front suspension of a motorcycle tends to ‘dive’, and the reasoning used when discussing motorcycle rear-end equilibria may again be applied. The support line will lie between the front-wheel ground-contact point and the velocity centre of the front assembly with respect to the chassis.

With a motorcycle equipped with a telescopic front fork, the velocity centre is at infinite distance and the dive line is normal to the sliding axis of the suspension; see Figure 7.8(a). In the case of a motorcycle equipped with a four-bar linkage, such as Duolever (Sections 7.7.6), the velocity centre is at the intersection of the two rocker extensions; Figure 7.8(b).

When the load transfer is along the support line, which in this case is the *dive line*, there is no suspension compression under braking—full anti-dive behaviour is thereby achieved. The anti-dive ratio is defined as the anti-squat ratio in (7.27); a value greater than one is associated with an extension of the suspension. Suspensions such as the Duolever in Figure 7.8(b) can be designed for good anti-dive behaviour, since the location of the rocker extension line intersection can be moved by changing the linkage geometry.

Front end in cars. Again, for small displacements around an equilibrium, the motion of the front wheels projected on the vehicle’s plane of symmetry can be thought of as a rotation around a velocity centre. When accelerating, the solid-axle case and the independent-suspension case must be treated separately. In the first case the support line (often called anti-lift line) connects the velocity centre of the suspended wheel assembly with the ground-contact point, while in the second case the support line

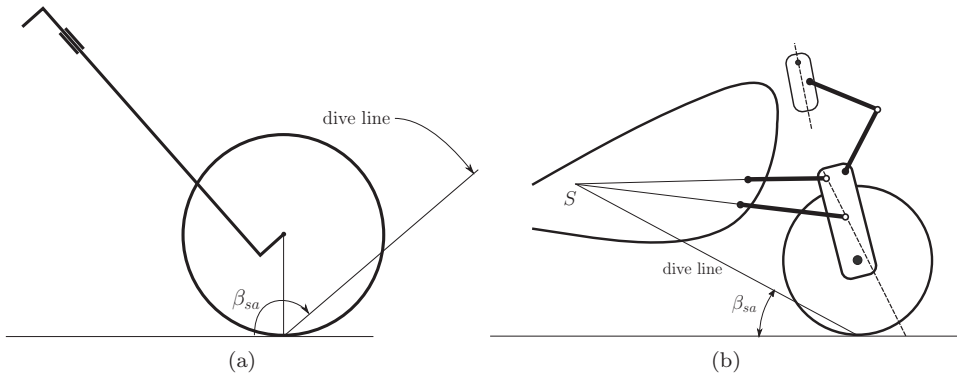


Figure 7.8: Dive line and dive angle β_{sa} in the case of motorcycles with (a) telescopic front fork; (b) four-bar linkage.

is parallel to a virtual swingarm, and through the ground-contact point—the same argument used for the rear wheels. The anti-lift ratio is defined as the anti-squat ratio in (7.27) and a value greater than one is now associated with suspension compression during acceleration. In front-wheel braking the anti-dive line joins the front-wheel ground-contact point and the velocity centre, since the braking torque is internal to the unsprung mass.

Pitch. The equilibrium positions of the front and rear suspensions determine the pitch of the vehicle under acceleration and braking. If \hat{z}_F and \hat{z}_R represent the front- and rear-wheel displacements (with respect to static trim), the pitch is approximately

$$\mu = \frac{\hat{z}_F - \hat{z}_R}{w}; \quad (7.38)$$

$\hat{z} > 0$ is related to suspension extension, and when $\mu > 0$ the vehicle pitches rearwards. For small displacements around a static trim, the suspension elastic moment can be written as $\hat{M}_s \approx -k_\theta \hat{\theta}$, where k_θ is a torsional spring stiffness and $\hat{\theta}$ is the rotation of the (front or rear) virtual swingarm with respect to the static trim. The equivalent vertical stiffness at the rear wheel can be obtained from the equivalence of potential energies

$$\frac{1}{2}k_z \hat{z}^2 = \frac{1}{2}k_\theta \hat{\theta}^2 \rightarrow k_z = k_\theta \left(\frac{1}{l_s \cos \theta} \right)^2, \quad (7.39)$$

where $\hat{z}/\hat{\theta} = l_s \cos \theta$ is the velocity ratio between the vertical travel of the wheel carrier and the rotation of the suspension's virtual swingarm.

We will now consider the pitching behaviour of an accelerating RWD vehicle. The rear-end suspension characteristics depend on the suspension layout, as determined by (7.25), (7.34), or (7.36), but they can all be written in the following common form:

$$-k_{zR} \hat{z}_R = F_{xR} (\tan \beta_{lt} - \tan \beta_{sa}^R), \quad (7.40)$$

where $\tan \beta_{lt}$ is given by (7.8), $\tan \beta_{sa}$ depends on the suspension layout, and (7.39) is used to express \hat{M}_s in terms of \hat{z} . The equilibrium at the front end can be written as

$$k_{zF} \hat{z}_F = F_{xR} \tan \beta_{lt}, \quad (7.41)$$

since $F_{xF} = 0$. This means that the pitch (7.38) of the accelerating RWD vehicle is given by

$$\mu = \frac{F_{xR}}{w} \left(\tan \beta_{lt} \left(\frac{1}{k_{zF}} + \frac{1}{k_{zR}} \right) - \frac{\tan \beta_{sa}^R}{k_{zR}} \right). \quad (7.42)$$

No pitching will occur when

$$\tan \beta_{sa}^R = \left(1 + \frac{k_{zR}}{k_{zF}} \right) \tan \beta_{lt}. \quad (7.43)$$

Observe that full anti-squat systems (i.e. $\beta_{sa}^R = \beta_{lt}$) do not result in pitch-free suspensions. In order to keep the vehicle level, it follows from (7.43) that it is necessary to compensate for front-end lift. If we assume that $k_{zR} \approx k_{zF}$,¹² full anti-pitch behaviour is obtained when $\tan \beta_{sa}^R = 2 \tan \beta_{lt}$.

In the case of an accelerating FWD vehicle, rear-end equilibria are determined by

$$-k_{zR} \hat{z}_R = F_{xF} \tan \beta_{lt}, \quad (7.44)$$

while the front-end equilibria are given by

$$k_{zF} \hat{z}_F = F_{xF} (\tan \beta_{lt} - \tan \beta_{sa}^F). \quad (7.45)$$

Substituting (7.44) and (7.45) into (7.38) gives the pitch of an accelerating FWD vehicle:

$$\mu = \frac{F_{xF}}{w} \left(\tan \beta_{lt} \left(\frac{1}{k_{zF}} + \frac{1}{k_{zR}} \right) - \frac{\tan \beta_{sa}^F}{k_{zF}} \right). \quad (7.46)$$

The zero-pitch condition is

$$\tan \beta_{sa}^F = \left(1 + \frac{k_{zF}}{k_{zR}} \right) \tan \beta_{lt}, \quad (7.47)$$

which again simplifies to $\tan \beta_{sa}^F = 2 \tan \beta_{lt}$ in the case that $k_{zR} \approx k_{zF}$; a zero-lift configuration does not result in zero-pitch behaviour.

¹² Typical values for motorcycles are of the order 20 kN/m, while in cars values range from this figure to an order of magnitude greater in the case of high-downforce race cars.

The pitching behaviour of a braking vehicle is determined by its dive behaviour at the front axle and the lift characteristics of the rear axle. The equilibria at the rear and front axles are determined by

$$k_{zR}\hat{z}_R = -F_{xR}(\tan\beta_{lt}^R - \tan\beta_{sa}^R) \quad (7.48)$$

$$-k_{zF}\hat{z}_F = -F_{xF}(\tan\beta_{lt}^F - \tan\beta_{sa}^F), \quad (7.49)$$

where the load-transfer angles $\beta_{lt}^{R,F}$ are given by (7.10), while the support angles $\beta_{sa}^{R,F}$ depend on the suspension layout. The pitch is again determined using (7.38) to give

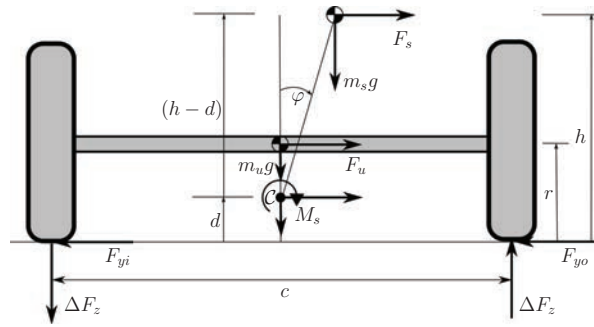
$$\mu = \frac{F_{xF}}{w} \left(\frac{1}{k_{zF}} (\tan\beta_{lt}^F - \tan\beta_{sa}^F) + \frac{1}{\gamma k_{zR}} (\tan\beta_{lt}^R - \tan\beta_{sa}^R) \right); \quad (7.50)$$

full anti-pitch behaviour is obtained when $\mu = 0$.

Example 7.2 Suppose a car has wheelbase $w = 2.5$ m, mass $m = 1,300$ kg, centre-of-mass height $h = 0.50$ m, and front- and rear-wheel radii $r_F = r_R = 0.30$ m. The equivalent vertical spring stiffnesses at the rear and front axles are $k_{zR} = 35$ kN/m and $k_{zF} = 25$ kN/m. The rear and front suspension virtual pivots are located at height $h_{SR} = h_{SF} = 0.37$ m from ground, while the distances from the rear and front axles are $b_{SR} = a_{SF} = 0.70$ m respectively, and the braking ratio is $\gamma = 60/40$. Compute the anti-squat, anti-lift, and anti-dive ratios and pitch angle when accelerating/braking at $\ddot{x}_G = \pm 0.5$ g, in the case of RWD and FWD vehicles, in the case of solid ‘live’ axles and independent suspensions. Neglect aerodynamic influences. For both RWD and FWD vehicles the load-transfer angle under acceleration is $\tan\beta_{lt} = 0.2$ using (7.8). The longitudinal force under acceleration is $m\ddot{x}_G = 6377$ N. The support angle of the accelerating RWD car is $\tan\beta_{sa} = 0.53$ from (7.29) in the case of ‘live’ axles and $\tan\beta_{sa} = 0.1$ using (7.37) in the case of independent suspensions, which gives anti-squat ratios of 264% and 50% respectively using (7.27). The corresponding pitch angles are -0.2° and $+1.6^\circ$ using (7.42). Since $b_{SR} = a_{SF}$ and $h_{SR} = h_{SF}$, the support angles of the accelerating FWD car are identical to those of the accelerating RWD vehicle. Therefore the anti-lift ratios are 264% and 50% respectively with the corresponding pitch angles given by -1.1° and $+1.4^\circ$; see (7.46). When braking with both RWD and FWD, the load-transfer angles (7.10) at the rear and front axles are $\tan\beta_{lt}^R = 0.50$ and $\tan\beta_{lt}^F = 0.33$ respectively, while the support angles are $\tan\beta_{sa}^R = \tan\beta_{sa}^F = 0.53$. The configuration is 159% anti-dive at the front and 106% anti-lift at the rear—this is an extreme scenario. The braking force is -6377 N. The pitch angle (7.50) is 0.7° .

7.2.3 Lateral load transfer in cars

The lateral load transfer and acceleration limit of a vehicle under steady turning (i.e. constant speed V and constant lateral acceleration $a_y = V^2/R$, where R is the cornering radius) will be considered in this section. We will begin by considering a single axle before progressing to the whole vehicle. We will develop the idea of a *roll centre* (for a single axle), and then the notion of a *roll axis* for the whole car. We will consider force and kinematic interpretations of the roll centre. We will assume that the sprung part of the car (i.e. everything ‘above’ the suspension; the main chassis) rolls through a

Figure 7.9: Force interpretation of the roll centre \mathcal{C} .

small angle with respect to the unsprung mass (i.e. everything ‘below’ the suspension; the front and rear axle and wheel assemblies). From a modelling perspective, we will assume that the sprung mass is joined to the unsprung mass through revolute joints at the front- and rear-axle roll centres. The front-wheel steering angle will be assumed negligible throughout the analysis.

Roll centre—force interpretation. In the force interpretation, the roll centre is defined as a point in the vertical plane above the wheel centres on a given axle, to which the application of a lateral force produces no suspension roll. In order to develop this idea we will make use of Figure 7.9, which shows the roll centre position in a left-hand turn when viewed from the rear; the wheel axle and tyres are assumed rigid.

The car’s lateral acceleration a_y produces lateral forces on the sprung and unsprung masses given by

$$F_s = a_y m_s$$

$$F_u = a_y m_u$$

respectively; m_s and m_u are the car’s sprung and unsprung masses respectively. The force on the sprung mass can be moved to the roll centre \mathcal{C} by introducing the suspension moment

$$M_s = m_s(h-d)(a_y + g\varphi) \quad (7.51)$$

in which d and h are the heights of the roll centre and sprung mass respectively.

A moment balance around the projection of \mathcal{C} on the ground shows that the load transfer has three terms that relate to the unsprung-mass lateral force, the sprung-mass lateral force, and the correcting moment M_s as given by

$$\Delta F_z = \frac{F_u r}{c} + \frac{F_s d}{c} + \frac{M_s}{c} \quad (7.52)$$

$$= \frac{F_u r}{c} + \frac{F_s h}{c} + \frac{m_s g(h-d)\varphi}{c}. \quad (7.53)$$

As the wheel radius r increases, the load transfer due to the unsprung mass increases; in some analyses the influence of the unsprung mass is neglected. As the height of the

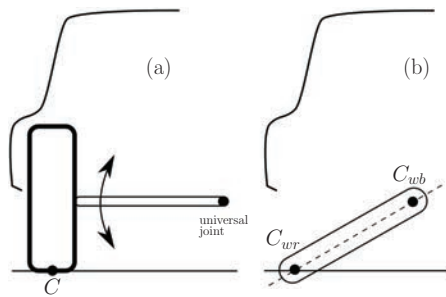


Figure 7.10: Roll centre in the case of a primitive rear suspension.

sprung mass centre increases, the load transfer due the sprung mass increases. The car rolls towards the outside of the turn when the mass centre of the sprung mass is above the roll centre, there is no roll when the mass centre is at the roll centre, and the car rolls towards the inside of the turn when the mass centre of the sprung mass is below the roll centre.

Roll centre—kinematic interpretation. In the kinematic interpretation the roll centre is the instantaneous centre of rotation of the sprung mass with respect to the ground, or alternatively the centre of rotation of the unsprung mass with respect to the sprung mass when a pure moment is applied on the unsprung mass. Consider the simple (swing-axle) suspension system illustrated in Figure 7.10. In the (a) part of the figure we see the left-hand suspension rotating about a universal joint that is fixed to the differential, which in turn is fixed to the car body. The universal joint (replaceable by a revolute joint in this two-dimensional analysis) moves so as to keep the wheel in contact with the ground. In the (b) part of the figure the suspension, wheel, and wheel carrier are abstracted as a link that has instantaneous centres of rotation C_{wr} and C_{wb} . Centre C_{wr} is a point fixed in the road about which the wheel-axle unit rotates, which is usually assumed to be in the centre of the tyre contact patch. The link is also pinned to the differential and the car body and rotates around the point C_{wb} . We want to know the instantaneous centre C_{br} of the car body with respect to the road. The Aronhold–Kennedy theorem [252] says that this third instantaneous centre lies on the straight line joining C_{wr} and C_{wb} . By symmetry, the roll centre is at the intersection of this line and the car's vertical longitudinal plane of symmetry.

By making use of these ideas, the roll centres of a MacPherson, and a double-wishbone suspension can be found, as shown in Figure 7.11. The instantaneous centre of rotation of the wheel and wheel carrier in the road is the ground-contact point C , while the instantaneous centre of rotation of the wheel and wheel carrier in the car body is S . The car's roll centre is the intersection point of the line through C and S and the car's longitudinal plane of symmetry.

Car roll centre. In this section we extend the axle-based notion of a roll centre to the entire car. Let us now assume that the vehicle's sprung mass is joined to the front and rear unsprung masses through two revolute joints, whose common axis of rotation is called the *roll axis* of the sprung mass. For present purposes the car's roll

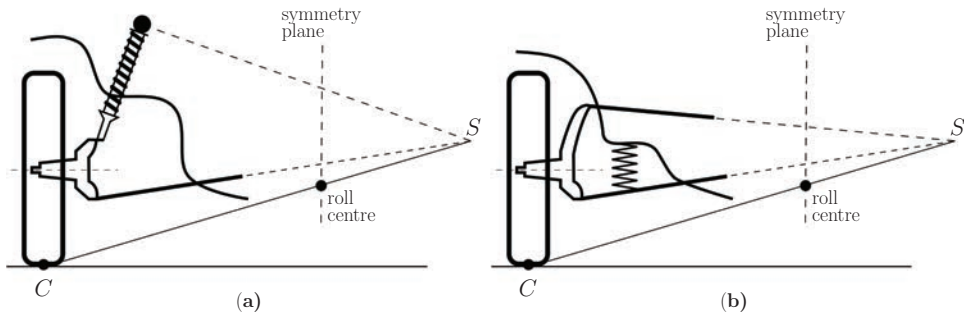


Figure 7.11: Roll centre in the case of (a) MacPherson strut and (b) double-wishbone suspension.

axis is assumed to pass through the roll centres of the front and rear axles. Referring to Figure 7.12, the roll axis has height d_F and d_R above the front and rear axles respectively, and height

$$d = \frac{d_F b + d_R (w - b)}{w} \quad (7.54)$$

above the projection of the mass centre of the sprung mass onto the ground plane.

Under the assumption that the roll angle φ and the roll axis inclination angle α are both small, a moment balance around C gives

$$ma_y (h - d) = (K - mg(h - d)) \varphi, \quad (7.55)$$

where m is the sprung mass (usually approximately the mass of the car; herein assumed equal), h is the height of the centre of mass, and K is the roll stiffness of the whole suspension system, which arises from the parallel combination of the front suspension stiffness K_F and rear suspension stiffness K_R :

$$K = K_F + K_R. \quad (7.56)$$

Equation (7.55) can be solved for the car roll angle

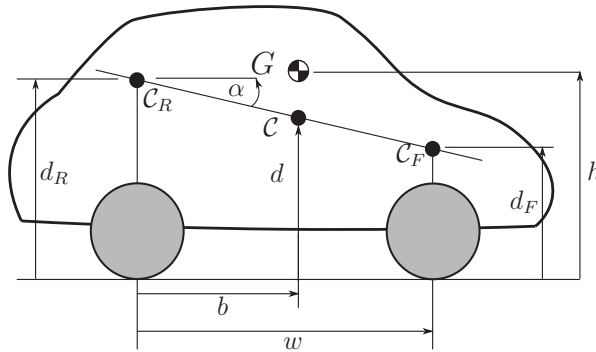


Figure 7.12: Car model for lateral load transfer.

$$\varphi = ma_y \frac{h-d}{K - mg(h-d)} = ma_y \frac{h-d}{\tilde{K}}, \quad (7.57)$$

where \tilde{K} is the effective roll stiffness; we will again assume that $\tilde{K} \approx K$. Another related index is the roll rate, which is defined as $\partial\varphi/\partial a_y = m(h-d)/\tilde{K}$.

Moment balances for the front and rear unsprung masses with respect to the points C_F and C_R on the roll axis are

$$K_F\varphi = \Delta F_{zF}c_F - F_{yF}d_F \quad (7.58)$$

$$K_R\varphi = \Delta F_{zR}c_R - F_{yR}d_R, \quad (7.59)$$

in which c_F and c_R are the front- and rear-wheel track widths respectively, ΔF_{zF} and ΔF_{zR} are the front and rear lateral load transfers respectively, and F_{yF} and F_{yR} are the front and rear lateral forces, that is, $F_{yF} = F_{yFo} + F_{yFi}$ and $F_{yR} = F_{yRo} + F_{yRi}$, where ‘i’ and ‘o’ mean inner and outer respectively.¹³ A lateral force balance together with a moment balance around the centre of mass give

$$F_{yF} = ma_y \frac{b}{w} \quad (7.60)$$

$$F_{yR} = ma_y \frac{w-b}{w}. \quad (7.61)$$

When substituting (7.57), (7.60), and (7.61) into (7.58) and (7.59) one obtains

$$\Delta F_{zF} = ma_y \left(\frac{K_F}{K} \frac{h-d}{c_F} + \frac{d_F}{c_F} \frac{b}{w} \right) \quad (7.62)$$

$$\Delta F_{zR} = ma_y \left(\frac{K_R}{K} \frac{h-d}{c_R} + \frac{d_R}{c_R} \frac{w-b}{w} \right). \quad (7.63)$$

The first terms on the right-hand sides relate to the roll stiffness distribution between the front and rear axles; the second terms are geometric.

The total lateral load transfer is computed by combining the front and rear load transfers in (7.62) and (7.63) to give

$$\Delta F_{zR}c_R + \Delta F_{zF}c_F = ma_y h, \quad (7.64)$$

or

$$\Delta F_z = ma_y \frac{h}{\tilde{c}} \quad (7.65)$$

with

$$\tilde{c} = \frac{\Delta F_{zR}c_R + \Delta F_{zF}c_F}{\Delta F_z}. \quad (7.66)$$

The constant \tilde{c} is the equivalent wheel track width, with $\Delta F_z = \Delta F_{zR} + \Delta F_{zF}$ (in the case that $c_F = c_R = c$, $\tilde{c} = c$).

¹³ An uneven lateral force distribution between the inner and outer tyre on an axle does not affect the derivation, since only the total lateral force on the axle matters.

To summarize, the total lateral load transfer is independent of the roll stiffness and depends only on the h/\bar{c} ratio; a reduced load transfer is obtained by lowering the car's mass centre and/or widening the car's track width. The load-transfer distribution between the front and rear axles is determined by the front and rear roll stiffness and some geometric parameters; harder suspensions lead to higher roll stiffness.

Jacking. The lateral forces on the inner and outer tyres of an axle need not be equal. Suppose that the outer lateral tyre force is given by $F_{yo} = \bar{F}_y + \Delta F_y$, while the inner lateral tyre force is given by $F_{yi} = \bar{F}_y - \Delta F_y$, where $\bar{F}_y = (F_{yo} + F_{yi})/2$. This lateral force difference is associated with the possible 'lifting' of cars fitted with independent suspensions as a consequence of lateral load transfer (e.g. when turning); this effect is called *suspension jacking*. Taking moments around the velocity centre of the outer wheel carrier (see Figure 7.11) gives

$$\begin{aligned}\hat{M}_{so} &= \Delta F_z b_{RC} - (\bar{F}_y + \Delta F_y) h_{RC} \\ &= (\Delta F_z b_{RC} - \bar{F}_y h_{RC}) - \Delta F_y h_{RC},\end{aligned}\quad (7.67)$$

where \hat{M}_{so} is the outer-suspension elastic moment relative to static conditions (positive in compression). The quantities b_{RC} and h_{RC} are the lateral distance and height of the roll centre with respect to the tyre contact point. Similarly, for the inner wheel,

$$\hat{M}_{si} = (\Delta F_z b_{RC} - \bar{F}_y h_{RC}) + \Delta F_y h_{RC}, \quad (7.68)$$

where \hat{M}_{si} is the inner-suspension elastic moment (negative in compression). The first components in (7.67) and (7.68) are associated with the roll motion (identical for both suspensions), while the second component is associated with *jacking*, which results in both an extension of suspension and a reduction in the vehicle's track width.

Lateral acceleration limit. We will now show that lateral load transfer is detrimental to a car's steady-cornering performance. A lateral force balance gives

$$\begin{aligned}ma_y &= (F_{yFo} + F_{yRo}) + (F_{yFi} + F_{yRi}) \\ &= F_{yo} + F_{yi},\end{aligned}\quad (7.69)$$

where the F_{yo} s represent the lateral forces due to the outside tyres, while the F_{yi} s represent the lateral forces due to the inside tyres. The lateral force depends on the road-tyre friction coefficient μ and normal load; the friction coefficient usually reduces with the load, see equation (3.96). Under static conditions, the normal load F_z is split equally between the outer and inner pairs of tyres; longitudinal symmetry will be assumed here and so $F_{zo} = F_{zi} = F_z/2$. Equation (7.69) can be rewritten as

$$ma_y = \mu F_{zo} + \mu F_{zi} \quad (7.70)$$

$$\begin{aligned}&= \mu_0 (1 - \alpha \Delta F_z) \left(\frac{F_z}{2} + \Delta F_z \right) + \mu_0 (1 + \alpha \Delta F_z) \left(\frac{F_z}{2} - \Delta F_z \right) \\ &= \mu_0 (F_z - 2\alpha (\Delta F_z)^2),\end{aligned}\quad (7.71)$$

where μ_0 is the friction coefficient at nominal load and ΔF_z is the total lateral load transfer in (7.65); the lateral load transfer ΔF_z always reduces the maximum lateral acceleration:¹⁴

$$a_y = \frac{\mu_0(F_z - 2\alpha(\Delta F_z)^2)}{m}. \quad (7.72)$$

In the case that the friction coefficient is not load dependent, the lateral load transfer has no effect on the maximum lateral acceleration. In the case that aerodynamic loading is negligible (i.e. $F_z = mg$), the maximum acceleration expression becomes

$$\frac{a_y}{g} = \mu_0. \quad (7.73)$$

In other words, the tyre–road friction coefficient determines the maximum theoretical achievable lateral acceleration of the car.¹⁵ Note that the same results have been obtained for the friction-related deceleration limit (7.14)

Cars with a large h/c ratio may have their lateral acceleration limited by *rollover* rather than the tyre friction limit (7.73). This limit may be estimated quasi-statically by taking limits around the heavily loaded tyre ground-contact point, while assuming no normal load on the other tyre. Setting $\Delta F_z = mg/2$ and $\tilde{c} = c$ in (7.65) gives

$$\frac{a_y}{g} = \frac{c}{2h}, \quad (7.74)$$

which shows that a large track width c and low mass-centre height h reduce the rollover propensity. More precise estimates of rollover limits can be obtained by modelling the suspension, steering, tyres, and road banking under dynamic conditions. Special attention must be given to rollover induced by a tyre hitting an object such as a curb—the so-called *tripped* conditions [113, 253, 254].

Example 7.3 Suppose a car with has wheelbase $w = 2.5$ m, mass $m = 1,300$ kg, centre-of-mass height $h = 0.5$ m, distance of mass centre from the rear axle $b = 1.3$ m, track width $c = c_F = c_R = 1.6$ m, roll stiffness balance $K_F/K = 0.55$, front-axle roll stiffness $K_F = 33$ kNm/rad, roll axis height $d = d_F = d_R = 0.1$ m, tyre friction coefficient $\mu_0 = 1$, and $\alpha = 10^{-4} \text{ N}^{-1}$. Compute the lateral load transfer under steady turning with a lateral acceleration of $a_y = 0.5$ g. The normal load on each of the front tyres is 3,314 N, while that on the rear tyres is 3,060 N; use half of the first components on the right-hand sides of (7.5) and (7.6). The total lateral load transfer is 1,992 N (7.65); the lateral load transfer on the front axle is 1,087 N (7.62) while that on the rear axle is 905 N (7.63). The roll angle of the car is $\varphi = 2.7^\circ$ (7.57) and the roll rate is $\partial\varphi/\partial a_y = 5.3^\circ/\text{g}$. The lateral acceleration limit is $a_y = 0.83$ g and is given by (7.72) and (7.65)—in this condition $\Delta F_z = 3,303$ N. This figure becomes $a_y = 1$ g (7.73) in the case that the tyre friction coefficient is not load dependent.

¹⁴ The coefficient α is related to p_{y4} in (3.96) by $\alpha = -p_{y4}/p_{y3}F_{z0}$, where $p_{y3} = \mu_0$ and $p_{y4} < 0$ are the coefficients related to the outer or inner pairs of tyres, while $F_{z0} = F_{zo} = F_{zi}$.

¹⁵ We call this lateral acceleration ‘theoretical’, because it assumes that all the tyres reach the friction limit simultaneously. In practice the first tyre that reaches the friction limit sets the maximum acceleration limit.

7.2.4 Roll trim in motorcycles

The equilibrium roll angle of a motorcycle under steady turning conditions, that is, a constant speed V and constant lateral acceleration a_y , is considered next. To keep the analysis simple, aerodynamic and gyroscopic influences are neglected, and the front and rear tyres are assumed aligned with the central plane of the chassis.

Referring to the left-hand part of Figure 7.13, in the case of thin-disk tyres, a moment balance around the ground-contact point is

$$0 = -ma_y h \cos \varphi + mgh \sin \varphi, \quad (7.75)$$

where $a_y = V^2/R_G$ is the lateral acceleration; and V the velocity of the vehicle's mass centre and R_G the distance between the centre of mass and the centre of the turn. The height of the centre of mass is h , φ is the roll angle, m is the mass of the vehicle and rider, and g is the gravity. Equation (7.75) can be solved for the equilibrium roll angle to give

$$\varphi_0 = \arctan \frac{a_y}{g}. \quad (7.76)$$

In the case of finite-width tyres with crown radius $\rho_F = \rho_R = \rho$, the roll balance becomes

$$0 = -ma_y (\rho + (h - \rho) \cos \varphi) + mg (h - \rho) \sin \varphi, \quad (7.77)$$

which can be written in the standard form

$$A \sin x + B \cos x + C = 0. \quad (7.78)$$

The various constants are given by

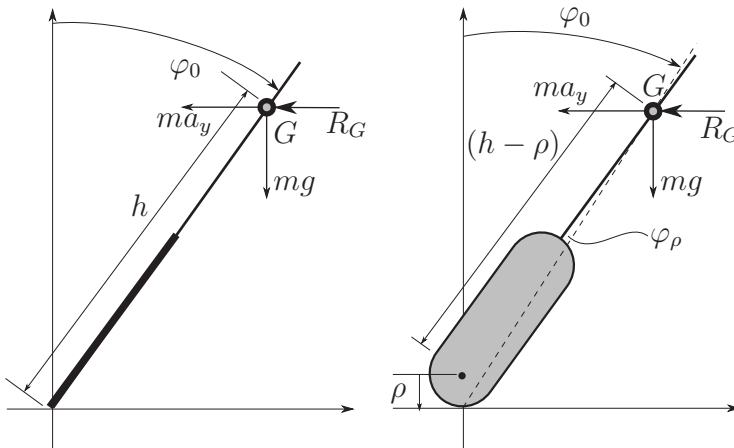


Figure 7.13: Motorcycle models for roll trim: thin-disk tyre (left) and finite-width toroidal tyre (right).

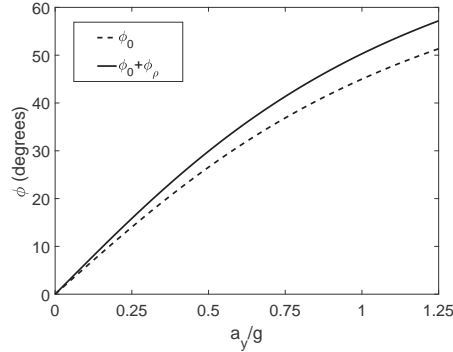


Figure 7.14: Roll angle as a function of the lateral acceleration in the case of thin-disk tyres (dashed line) and finite-width tyres (solid line). The parameters used are $\rho = 0.075 \text{ m}$ and $h = 0.650 \text{ m}$.

$$A = mg(h - \rho) \quad B = -ma_y(h - \rho) \quad C = -ma_y\rho \quad x = \varphi. \quad (7.79)$$

Equation (7.78) has solution¹⁶

$$\begin{aligned} \varphi &= \arctan \frac{a_y}{g} + \arcsin \frac{a_y \rho}{(h - \rho) \sqrt{g^2 + a_y^2}} \\ &= \varphi_0 + \varphi_\rho. \end{aligned} \quad (7.81)$$

A comparison between (7.76) and (7.81) shows that for a given lateral acceleration a_y , the roll angle increases as the tyre crown radius increases; see Figure 7.14. The equilibrium roll angle is independent of the height of the loaded vehicle mass centre (motorcycle plus rider) in the case of thin-disk tyres. In the case of finite-width tyres, the roll angle increases as the mass-centre height reduces.

¹⁶ The solution is obtained normalizing by $\sqrt{A^2 + B^2}$ and introducing the variable β as follows:

$$\begin{aligned} \frac{A}{\sqrt{A^2 + B^2}} \sin x + \frac{B}{\sqrt{A^2 + B^2}} \cos x &= \frac{-C}{\sqrt{A^2 + B^2}} \\ \cos \beta \sin x + \sin \beta \cos x &= \frac{-C}{\sqrt{A^2 + B^2}} \\ \sin(x + \beta) &= \frac{-C}{\sqrt{A^2 + B^2}} \end{aligned}$$

which has solution

$$\begin{aligned} x &= -\beta + \arcsin \frac{-C}{\sqrt{A^2 + B^2}} \\ &= \arctan(-B, A) + \arcsin \frac{-C}{\sqrt{A^2 + B^2}}. \end{aligned} \quad (7.80)$$

We conclude this section by noting that in steady-state cornering the vehicle weight and the centrifugal force combine to produce a suspension load of $mg/\cos\varphi > mg$, and thus an additional suspension compression is expected under cornering.

7.3 Road modelling

Road models are required in a number of applications areas including virtual reality environments, transportation management and planning systems, and automated vehicle navigation systems. These models are also required in vehicular optimal control problems so that road-related path constraints can be incorporated into the problem [120, 255]. Road-related path constraints are enforced by ensuring that the vehicle remains in contact with the road and that its mass centre, or its road wheels, remain within the track boundaries. In the treatment given here *ribbons* or *strips* are central to our road models and provide a differential-geometric description of general navigable road surfaces [256]. We will assemble a number of geometric ideas that will be used to describe three-dimensional roads. All of these concepts can be found in the classical differential geometry literature; see for example [257–259]. We will also make use of the properties of rotating frames as given in Section 2.5.

7.3.1 Three-dimensional curves

Consider the parametric representation of the *arc of a curve*

$$\mathcal{C} = \{ \mathbf{x}(s) = [x(s) \ y(s) \ z(s)]^T \in \mathbb{R}^3 : s \in [s_0, s_f] \}, \quad (7.82)$$

in which the parameter s is the *arc length* of \mathcal{C} . We assume that each element of $d^3\mathbf{x}/ds^3$ is continuous and that $d^2\mathbf{x}/ds^2$ is not identically 0 for any s . The curve is deemed *simple* if any point on the curve corresponds to a single value of s .

A *moving trihedron* associated with \mathcal{C} is defined by a triple of unit vectors $\mathbf{t}(s)$, $\mathbf{p}(s)$, and $\mathbf{b}(s)$ that form a right-handed coordinate system with (moving) origin $\mathbf{x}(s)$. The unit vector \mathbf{t} is tangent to \mathcal{C} and is defined by $\mathbf{t} = \mathbf{x}'$; the prime represents a derivative with respect to the arc length s . Since $\mathbf{t} \cdot \mathbf{t} = 1$, $\mathbf{t} \cdot \mathbf{t}' = 0$ and so \mathbf{t}' is orthogonal to \mathbf{t} . The unit vector \mathbf{p} is the *principal normal* to \mathcal{C} and is defined as $\mathbf{p} = \mathbf{t}'/|\mathbf{t}'|$. The unit vector \mathbf{b} is called the *binormal* to the curve and is defined by the vector product $\mathbf{b} = \mathbf{t} \times \mathbf{p}$. A pictorial representation of \mathcal{C} and its moving trihedron is shown in Figure 7.15. The *curvature vector* of \mathcal{C} is defined as the rate of change of the tangent vector, $\boldsymbol{\kappa} = \mathbf{t}'$. The *curvature* is the scalar product $\kappa = \boldsymbol{\kappa} \cdot \mathbf{p}$, which is a measure of the deviation of \mathcal{C} from a straight line; it follows that $\boldsymbol{\kappa} = \kappa\mathbf{p}$, where $\kappa = |\mathbf{t}'|$. The *radius of curvature* is defined as $\rho = 1/\kappa$. The *centre of curvature* is given by $\mathbf{c} = \mathbf{x} + \rho\mathbf{p}$. The *torsion* of \mathcal{C} measures the direction and extent to which the curve deviates from its *osculating plane* $\mathbf{t} \mathbf{p}$. The torsion is defined as $\tau = -\mathbf{p} \cdot \mathbf{b}'$.

The orientation of the moving trihedron is defined by the three-dimensional rotation matrix

$$\mathcal{R} = [\mathbf{t} \ \mathbf{p} \ \mathbf{b}]. \quad (7.83)$$

The curvature and torsion define the *angular rate* of the moving trihedron through the kinematic equations known as the *Frenet–Serret formulae*

$$\mathcal{R}' = \mathcal{R} \begin{bmatrix} 0 & -\kappa & 0 \\ \kappa & 0 & -\tau \\ 0 & \tau & 0 \end{bmatrix} = \mathcal{R}S(\boldsymbol{\Omega}^C); \quad (7.84)$$

which is obtained using (2.169), with the skew-symmetric matrix S defined in (2.154) and $\boldsymbol{\Omega}^C$ the moving trihedron's angular rate (in radians per metre and *not* radians per second!). Using (2.146), each column of (7.84) can be interpreted kinematically as $\mathbf{v} = \boldsymbol{\Omega}^C \times \mathbf{x}$, where \mathbf{x} is a position of the origin of the moving trihedron. By direct calculation using (7.83) and (7.84), $\mathbf{t}' = \kappa\mathbf{p}$, $\mathbf{p}' = \tau\mathbf{b} - \kappa\mathbf{t}$, and $\mathbf{b}' = -\tau\mathbf{p}$.

The angular rate vector of the moving trihedron is known as the *Darboux* vector and is given by

$$\boldsymbol{\Omega}^C = \tau\mathbf{t} + \kappa\mathbf{b}. \quad (7.85)$$

Once the curvature vector $\boldsymbol{\Omega}^C$ is given as a function of the curvilinear abscissa s , by imposing initial conditions on the position $\mathbf{x}(s_0)$ and the orientation $\mathcal{R}(s_0)$, the curve \mathcal{C} is generated by

$$\begin{cases} \mathcal{R} = \int_{s_0}^s \mathcal{R}' ds, \\ \mathbf{x} = \int_{s_0}^s \mathbf{t} ds, \end{cases} \quad (7.86)$$

in which \mathbf{t} is the first column of \mathcal{R} in (7.83).

7.3.2 Ribbons

We will represent the road by a geometric object called a *ribbon*, which can be created by augmenting the curve \mathcal{C} with notions of ‘width’ and ‘twist’. Both of these quantities will be defined in terms of a unit *camber* vector \mathbf{n} , which lies in the plane of the ribbon

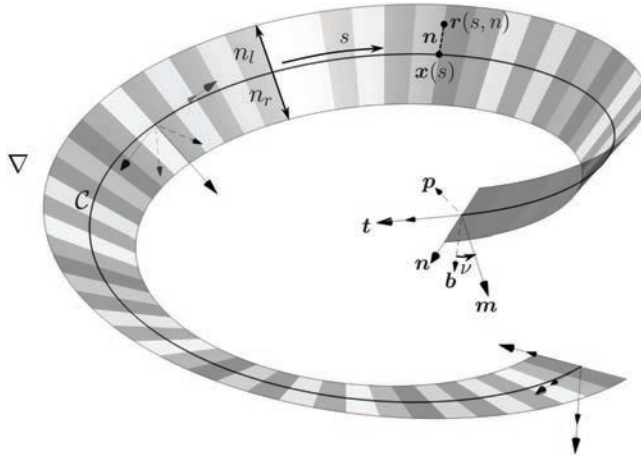


Figure 7.15: A road represented by a ribbon ∇ that is generated by a spine curve \mathcal{C} .

and is orthogonal to the tangent vector \mathbf{t} ; see Figure 7.15. We will represent the ribbon parametrically as:

$$\nabla = \{\mathbf{r}(s, n) = \mathbf{x}(s) + \mathbf{n}(s)n \in \mathbb{R}^3 : s \in [s_0, s_f], n \in [n_l(s), n_r(s)]\}, \quad (7.87)$$

in which \mathbf{x} is the ribbon's *spine curve*, s is the arc length, and n is the lateral offset in the ribbon plane; the origin of the moving trihedron travels along \mathbf{x} . The left- and right-hand road boundaries are described by n_l and n_r respectively. Lateral displacements on the ribbon surface are measured from the spine in the direction of unit vector \mathbf{n} . The width of the ribbon at each s is given by $|n_r - n_l|$. This parameterization will accommodate variable-width ribbons that need not be symmetric around the spine curve \mathcal{C} . If $\mathbf{r}(s, n)$ is a point in ∇ , then we will assume that there is a one-to-one mapping between this point and the parameter domain. Curves on ∇ corresponding to constant s , or constant n , are called *coordinate curves*; the coordinate curve corresponding to $n = 0$ is the spine of the ribbon. The spine is modelled as a simple curve \mathcal{C} and can be described in terms of the geometric entities introduced in Section 7.3.1. The camber vector lies in the plane normal to the spine's tangent vector \mathbf{t} and can therefore be described in terms of \mathbf{p} , \mathbf{b} , and a *twist angle* ν (around \mathbf{t}) as follows

$$\mathbf{n} = \mathbf{p} \cos \nu + \mathbf{b} \sin \nu. \quad (7.88)$$

The *twist rate* is ν' . A unit vector \mathbf{m} that is normal to the ribbon surface is defined to complete a right-handed axis system with \mathbf{t} and \mathbf{n} , whence $\mathbf{m} = \mathbf{t} \times \mathbf{n}$. See Figure 7.15 for an illustration of a ribbon and these quantities.

The Frenet–Serret formulae (7.84) can be used to describe the spine, but they do not have the flexibility to describe the ribbon itself. Developing again a kinematic interpretation of the problem, a moving triad $\mathbf{t} \mathbf{n} \mathbf{m}$, which we call the *ribbon trihedron*, is used to describe the evolution of the spine and the ribbon itself—note that the spine trihedron was previously defined using the moving triad $\mathbf{t} \mathbf{p} \mathbf{b}$. The ribbon trihedron is sometimes called the *Darboux frame* of ∇ on \mathcal{C} .

The angular rate of the reference frame fixed to the ribbon trihedron is given by the sum of the Darboux vector (7.85) and the twist rate ν'

$$\boldsymbol{\Omega}^{\mathcal{C}} = [\tau + \nu'] \mathbf{t} + \kappa \mathbf{b}. \quad (7.89)$$

The ribbon angular rate vector $\boldsymbol{\Omega}$ can be expressed in the ribbon trihedron through a coordinate transformation from the curve triad $\mathbf{t} \mathbf{p} \mathbf{b}$ to the ribbon triad $\mathbf{t} \mathbf{n} \mathbf{m}$ using $\mathcal{R}(\mathbf{e}_x, \nu)^T$ given by (2.157)

$$\boldsymbol{\Omega}^{\nabla} = \begin{bmatrix} 1 & 0 & 0 \\ 0 & \cos \nu & \sin \nu \\ 0 & -\sin \nu & \cos \nu \end{bmatrix} \begin{bmatrix} \tau + \nu' \\ 0 \\ \kappa \end{bmatrix} = \begin{bmatrix} \tau + \nu' \\ \kappa \sin \nu \\ \kappa \cos \nu \end{bmatrix}, \quad (7.90)$$

where $\boldsymbol{\Omega}^{\nabla}$ is expressed in the ribbon trihedron or Darboux frame. The angular rate vector $\boldsymbol{\Omega}^{\nabla}$ is thus a vector in \mathbb{R}^3 , which has a skew-symmetric matrix representation $S(\boldsymbol{\Omega}^{\nabla})$:

$$\boldsymbol{\Omega}^{\nabla} = \begin{bmatrix} \Omega_x \\ \Omega_y \\ \Omega_z \end{bmatrix}, \quad S(\boldsymbol{\Omega}^{\nabla}) = \begin{bmatrix} 0 & -\Omega_z & \Omega_y \\ \Omega_z & 0 & -\Omega_x \\ -\Omega_y & \Omega_x & 0 \end{bmatrix}, \quad (7.91)$$

where Ω_x , Ω_y , and Ω_z are known as the *relative torsion*, the *normal curvature*, and the *geodesic curvature*, respectively. The matrix $S(\boldsymbol{\Omega}^\nabla)$, also known as the *Cartan matrix* [260], is a generalization of the Frenet–Serret formulae to the case of ribbons and

$$\mathcal{R}' = \mathcal{R}S(\boldsymbol{\Omega}^\nabla). \quad (7.92)$$

As before, once the generalized curvature vector $\boldsymbol{\Omega}^\nabla$ and the widths n_r, n_l are given as a function of the curvilinear abscissa s , the ribbon can be computed by integration, given the initial conditions $\mathbf{x}(s_0)$ and $\mathcal{R}(s_0)$:

$$\begin{cases} \mathcal{R} = \int_{s_0}^s \mathcal{R}' ds, \\ \mathbf{r} = \int_{s_0}^s \mathbf{t} ds + n\mathbf{n}, \end{cases} \quad (7.93)$$

in which \mathcal{R}' is given by (7.92). The generalized Frenet–Serret equations are used as a differential-geometric description of ribbons in terms of their generalized curvature vector $\boldsymbol{\Omega}^\nabla$ and the width parameters.

7.3.3 Euler angles

The ribbon-based model of the road is given in (7.93), with the evolution of the ribbon trihedron as a function of arc length coming from integrating a 3×3 rotation matrix \mathcal{R} . As explained in Section 2.5, \mathcal{R} can be expressed using three rotations—the related angles are the Euler angles, which we herein define as θ , μ , and ϕ . As in most mechanics problems, the idea is to replace the 3×3 matrix \mathcal{R} in (7.92) with three scalar differential equations in the Euler angles.

The relationships between the θ , μ , and ϕ and κ , τ , and ν are obtained when noting that the ribbon angular rate given by Ω^C (7.89) or Ω^∇ (7.90) can also be expressed in terms of the Euler angles using (2.166) or (2.169) respectively, with $\mathcal{R} = \mathcal{R}(\theta, \mu, \phi)$. In the z - y - x (yaw, pitch, and roll) case,

$$\mathcal{R} = \mathcal{R}(e_z, \theta)\mathcal{R}(e_y, \mu)\mathcal{R}(e_x, \phi) = \begin{bmatrix} c_\theta c_\mu & c_\theta s_\mu s_\phi - s_\theta c_\phi & c_\theta s_\mu c_\phi + s_\theta s_\phi \\ s_\theta c_\mu & s_\theta s_\mu s_\phi + c_\theta c_\phi & s_\theta s_\mu c_\phi - c_\theta s_\phi \\ -s_\mu & c_\mu s_\phi & c_\mu c_\phi \end{bmatrix}, \quad (7.94)$$

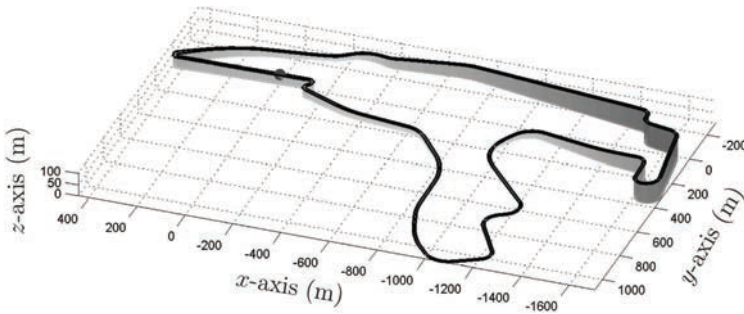


Figure 7.16: Ribbon-based model of the 7 km Circuit de Spa-Francorchamps: the start/finish line is marked with a black circle.

with $\mathcal{R}(e_i, \cdot)$ given by (2.156)–(2.158). The following relationships are obtained from $S(\Omega^\nabla) = \mathcal{R}^T \mathcal{R}'$:

$$\theta' = \kappa \frac{\cos(\nu - \phi)}{\cos \mu} \quad (7.95)$$

$$\mu' = \kappa \sin(\nu - \phi) \quad (7.96)$$

$$\phi' = \tau + \nu' + \kappa \tan \mu \cos(\nu - \phi). \quad (7.97)$$

Using (7.95)–(7.97), the kinematic parameterization of the ribbon (7.93) becomes

$$\begin{cases} \theta(s) &= \int_{s_0}^s \theta' ds, \\ \mu(s) &= \int_{s_0}^s \mu' ds, \\ \phi(s) &= \int_{s_0}^s \phi' ds, \\ \mathbf{r}(s, n) &= \int_{s_0}^s \mathbf{t} ds + n\mathbf{n}, \end{cases} \quad (7.98)$$

where \mathbf{t} and \mathbf{n} are the first and second columns, respectively, of the rotation matrix \mathcal{R} as given in (7.94).

The initial conditions $\theta(s_0)$, $\mu(s_0)$, and $\phi(s_0)$ are found by solving the inverse problem for a given $\nabla(s_0)$, for example, $\tan \theta = \mathcal{R}_{21}/\mathcal{R}_{11}$, $\tan \phi = \mathcal{R}_{32}/\mathcal{R}_{33}$, and $\sin \mu = -\mathcal{R}_{31}$, where \mathcal{R}_{ij} means row i and column j of \mathcal{R} .

Example 7.4 The differential geometric properties of the three-dimensional ribbon-based model for the Circuit de Spa-Francorchamps (Spa) is shown in Figure 7.16. The track features were estimated using measured GPS data for the road boundaries [256]. The model is then computed by solving an optimal control problem of the kind described in Section 8.6.7. Figure 7.17(a) shows the track's inclination angle (μ) and

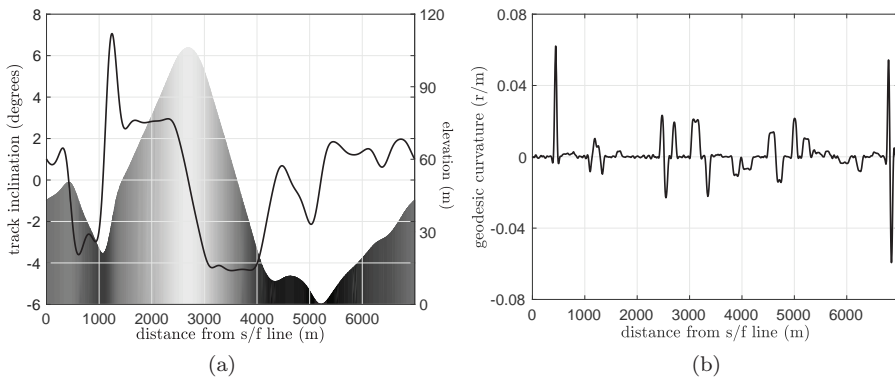


Figure 7.17: Track inclination and elevation (a) and geodesic curvature (b) of the Circuit de Spa-Francorchamps as functions of the distance from the start/finish line.

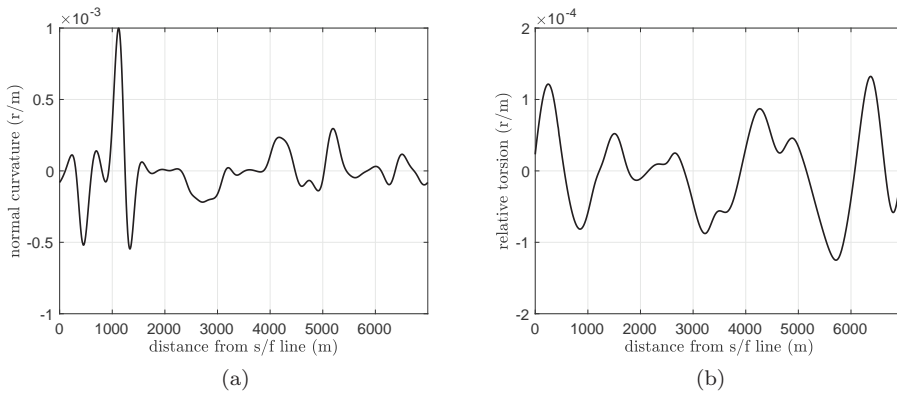


Figure 7.18: Normal curvature (a) and relative torsion (b) of the Circuit de Spa-Francorchamps as functions of the distance from the start/finish line.

spine elevation as a function of elapsed distance s . The start/finish line is approximately 43 m above the track's lowest point, with the full-track elevation change being approximately 106 m. Figure 7.17 (b) shows the track's geodesic curvature as a function of elapsed distance s . The first positive spike in the geodesic curvature Ω_z corresponds to the sharp right-hand hairpin (La source) following the start/finish line (the track is raced in a clockwise direction). Notable also is the positive-negative doublet in the geodesic curvature at approximately 6,825 m, which corresponds to the right-left chicane immediately before the start/finish line; the other track corners can be identified in much the same way. The normal curvature Ω_y describes the way in which the track elevation changes with elapsed distance, while the relative torsion Ω_x describes the way in which the track camber varies with elapsed distance. These curves are shown in Figure 7.18, with the track's camber (ϕ) shown in Figure 7.19.

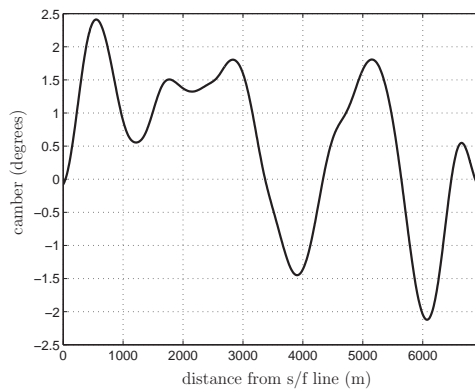


Figure 7.19: Camber angle of Circuit de Spa-Francorchamps as a function of the distance from the start/finish line.

7.4 Vehicle Positioning

The track and vehicle (bicycle, car, or motorcycle) kinematics can be modelled using the differential-geometric framework developed in Section 7.3. We assume that the road surface is a plane that is orthogonal to the road-surface-normal vector \mathbf{m} as defined in Section 7.3.2 and Figure 7.15. This ribbon-derived plane will move with the vehicle and generates a road surface that heaves, pitches, and rolls under the vehicle.

A track segment is illustrated in Figure 7.20 and shows an inertial axis system, a point s (the curvilinear abscissa) that travels with the car along the spine of the track, and a vector \mathbf{n} , which is perpendicular to the tangent vector \mathbf{t} and that points towards the projection on the ground plane of a fixed point G_p on the vehicle—this point could be the vehicle's mass centre, for example.

The road normal \mathbf{m} is perpendicular to \mathbf{t} and \mathbf{n} and defines the moving road tangent plane—the ribbon Darboux frame. The magnitude of \mathbf{n} is the perpendicular distance between the track's spine and the vehicle's fixed point G_p . The angle ξ is the yaw angle of the vehicle relative to the spine of the track \mathbf{t} . The track's spatial curvature vector or angular rate (in radians per metre) is given by (7.89) or (7.90). The track's angular velocity vector is given by $\boldsymbol{\omega} = \boldsymbol{\Omega} \frac{ds}{dt}$, where $\boldsymbol{\omega} = [\omega_x \ \omega_y \ \omega_z]^T$; in the unit-speed case $\boldsymbol{\omega} = \boldsymbol{\Omega}$, since $\frac{ds}{dt} = 1$.

The next kinematic relationships we will require relate to the way in which the vehicle progresses down the road. Suppose that the absolute velocity of the vehicle point G_p in its body-fixed coordinate system is $\mathbf{v} = [u \ v \ w]^T$ —these variables will derive from the integration of the equation of motion; see Section 4.2. The distance between the vehicle's fixed point G_p and the origin of the Darboux frame is $\mathbf{n} = [0 \ n \ 0]^T$ in Darboux coordinates assuming that G_p lies in the plane of the road.

We can now express the absolute velocity of G_p in the Darboux frame using (2.144)

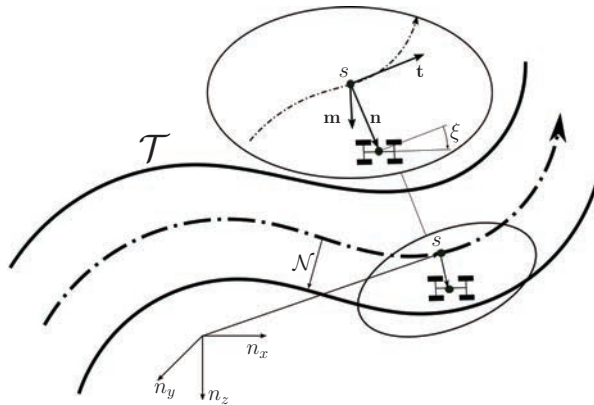


Figure 7.20: Differential-geometric description of a track segment \mathcal{T} . The track half-width is \mathcal{N} , with ξ the vehicle's yaw angle relative to the spine's tangent direction.

$$\begin{bmatrix} \dot{s} \\ 0 \\ 0 \end{bmatrix} + \boldsymbol{\omega} \times \mathbf{n} + \begin{bmatrix} 0 \\ \dot{n} \\ 0 \end{bmatrix} = \mathcal{R}(\mathbf{e}_z, \xi) \mathbf{v}, \quad (7.99)$$

where the first term on the left-hand side is the velocity of the Darboux frame origin, the second term is the transferred velocity and the third term is the relative velocity of G_p in the Darboux frame. The right-hand-side term is the absolute velocity of G_p , where $\mathcal{R}(\mathbf{e}_z, \xi)$ is given by (2.156) and represents the yawing of the vehicle relative to the spine of the track. Equation (7.99) can be rewritten as follows:

$$\begin{bmatrix} \dot{s} \\ \dot{n} \\ 0 \end{bmatrix} = \begin{bmatrix} n\omega_z + u \cos \xi - v \sin \xi \\ u \sin \xi + v \cos \xi \\ w - n\omega_x \end{bmatrix}. \quad (7.100)$$

The first row of (7.100) gives the speed of the origin of the Darboux frame in its tangent direction and can be written as

$$\dot{s} = \frac{u \cos \xi - v \sin \xi}{1 - n\Omega_z}, \quad (7.101)$$

since $\omega_z = \dot{s}\Omega_z$ in the variable-speed case. This equation is used to generate $S_f(s) = \frac{dt}{ds}$, which transforms ‘time’ as the independent variable into the ‘elapsed distance’ as the independent variable. In order to fulfil this function, $S_f(s)$ and its inverse must be non-zero everywhere on the spine curve. The second row of (7.100) describes the way in which the vehicle moves normal to the spine:

$$\dot{n} = u \sin \xi + v \cos \xi. \quad (7.102)$$

The third row of (7.100) describes the absolute vertical velocity of G_P as a result of the road camber changes, and follows from the fact that the vehicle cannot have a vertical velocity component in the \mathbf{m} direction. This gives

$$w = n\omega_x. \quad (7.103)$$

If the ‘distance travelled’ is selected as the independent variable, then a complete set of kinematics equations includes (7.101), which generates $S_f(s)$, (7.95)–(7.97), and

$$\frac{dn}{ds} = S_f(s) (u \sin \xi + v \cos \xi) \quad (7.104)$$

which comes from (7.102).

The angular velocity of the vehicle in its body-fixed frame $\bar{\boldsymbol{\omega}}$ is equal to the angular velocity of the road expressed in the vehicle-fixed frame, that is, $\mathcal{R}(\mathbf{e}_z, \xi)^T \boldsymbol{\omega}$, plus the angular velocity of the vehicle relative to the road, again expressed in the vehicle-fixed frame, that is, $[0, 0, \dot{\xi}]^T$ —the summation rule holds for angular velocities; Section 2.5. The following expression is thus obtained

$$\bar{\boldsymbol{\omega}} = \mathcal{R}(\mathbf{e}_z, \xi)^T \boldsymbol{\omega} + \begin{bmatrix} 0 \\ 0 \\ \dot{\xi} \end{bmatrix} \quad (7.105)$$

which gives

$$\begin{bmatrix} \bar{\omega}_x \\ \bar{\omega}_y \\ \bar{\omega}_z \end{bmatrix} = \begin{bmatrix} \omega_x \cos \xi + \omega_y \sin \xi \\ \omega_y \cos \xi - \omega_x \sin \xi \\ \omega_z + \dot{\xi} \end{bmatrix}. \quad (7.106)$$

We will use the vehicle dynamics equations to find $\bar{\omega}_z$, with the vehicle yaw angle ξ deduced from the third row of (7.106) by integrating

$$\frac{d\xi}{ds} = S_f(s)\bar{\omega}_z - \Omega_z. \quad (7.107)$$

Summarizing, the road is described in terms of the generalized curvature vector $\mathbf{\Omega}(s)$, that is, the curvature $\kappa(s)$, the torsion $\tau(s)$, and the twist $\nu(s)$. The position and orientation of the vehicle on the road are given in terms of $n(s)$ and $\xi(s)$ by integrating (7.104) and (7.107)— u , v , w , and $\bar{\omega}_z$ will come from the integration of the vehicle's equations of motion. Since the car has no suspension system, the vehicle's angular velocities $\bar{\omega}_x$ and $\bar{\omega}_y$ depend on the road angular velocities ω_x , ω_y , and ξ ; see (7.106). Examples of simulation of the combined road-vehicle model will be shown in Chapter 9 in the context of minimum time manoeuvring.

7.5 Car modelling

One of the early references relating to car dynamic models is [261]. An early model that predicts the steering response of a road car is developed in [262], where steering oscillations are also discussed. This paper shows a high level of agreement between steady-state measurements and theoretical calculations. An analysis of the influence of tyre characteristics on the behaviour of a car undergoing manoeuvres is given in [263]. Simulation results are used to assess the influence of variations in the lateral and longitudinal tyre stiffnesses, and the coefficient of friction at the tyre-road interface on the vehicle's steering and braking responses. Overviews of motor-vehicle dynamics modelling are available in [206, 264].

In this section we derive the equations of motion of a four-wheeled vehicle model that is suitable for optimal control calculations on a three-dimensional road of the type described in Section 7.3. The model includes slipping tyres and aerodynamic maps that depend on a quasi-static suspension model. The equations describing the dynamics of the car can be derived using either the Newton–Euler (Section 2.2.2) or the Lagrange equations (Section 2.2.8).

It follows from (2.144) and (7.103) that the absolute velocity of the car's mass centre (expressed on the vehicle's body-fixed coordinate system) is given by

$$\mathbf{v}_B = \mathbf{v} + \bar{\boldsymbol{\omega}} \times \mathbf{h} \quad (7.108)$$

$$= \begin{bmatrix} u \\ v \\ n\omega_x \end{bmatrix} + \begin{bmatrix} \bar{\omega}_x \\ \bar{\omega}_y \\ \bar{\omega}_z \end{bmatrix} \times \begin{bmatrix} 0 \\ 0 \\ -h \end{bmatrix} = \begin{bmatrix} u - h\bar{\omega}_y \\ v + h\bar{\omega}_x \\ n\omega_x \end{bmatrix}, \quad (7.109)$$

where \mathbf{v} is the velocity of the origin G_p of the vehicle-fixed frame of Section 7.4, $\bar{\boldsymbol{\omega}}$ the vehicle angular velocity, and h is the height of the vehicle mass centre above the

ground. The vertical velocity w of the vehicle-fixed frame has been written in terms of the road angular velocity component ω_x and the lateral position with respect to the centre line n .

Newton–Euler equations require the computation of the accelerations of the car. These are derived from the velocities \mathbf{v}_B and $\bar{\boldsymbol{\omega}}$, which are both defined in the body-fixed (non-inertial) frame. Application of (2.6) and (2.11) using (2.10) gives¹⁷

$$M(\dot{\mathbf{v}}_B + \bar{\boldsymbol{\omega}} \times \mathbf{v}_B) = F_B + Mg\mathcal{R}^T \mathbf{e}_z \quad (7.110)$$

$$I_B \dot{\bar{\boldsymbol{\omega}}} + \bar{\boldsymbol{\omega}} \times (I_B \bar{\boldsymbol{\omega}}) = M_B, \quad (7.111)$$

in which M is the car's mass and I_B its inertia with respect to the mass centre in the body-fixed coordinate system (assumed to be diagonal $I_B = \text{diag}(I_x \ I_y \ I_z)$), $F_B = [F_x \ F_y \ F_z]^T$ and $M_B = [M_x \ M_y \ M_z]^T$ are the external force and moment, and $\mathcal{R} = \mathcal{R}(\mathbf{e}_z, \theta)\mathcal{R}(\mathbf{e}_y, \mu)\mathcal{R}(\mathbf{e}_x, \phi)\mathcal{R}(\mathbf{e}_z, \xi)$ represents the orientation of the vehicle-fixed frame with respect to the ground, with θ, μ, ϕ the Euler angles related to the road Darboux frame (Section 7.3.3) and ξ the relative angle between the car and the road (Section 7.4). The gravitational acceleration acting on the car's mass centre is

$$g\mathcal{R}^T \mathbf{e}_z = g \begin{bmatrix} \sin \xi \sin \phi \cos \mu - \cos \xi \sin \mu \\ \sin \xi \sin \mu + \cos \xi \sin \phi \cos \mu \\ \cos \phi \cos \mu \end{bmatrix}. \quad (7.112)$$

The car's equations of motion can now be assembled from (7.110), (7.111), and (7.112) as follows:

$$\begin{aligned} \dot{u} &= (v + h\bar{\omega}_x)\bar{\omega}_z - n\omega_x\bar{\omega}_y + h\dot{\bar{\omega}}_y \\ &\quad + g(\sin \xi \sin \phi \cos \mu - \cos \xi \sin \mu) + F_x/M \end{aligned} \quad (7.113)$$

$$\begin{aligned} \dot{v} &= n\omega_x\bar{\omega}_x - (u - h\bar{\omega}_y)\bar{\omega}_z - h\dot{\bar{\omega}}_x \\ &\quad + g(\sin \xi \sin \mu + \cos \xi \sin \phi \cos \mu) + F_y/M \end{aligned} \quad (7.114)$$

$$\dot{\bar{\omega}}_z = ((I_x - I_y)\bar{\omega}_x\bar{\omega}_y + M_z)/I_z, \quad (7.115)$$

in which F_x , F_y , and M_z are, respectively, the longitudinal and lateral tyre and aerodynamic forces, and the z -axis tyre moment acting on the car. These quantities are illustrated in Figure 7.21 and are given by

$$F_x = \cos \delta(F_{f_{rx}} + F_{f_{lx}}) - \sin \delta(F_{f_{ry}} + F_{f_{ly}}) + F_{rrx} + F_{rlx} + F_{ax} \quad (7.116)$$

$$F_y = \cos \delta(F_{f_{ry}} + F_{f_{ly}}) + \sin \delta(F_{f_{rx}} + F_{f_{lx}}) + F_{rry} + F_{rly} \quad (7.117)$$

$$\begin{aligned} M_z &= a(\cos \delta(F_{f_{ry}} + F_{f_{ly}}) + \sin \delta(F_{f_{rx}} + F_{f_{lx}})) - b(F_{rry} + F_{rly}) \\ &\quad + w_f(\sin \delta(F_{f_{ry}} - F_{f_{ly}}) + \cos \delta(F_{f_{lx}} - F_{f_{rx}})) \\ &\quad + w_r(F_{rlx} - F_{rrx}), \end{aligned} \quad (7.118)$$

where F_{ax} is the aerodynamic drag force (more detail will be given in Section 7.5.6).

¹⁷ The transformation of the time derivative between inertial and body-fixed reference frames is (chapter IV in [42])

$$\left. \frac{d \cdot}{dt} \right|_I = \left. \frac{d \cdot}{dt} \right|_B + \bar{\boldsymbol{\omega}} \times \cdot$$

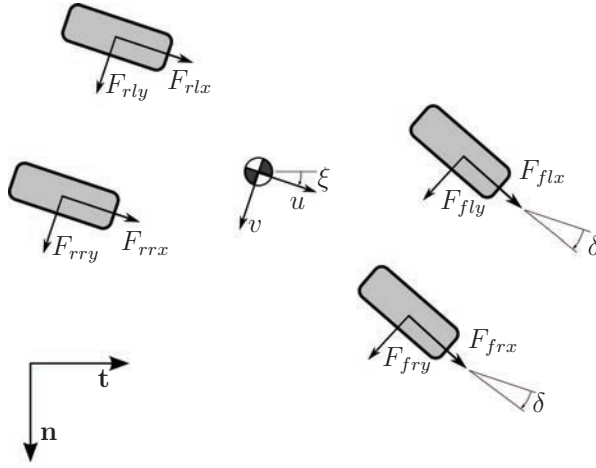


Figure 7.21: Tyre force system. The car's yaw angle is ξ with respect to the Darboux frame, which is defined in terms of the vectors \mathbf{t} and \mathbf{n} .

If spinning road wheels are included in the model, they can be described by equations of the form

$$I_{wij}\dot{\omega}_{ij} = T_{ij} - R_i F_{ijx} \quad i = f, r \quad j = l, r. \quad (7.119)$$

The moment of inertia of each wheel about its axis of rotation is I_{wij} , the radius of each wheel is R_i ; the wheel torque is T_{ij} (positive when propulsive and negative when braking) and the wheel angular velocities are given by ω_{ij} ($i = f, r$ $j = l, r$).

The time domain equations of motion (7.113), (7.114), and (7.115), can be expressed in terms of the elapsed distance as follows:

$$\frac{du}{ds} = S_f \dot{u} \quad (7.120)$$

$$\frac{dv}{ds} = S_f \dot{v} \quad (7.121)$$

$$\frac{d\bar{\omega}_z}{ds} = S_f \dot{\omega}_z. \quad (7.122)$$

The angular accelerations $\dot{\omega}_y$ in (7.113) and $\dot{\omega}_x$ in (7.114) can be derived from (7.106). In many cases the Darboux frame $\dot{\omega}_x$ and $\dot{\omega}_y$ can be neglected, and so

$$\dot{\omega}_x \approx \dot{\xi}(\omega_y \cos \xi - \omega_x \sin \xi) \quad (7.123)$$

$$\dot{\omega}_y \approx -\dot{\xi}(\omega_y \sin \xi + \omega_x \cos \xi). \quad (7.124)$$

7.5.1 Tyre friction

The tyre frictional forces can be modelled using empirical formulae of the type described in Chapter 3. The tyre's longitudinal slip is described by a longitudinal slip coefficient κ , while the lateral slip is described by a slip angle α , where

$$\kappa = - \left(1 - \frac{R_i \omega_{ij}}{u_w} \right), \quad (7.125)$$

$$\tan \alpha = - \frac{v_w}{u_w}, \quad (7.126)$$

where R_i is the wheels' radius and ω_{ij} the wheels' spin angular velocity (non-negative in normal running conditions). The terms u_w and v_w are the absolute speed components of the wheel centre in a wheel-fixed coordinate system. The four wheel slip angles are given by

$$\begin{aligned} \alpha_{rr} &= -\arctan \left(\frac{v - \bar{\omega}_z b}{u - \bar{\omega}_z w_r} \right), \\ \alpha_{rl} &= -\arctan \left(\frac{v - \bar{\omega}_z b}{u + \bar{\omega}_z w_r} \right), \\ \alpha_{fr} &= -\arctan \left(\frac{v + \bar{\omega}_z a}{u - \bar{\omega}_z w_f} \right) + \delta, \\ \alpha_{fl} &= -\arctan \left(\frac{v + \bar{\omega}_z a}{u + \bar{\omega}_z w_f} \right) + \delta, \end{aligned} \quad (7.127)$$

with the longitudinal slip ratios given by

$$\begin{aligned} \kappa_{rr} &= - \left(1 - \frac{R \omega_{rr}}{u - \bar{\omega}_z w_r} \right), \\ \kappa_{rl} &= - \left(1 - \frac{R \omega_{rl}}{u + \bar{\omega}_z w_r} \right), \\ \kappa_{fr} &= - \left(1 - \frac{R \omega_{fr}}{\cos \delta (u - \bar{\omega}_z w_f) + \sin \delta (v + \bar{\omega}_z a)} \right), \\ \kappa_{fl} &= - \left(1 - \frac{R \omega_{fl}}{\cos \delta (u + \bar{\omega}_z w_f) + \sin \delta (v + \bar{\omega}_z a)} \right). \end{aligned} \quad (7.128)$$

Equations (7.127) should be compared with (4.5)–(4.6) corresponding to the single-track car model. Sometimes alternative expressions for the front slips are reported,¹⁸ which are derived using the trigonometric identity $\arctan A + \arctan B = \arctan \frac{A+B}{1-AB}$.

7.5.2 Load transfer

The ability of the tyres to generate side forces is influenced by the normal loads acting on them. In order to compute the tyre loads as the car moves down the road, we balance the forces acting on the car normal to the road, and then balance moments around the body-fixed roll and pitch axes, x_b and y_b , respectively; see Figure 7.22. These calculations must recognize the gravitational, inertial, centripetal, and aerodynamic forces acting on the car, as well as the gyroscopic moments.

The vertical force balance on the car comes from the z -axis component of (7.110)

$$\begin{aligned} n\dot{\omega}_x &= (F_{rrz} + F_{rlz} + F_{frz} + F_{flz} + F_{az}^f + F_{az}^r) / M \\ &\quad + g \cos \phi \cos \mu + u\bar{\omega}_y - v\bar{\omega}_x - h (\bar{\omega}_x^2 + \bar{\omega}_y^2) - \omega_x \dot{n}, \end{aligned} \quad (7.129)$$

in which the $F_{\cdot z}$ s are the vertical tyre forces acting on each of the four wheels (all the $F_{\cdot z}$ s are negative under parked equilibrium conditions), F_{az}^f and F_{az}^r are the

¹⁸ $\alpha_{fr} = \arctan \left(\frac{\sin \delta (\bar{\omega}_z w_f - u) + \cos \delta (\bar{\omega}_z a + v)}{\cos \delta (u - \bar{\omega}_z w_f) + \sin \delta (\bar{\omega}_z a + v)} \right)$ and $\alpha_{fl} = \arctan \left(\frac{\cos \delta (\bar{\omega}_z a + v) - \sin \delta (\bar{\omega}_z w_f + u)}{\cos \delta (\bar{\omega}_z w_f + u) + \sin \delta (\bar{\omega}_z a + v)} \right)$.

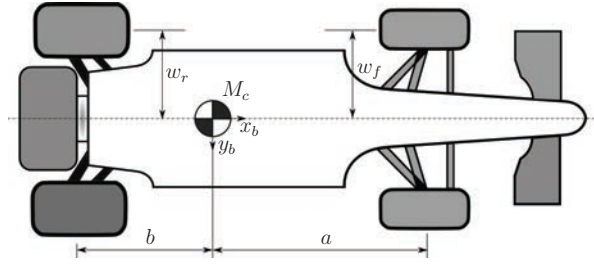


Figure 7.22: Plan view showing some of the vehicle's basic geometric parameters.

aerodynamic downforces at the front and rear axles, the seventh term is the force due to gravity, and the eighth and ninth terms are centripetal forces. In many cases the $\dot{\omega}_x$ term in (7.129) can be neglected.

Balancing moments (7.111) around the car's mass centre in the x_b direction gives

$$I_x \dot{\omega}_x = w_r(F_{rrz} - F_{rlz}) + w_f(F_{frz} - F_{flz}) - hF_y + (I_y - I_z)\bar{\omega}_z\bar{\omega}_y. \quad (7.130)$$

The first two terms are the roll moments produced by the vertical tyre forces, the third term is the roll moment produced by the lateral tyre forces F_y in (7.117), and the fourth term is a gyroscopic moment acting in the x_b direction; see Figure 7.22. In many cases the $\dot{\omega}_x$ term in (7.130) can be approximated by (7.123).

Balancing moments (7.111) around the car's mass centre in the y_b direction gives

$$I_y \dot{\omega}_y = b(F_{rrz} + F_{rlz} + F_{az}^r) - a(F_{frz} + F_{flz} + F_{az}^f) + hF_x + (I_z - I_x)\bar{\omega}_z\bar{\omega}_x. \quad (7.131)$$

The first two terms represent the pitching moments produced by the vertical tyre forces and downforces, the third term is the pitching moment produced by the longitudinal force F_x in (7.116), and the fourth term is a gyroscopic moment acting in the y_b direction. In many cases the $\dot{\omega}_y$ term in (7.131) can be approximated by (7.124).

Equations (7.129), (7.130), and (7.131) constitute a set of three linear equations in four unknowns. This structure is statically indeterminate (or hyperstatic) and so a fourth equation is required in order to make a unique solution possible. A unique solution for the tyre loads can be obtained by adding a suspension-related roll balance relationship, in which the lateral load difference across the front axle is some fraction of the whole

$$F_{frz} - F_{flz} = D(F_{frz} + F_{rrz} - F_{flz} - F_{rlz}), \quad (7.132)$$

where $D \in [0, 1]$. If this fourth equation is recognized, and equations (7.129), (7.130), (7.131), and (7.132) are linearly independent, a unique solution results. A comparison between (7.132), and (7.62) and (7.65), with $c_F = c_R = c$, gives

$$D = \frac{K_F}{K} \frac{h-d}{h} + \frac{d_F}{w} \frac{b}{h}. \quad (7.133)$$

7.5.3 Non-negative tyre loads

The forces satisfying equations (7.129), (7.130), (7.131), and (7.132) are potentially both positive and negative. Negative forces are indicative of vertical reaction forces, while positive forces are fictitious ‘forces of attraction’. Since the model being considered here has no pitch, roll, or heave freedoms, none of the wheels is free to leave the road, while simultaneously keeping faith with (7.129) to (7.132); an approximation is thus required.

To cater for the possible ‘positive force’ (‘light wheel’) situation within an optimal control environment we introduce the tyre normal load vector $\bar{\mathbf{F}}_{\mathbf{z}} = [\bar{F}_{flz}, \bar{F}_{frz}, \bar{F}_{rlz}, \bar{F}_{rrz}]^T$, which may contain positive components. These are set to zero by defining $\mathbf{F}_{\mathbf{z}} = \min(\bar{\mathbf{F}}_{\mathbf{z}}, \mathbf{0})$, where the minimum function $\min(\cdot, \cdot)$ is interpreted element-wise. It is clear that $\bar{\mathbf{F}}_{\mathbf{z}}$ and $\mathbf{F}_{\mathbf{z}}$ will be equal unless at least one entry of $\bar{\mathbf{F}}_{\mathbf{z}}$ is positive (i.e. non-physical). Since the model must respect the laws of mechanics, equations (7.129), (7.130), and (7.131) must be enforced unconditionally. In contrast, we assume that the solution to (7.132), which is only an approximate representation of the suspension system, can be ‘relaxed’ in the event of a tyre normal load sign reversal.

Equations (7.129), (7.130), and (7.131) are arranged in matrix form as

$$A_1 \mathbf{F}_{\mathbf{z}} = \mathbf{c}, \quad (7.134)$$

while (7.132) can be written as

$$A_2 \mathbf{F}_{\mathbf{z}} = \mathbf{0}. \quad (7.135)$$

The entries in the matrices A_1 and A_2 and the vector \mathbf{c} can be assembled from (7.129), (7.130), (7.131), and (7.132). In order to deal with the ‘light wheel’ situation, we combine (7.134) and (7.135) as

$$\begin{bmatrix} A_1 & 0 \\ 0 & A_2 \end{bmatrix} \begin{bmatrix} \mathbf{F}_{\mathbf{z}} \\ \bar{\mathbf{F}}_{\mathbf{z}} \end{bmatrix} = \begin{bmatrix} \mathbf{c} \\ \mathbf{0} \end{bmatrix} \quad (7.136)$$

in which $\mathbf{F}_{\mathbf{z}}$ in (7.135) has been replaced by $\bar{\mathbf{F}}_{\mathbf{z}}$. If there is a ‘light wheel’, the mechanics equations (7.129), (7.130), and (7.131) will be satisfied by the non-positive forces $\mathbf{F}_{\mathbf{z}}$, while the roll balance equation (7.132) is satisfied by the now fictitious forces $\bar{\mathbf{F}}_{\mathbf{z}}$ that contain a ‘force of attraction’. It is clear that the tyre normal loads have to satisfy (7.136), which will be treated as constraints within an optimal control environment. The ‘light wheel’ modelling is covered in more detail in [255].

7.5.4 Wheel torque distribution

In order to optimize the vehicle’s performance, one needs to control the torques applied to the individual road wheels. In some applications, including Formula One racing, the braking system is designed so that equal pressure is applied to the brake callipers of each axle, with the braking pressures between the front and rear axles satisfying a pre-specified design ratio (7.9). The drive torques applied to the driven wheels are controlled by a differential mechanism.

Brakes. We equate equal brake calliper pressures with equal braking torques when neither wheel on a particular axle is locked. If one wheel is locked, the braking torque applied to the locked wheel may be lower than that applied to the rolling wheel. In the case of the front wheels, assuming negligible spin inertia, this constraint might be modelled as

$$0 = \max(\omega_{fr}, 0) \max(\omega_{fl}, 0) (F_{frx} - F_{flx}), \quad (7.137)$$

in which ω_{fr} and ω_{fl} are the angular velocities of the front right and front left wheel, respectively. If either road wheel ‘locks up’, the corresponding angular velocity will be non-positive and the braking torque constraint (7.137) becomes inactive. The rear wheels are treated similarly, with $(\cdot)_{rr,rl}$ replacing $(\cdot)_{fr,fl}$ in (7.137).

Differential. One might want to assume that the drive torque is delivered to the driven heels through a limited-slip differential. In the case of a RWD vehicle one may wish to stipulate

$$R_r(F_{lrx} - F_{rrx}) = -k_d(\omega_{lr} - \omega_{rr}), \quad (7.138)$$

in which ω_{lr} and ω_{rr} are the rear-wheel angular velocities, R_r is the rear-wheels’ radius, and k_d is a torsional damping coefficient. The special cases of an open and a locked differential correspond to $k_d = 0$ and k_d arbitrarily large respectively. The speed-sensing differential in (7.138), where the torque bias on the driven axle is related to wheels’ speed difference, could be replaced by a torque-sensing differential, in which the torque bias is related to the torque input, with possibly different behaviours in driving and coasting conditions [166, 265].

7.5.5 Suspensions

A variety of different car suspensions have been devised. An introductory discussion of vehicular suspension systems can be found in [266]. A number of independent suspensions are surveyed in [267], where the synthesis of suspension linkages is studied, including their kinematic structure, their dimensions, and their compliance properties. The well-known MacPherson strut suspension is modelled in [268] as a three-dimensional kinematic mechanism; both linear and nonlinear analyses are provided. A MacPherson suspension mechanism model is also developed in [269].

In Section 7.2.3 we presented a simple graphical method for computing the roll centre of MacPherson and double-wishbone suspensions. In this section we focus on the analytic modelling of a typical Formula One suspension. Among the objectives of the analysis are the determination of the position and orientation of the wheel as the suspension compresses/extends, and the computation of the vertical force F_z on a wheel generated by the spring-damper force F in the suspension strut. The relationship between F_z and F can be obtained using the virtual power principle. This gives

$$F_z \dot{z} = F \dot{l}, \quad (7.139)$$

where z is the wheel vertical travel and l is the suspension strut travel. Thus

$$F_z = F \left(\frac{\dot{l}}{\dot{z}} \right) = F \tau, \quad (7.140)$$

where τ is the velocity ratio. The suspension is called *progressive* when τ increases as the suspension compresses.

Formula One suspension. Figure 7.23 shows the twenty-four elements of a Formula One car suspension. The wishbones are shown solid, the pushrods are shown dashed, and the trackrods are shown dotted. The ends of the wishbones, pushrods and trackrods are all marked with hexagrams. A detailed kinematic and quasi-static analysis of a typical multi-link suspension will now be given.

The kinematics of a suspension system are determined by its motion constraints. We will now focus on Figure 7.24(a), which shows the suspension of the front-left wheel. Rods one to four make up the double-wishbone suspension elements. Rod five is the steering trackrod, which connects the wheel carrier to the steering rack. Rod six is the suspension push bar, which connects the wheel carrier to a suspension strut rocker mechanism mounted within the car's body; see Figure 7.25. In the following analysis all the joints in Figure 7.24 are treated as spherical.

In order to describe the suspension motion constraints in detail, we introduce car-fixed and wheel-carrier-fixed reference frames with origins O_C and O_W respectively. As shown in Figure 7.24(a), points P_1 to P_4 are fixed in the car chassis and are connected to Q_1 to Q_4 that are fixed in the wheel carrier using fixed-length wishbones of length l_i $i = 1, \dots, 4$. Points P_5 and Q_5 are at opposite ends of the steering trackrod with Q_5 fixed in the wheel carrier. Point P_5 is connected to the steering rack and moves in the car body (y -direction) as the steering-wheel position is varied. Points P_6 and Q_6 are at opposite ends of the suspension pushrod with Q_6 fixed in the wheel carrier. Point P_6 is connected to a rocker mechanism and moves in the car body in sympathy with movements of the pushrod; see Figure 7.25. The steering trackrod and suspension pushrod have lengths l_5 and l_6 respectively. This system has two degrees of freedom corresponding to changes in the steering angle and to changes in the angular position of the suspension rocker mechanism. The suspension rockers are also connected to a

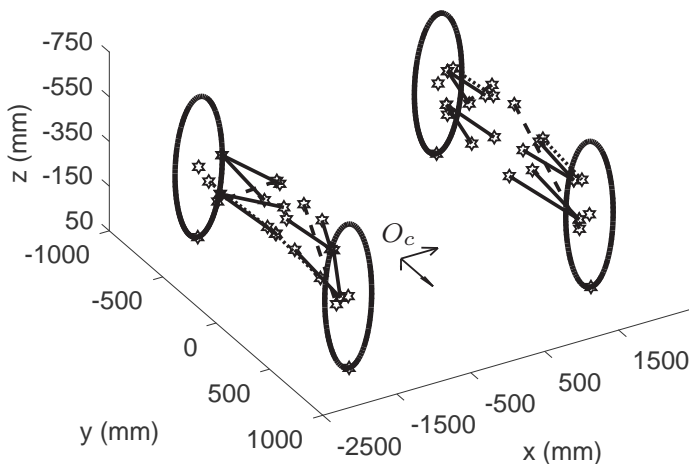


Figure 7.23: The suspension system of a typical Formula One car.

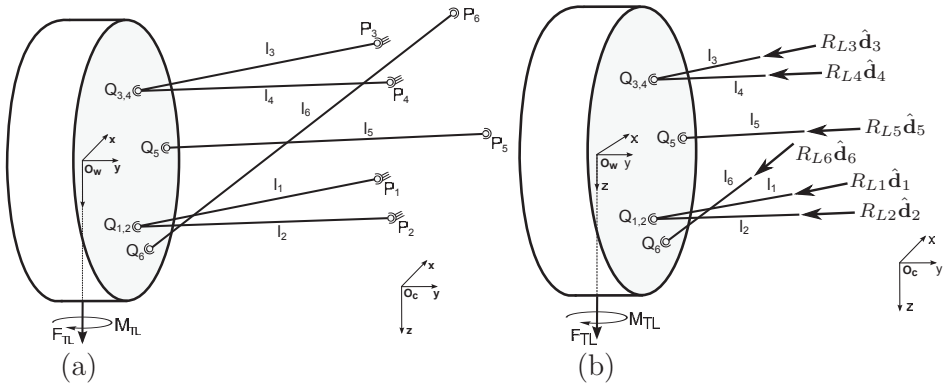


Figure 7.24: Front-left suspension configuration of a typical Formula One car with a pushrod suspension system (a) and free body diagram of the front-left wheel carrier (b).

parallel heave spring and damper combination, a torsion bar, and an anti-roll bar; the damper is not considered in the quasi-static analysis presented here. A tyre moment M_{TL} is applied to the wheel carrier body, with a tyre force F_{TL} applied at the wheel's ground-contact point.

In the following analysis all vectors will be expressed in the car reference frame. In the case a vector is resolved in the wheel carrier frame the following notation will be used $(\cdot)^W$. Six motion constraints derive from the fixed lengths of the six suspension elements. If we suppose that P_i and Q_i are vector representations of the corresponding points in Figure 7.24 (a), then the magnitudes of each of the six differences $P_i - Q_i$ (lengths) must be fixed too. That is,

$$\|P_i - Q_i\|^2 = l_i^2 \quad i = 1, \dots, 6, \quad (7.141)$$

in which the lengths l_i are constant. A steering angle δ results in a displacement of the steering rod mount point P_5 in the y -axis direction, which is proportional to the radius r of the steering pinion

$$P_5 = [0 \ -r\delta \ 0]^T + P_5^0; \quad (7.142)$$

P_5^0 is the straight-running position of P_5 . These equations determine a hypersurface over which the twelve points in Figure 7.24 (a) must move.

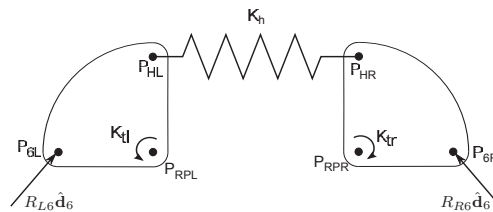


Figure 7.25: Pushrod and rocker setup; the heave spring has stiffness K_h .

There are six degrees of relative motion movement that are constrained by (7.141). The translational freedoms (relative to the car) of the wheel carrier reference frame origin \mathbf{O}_W are

$$\mathbf{D} = [\Delta x \ \Delta y \ \Delta z]^T. \quad (7.143)$$

The rotational freedoms of the wheel carrier relative to the vehicle's chassis are described in terms of the elementary rotations $\mathcal{R}(\mathbf{e}_x, \phi)$, $\mathcal{R}(\mathbf{e}_y, \theta)$, and $\mathcal{R}(\mathbf{e}_z, \psi)$, which are described by (2.156)–(2.157). When employing the yaw–roll–pitch (ψ – ϕ – θ) convention

$$\mathbf{X} = \mathcal{R}(\mathbf{e}_z, \psi) \mathcal{R}(\mathbf{e}_x, \phi) \mathcal{R}(\mathbf{e}_y, \theta) \mathbf{X}^W + \mathbf{D} \quad (7.144)$$

describes a point \mathbf{X}^W , which is fixed in the wheel carrier, in the chassis frame. Equations (7.141) and (7.144) provide six motion constraints that determine the kinematic behaviour of the suspension system.

As shown in Figure 7.25, the left- and right-hand sides of the suspension system are coupled through a heave spring (and a parallel damper which is not shown) and a rocker assembly. The right- and left-hand rockers are mounted on torsion bars with stiffnesses K_{tr} and K_{tl} respectively. The two rockers are also coupled by an anti-roll bar that resists chassis roll. This is represented by a moment $(\alpha_R + \alpha_L)K_{arb}$ applied to each rocker, in which α_R and α_L are the right- and left-hand rocker angles. The anti-roll bar stiffness is denoted by K_{arb} . In Figure 7.25 R_{L6} and R_{R6} are the magnitudes of the right- and left-hand pushrod forces, \mathbf{P}_{6L} and \mathbf{P}_{6R} are the pushrod attachment points, \mathbf{P}_{HL} and \mathbf{P}_{HR} are the end points of the heave spring, \mathbf{R}_{RPL} and \mathbf{R}_{RPR} are the rocker pivot points, and K_h is the heave spring stiffness.

A moment balance around the pin joint \mathbf{P}_{RPL} gives

$$0 = ((\mathbf{P}_{6L} - \mathbf{P}_{RPL}) \times F_{L6} \hat{\mathbf{d}}_6 + (\mathbf{P}_{HL} - \mathbf{P}_{RPL}) \times F_{heave} \hat{\mathbf{d}}_{hs}) \cdot \mathbf{n}_{RL} - K_{tl} \alpha_L - K_{arb}(\alpha_L + \alpha_R) \quad (7.145)$$

in which \mathbf{n}_{RL} is the left rocker pivot rotation axis, $\hat{\mathbf{d}}_6$ is a unit vector in the direction of l_6 , $\hat{\mathbf{d}}_{hs}$ is a unit vector in the heave spring direction pointing from \mathbf{P}_{HL} to \mathbf{P}_{HR} and F_{heave} is the heave spring force magnitude.

In the same way, one can take moments around \mathbf{P}_{RPR} to obtain

$$0 = ((\mathbf{P}_{6R} - \mathbf{P}_{RPR}) \times F_{R6} \hat{\mathbf{d}}_6 - (\mathbf{P}_{HR} - \mathbf{P}_{RPR}) \times F_{heave} \hat{\mathbf{d}}_{hs}) \cdot \mathbf{n}_{RR} - K_{tr} \alpha_R - K_{arb}(\alpha_L + \alpha_R) \quad (7.146)$$

in which $\hat{\mathbf{d}}_6$ in (7.146) must be interpreted in the context of the right-hand suspension assembly. The heave spring force F_{heave} is a function of the change in its length, and is given by

$$F_{heave} = k_h \Delta L \quad (7.147)$$

in which $\Delta L = \|\mathbf{P}_{HR} - \mathbf{P}_{HL}\| - L_0$, with L_0 the unloaded length. In general, the heave spring stiffness tends to ‘harden’ as it is compressed, thus giving a nonlinear relationship between the spring force and spring travel.

The quasi-static equations of motion describing the suspension system are determined using force and moment balances with the aid of the free body diagram shown

in Figure 7.24 (b). We will suppose that the reaction force acting at point Q_i has magnitude R_{Li} and acts in direction $\hat{\mathbf{d}}_i$. It should be noted that although the reaction forces are vector-valued quantities, it is only the magnitudes of these vectors that are unknown, since their directions are determined by the kinematic constraints. The external forces acting on the wheel carrier are the tyre force \mathbf{F}_{TL} , and the gravitational force due to the wheel carrier's mass m_L , which is given by

$$\mathbf{F}_{Lg} = [0 \ 0 \ m_L g]^T. \quad (7.148)$$

Summing forces on the left-hand wheel carrier gives

$$0 = \mathbf{F}_{TL} + \mathbf{F}_{Lg} + R_{L1}\hat{\mathbf{d}}_1 + R_{L2}\hat{\mathbf{d}}_2 + R_{L3}\hat{\mathbf{d}}_3 + R_{L4}\hat{\mathbf{d}}_4 + R_{L5}\hat{\mathbf{d}}_5 + R_{L6}\hat{\mathbf{d}}_6, \quad (7.149)$$

in which R_{L6} is the force acting on the left-hand rocker. This equation provides three scalar equations in the six left-hand unknown reaction force magnitudes. A similar force balance on the right-hand front wheel carrier gives

$$0 = \mathbf{F}_{TR} + \mathbf{F}_{Rg} + R_{R1}\hat{\mathbf{d}}_1 + R_{R2}\hat{\mathbf{d}}_2 + R_{R3}\hat{\mathbf{d}}_3 + R_{R4}\hat{\mathbf{d}}_4 + R_{R5}\hat{\mathbf{d}}_5 + R_{R6}\hat{\mathbf{d}}_6, \quad (7.150)$$

where R_{R6} is the force acting on the right-hand suspension rocker. In this case

$$\mathbf{F}_{Rg} = [0 \ 0 \ m_R g]^T \quad (7.151)$$

with the $\hat{\mathbf{d}}_i$ s interpreted in a like manner in the context of the right-hand front wheel. This equation provides another three equations in the six right-hand reaction force magnitudes.

As we will now show the remaining equations come from moment balance calculations. To begin, we define a set of vectors that point from point Q_1 , which is fixed in the wheel carrier, to points Q_i $i = 2, \dots, 6$, O_W and the tyre ground-contact point Q_{GC} . These vectors are given by \mathbf{d}_{12} , \mathbf{d}_{13} , \mathbf{d}_{14} , \mathbf{d}_{15} , \mathbf{d}_{16} , \mathbf{d}_{1W} , and \mathbf{d}_{1GC} respectively. With the exception of \mathbf{d}_{1GC} , these vectors are known and fixed in the wheel carrier. In order to find the vector \mathbf{d}_{1GC} , which represents a moving point in the wheel frame, we need to study the geometry of the ground-contact point. To that end we introduce the vector $\hat{\mathbf{e}}_w^W = [0 \ 1 \ 0]^T$, which is fixed in the wheel carrier, and points in the direction of the wheel spindle. The wheel spindle unit vector, expressed in the car frame, is thus given by

$$\hat{\mathbf{e}}_w = \mathcal{R}(\mathbf{e}_z, \psi) \mathcal{R}(\mathbf{e}_x, \phi) \mathcal{R}(\mathbf{e}_y, \theta) \hat{\mathbf{e}}_w^W. \quad (7.152)$$

If the pitch and roll of the car relative to the road are 'small', the unit road-normal expressed in the chassis frame can be approximated by $\hat{\mathbf{e}}_{rn} = [0 \ 0 \ 1]^T$. This means that the vector pointing from the wheel centre to the ground-contact point is given by

$$\mathbf{r}_w = \frac{(\hat{\mathbf{e}}_{cw} \times \hat{\mathbf{e}}_{rn}) \times \hat{\mathbf{e}}_{cw}}{\|(\hat{\mathbf{e}}_{cw} \times \hat{\mathbf{e}}_{rn}) \times \hat{\mathbf{e}}_{cw}\|} R_{fw} \quad (7.153)$$

and so $\mathbf{d}_{1GC} = \mathbf{r}_w + \mathbf{d}_{1W}$; R_{fw} is the loaded tyre radius, which depends on the tyre force \mathbf{F}_{TL} and is usually determined by measurement.

Taking moments around \mathbf{Q}_1 in Figure 7.24 (B) gives

$$\begin{aligned} 0 = & \mathbf{M}_{TL} + \mathbf{d}_{1GC} \times \mathbf{F}_{TL} + \mathbf{d}_{1W} \times \mathbf{F}_{Lg} + R_{L2}(\hat{\mathbf{d}}_2 \times \mathbf{d}_{12}) \\ & + R_{L3}(\hat{\mathbf{d}}_3 \times \mathbf{d}_{13}) + R_{L4}(\hat{\mathbf{d}}_4 \times \mathbf{d}_{14}) + R_{L5}(\hat{\mathbf{d}}_5 \times \mathbf{d}_{15}) \\ & + R_{L6}(\hat{\mathbf{d}}_6 \times \mathbf{d}_{16}). \end{aligned} \quad (7.154)$$

A similar calculation for the front-right wheel gives

$$\begin{aligned} 0 = & \mathbf{M}_{TR} + \mathbf{d}_{1GC} \times \mathbf{F}_{TR} + \mathbf{d}_{1W} \times \mathbf{F}_{Rg} + R_{R2}(\hat{\mathbf{d}}_2 \times \mathbf{d}_{12}) \\ & + R_{R3}(\hat{\mathbf{d}}_3 \times \mathbf{d}_{13}) + R_{R4}(\hat{\mathbf{d}}_4 \times \mathbf{d}_{14}) + R_{R5}(\hat{\mathbf{d}}_5 \times \mathbf{d}_{15}) \\ & + R_{R6}(\hat{\mathbf{d}}_6 \times \mathbf{d}_{16}) \end{aligned} \quad (7.155)$$

in which the vectors $\hat{\mathbf{d}}_2, \dots, \hat{\mathbf{d}}_6$, \mathbf{d}_{1GC} , and $\mathbf{d}_{12}, \dots, \mathbf{d}_{16}$ must be interpreted in an analogous manner in the context of the right-hand suspension.

In sum, equations (7.141) are used to determine the right- and left-hand Euler angles and the right- and left-hand wheel carrier displacements in (7.143); twelve variables in total. Equations (7.145) and (7.146) determine the two rocker angles. Equations (7.149), (7.150), (7.154), and (7.155) determine the twelve right- and left-hand pushrod force magnitudes. Equations (7.141), (7.145), (7.146), (7.149), (7.150), (7.154), and (7.155) can be solved for the twenty-six unknowns associated with each axle as a function of the tyre force \mathbf{F}_T and tyre moment \mathbf{M}_T using a nonlinear algebraic equation solver.

Figure 7.26 illustrates the typical force-displacement behaviour of the front-left suspension system as a function of the normal tyre load; the front-right tyre is assumed unloaded [270], that is, the inputs are $\mathbf{F}_{TL} = [0, 0, F_{flz}]^T$, $\mathbf{M}_{TL} = \mathbf{M}_{TR} = \mathbf{F}_{TR} = [0, 0, 0]^T$, and $\delta = 0$. It is evident from Figure 7.26 that the wheel's camber and toe angles vary very little as a result of normal load variations. This figure also shows that the suspension movement resulting from normal load variations is almost entirely in the vertical direction.

7.5.6 Aerodynamic maps

The suspension analysis in Section 7.5.5 describes the kinematics of the car as a function of suspension's motion. Computable quantities include the front- and rear-axle ride heights and the car's roll angle. These quantities are illustrated in Figure 7.27. The axle roll angles are computed as the wheel height difference divided by the axle track, while the heave is computed as the average height. If the suspension analysis is included in the car model, (7.132) can be replaced by the rigid-body assumption

$$\phi_f = \phi_r, \quad (7.156)$$

where ϕ_f and ϕ_r are the roll angles at the front and rear axles.

In race cars, where aerodynamic wings are allowed, an important suspension influence relates to the vehicle's aerodynamic performance. In the case of hard suspensions, such as those used in race cars, suspension movements are 'small' and 'nearly linear' models can be used. Table 7.1 shows how the front- and rear-axle ride heights and roll

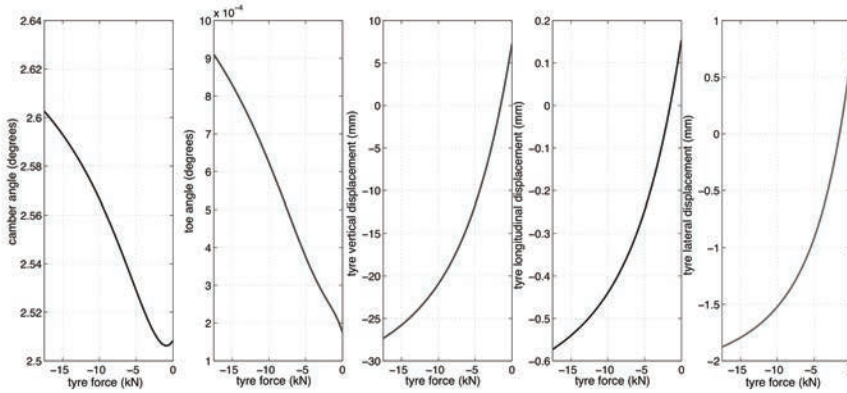


Figure 7.26: Variations in the front-left wheel carrier camber angle ϕ in (7.144), toe angle ψ in (7.144), and the ground-contact point as a function of tyre vertical load F_{flz} .

angles vary with left- and right-wheel normal loads F_l and F_r ; in the case given, only linear and quadratic terms in the normal loads are required to describe the suspension motion [270]. More complex meta models may be derived that give suspension motions as a function of the longitudinal and normal tyre forces.

The external forces acting on the car come from the tyres and from aerodynamic influences. A dynamic car model can be used to compute the normal tyre loads $F_{rrz} \cdots F_{flz}$, and the steering and side-slip angles δ and $\beta = \arctan(v/u)$, respectively. As shown in Figure 7.28, these data are supplied to the suspension and aero models to produce the aerodynamic coefficients, which are then dynamically updated. The front- and rear-axle downforce coefficients are given by C_L^f and C_L^r respectively, while the drag coefficient is C_D .

The aerodynamic downforces in (7.129) and (7.131) are computed using

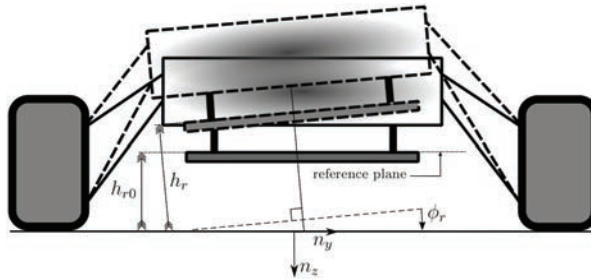


Figure 7.27: Suspension-induced roll angle ϕ_r and ride height h_r at the rear axle; the car is driving into the page and into a right-hand bend. The rear-axle ride height in the nominal configuration is h_{r0} and is measured relative to the reference plane (fixed in the car).

Table 7.1 Multivariate polynomial coefficients (meta model) of the front- and rear-axle ride height (in mm) and roll angle (in rad). The left- and right-wheel normal loads F_l and F_r , respectively, are given in kN.

	1	F_l	F_r	F_l^2	$F_l F_r$	F_r^2
h_f	-21.52	-2.513	-2.513	-0.08324	0.1126	-0.08324
ϕ_f	0	0.00851	-0.00851	0.000256	0	-0.0002562
h_r	-89.04	-4.1305	-4.1305	-0.09450	0.1119	-0.09450
ϕ_r	0	0.0112	-0.0112	6.1×10^{-05}	0	-6.1×10^{-05}

$$F_{az}^f = \frac{1}{2} \rho C_L^f A u^2, \quad (7.157)$$

and

$$F_{az}^r = \frac{1}{2} \rho C_L^r A u^2, \quad (7.158)$$

which are applied at the centres of the front and rear axles, while the drag force in (7.116) is given by

$$F_{ax} = -\frac{1}{2} \rho C_D A u^2, \quad (7.159)$$

which is applied in the rod plane. In (7.157), (7.158), and (7.159) A is the car's frontal area, ρ is the air density, and u is the air velocity over the car. The drag has a negative sign, since it acts in the negative x -axis direction. The drag and downforce coefficients are typically derived from track and wind-tunnel measurements, with representative values given in Table 7.2.

Table 7.2 Downforce and drag coefficients and sensitivities.

C_L^f	C_L^r	C_D	Input
1.2000	0.9494	0.9455	Nominal Value
10.0000	1.0000	0.1000	h_f (m)
-5.0000	-22.2222	-0.1000	h_r (m)
0	-222.2222	0	h_r^2 (m ²)
-5.1294	-10.2588	0	β^2 (rad ²)
-0.1641	-0.1641	0	δ^2 (rad ²)
-8.2070	-32.8281	0	ϕ^2 (rad ²)

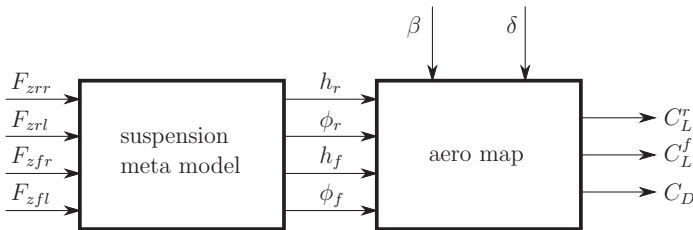


Figure 7.28: Quasi-static aero-suspension model. The dynamic model generates the normal tyre loads, and the steering and side-slip angles, while the quasi-static suspension model generates the aerodynamic drag and downforce coefficients.

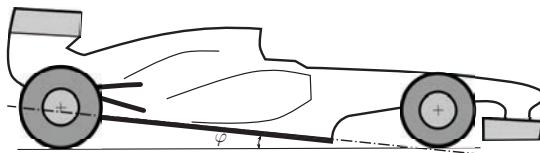
Example 7.5 Consider a race car with mass $m = 660$ kg, wheelbase $w = 3.4$ m, and with the centre of mass $b = 1.6$ m from the rear axle. Compute the ride heights and the drag and lift coefficients at standstill using the data given in Tables 7.1 and 7.2. Repeat the computation when the loads on the front and rear tyres increase by 3.330 kN and 3.142 kN respectively; the total downforce is twice the weight of the car. Finally, compute the effect of a side-slip angle of $\beta = 6^\circ$ and a roll angle of $\phi_f = \phi_r = 2^\circ$ on the drag and lift coefficients. At standstill, the normal loads on the front and rear tyres are $F_{flz} = F_{frz} = -1.523$ kN and $F_{rlz} = F_{rrz} = -1.713$ kN, respectively, which gives ride heights of $h_f = -14$ mm and $h_r = -75$ mm at the front and rear axles respectively. The corresponding drag coefficient is $C_D = 0.95$, while the front- and rear-axle down-force coefficients are $C_L^f = 1.44$ and $C_L^r = 1.35$ respectively. When downforce effects are included, the loads increase to $F_{flz} = F_{frz} = -4.853$ kN and $F_{rlz} = F_{rrz} = -4.855$ kN, the ride heights reduce to $h_f = +1.6$ mm¹⁹ and $h_r = -51$ mm, and the drag remains $C_D = 0.95$, while the lift coefficients become $C_L^f = 1.47$ and $C_L^r = 1.51$. A side-slip angle of 6° reduces the down-force coefficients to $C_L^f = 1.41$ and $C_L^r = 1.39$, while an additional 2° roll angle reduces the lift to $C_L^f = 1.40$ and $C_L^r = 1.35$.

7.6 Driver modelling

In certain scenarios, particularly in the case of motorcycles, it is necessary to augment the vehicle model with some form of driver/rider representation. Examples include driving ‘on the limit’ in racing, the stabilization of motorcycles in low-speed manoeuvring, and obstacle avoidance. There are three main physiological functions that characterize a driver’s steering response that we will now discuss: (i) the cognitive response of the brain, (ii) the muscle-related stretch reflex response, and (iii) the purely passive (intrinsic) response [199].

The cognitive response is related primarily to the driver’s path-following role and comprises two parts: the feedforward steering action based on the previewed road path and the learned vehicle behaviour, and a feedback steering action based on the vehicle’s sensed motion. From the control point of view, the use of a receding horizon strategy with both linear quadratic (LQ) preview control (e.g. [272] and [273, 274] for

¹⁹ The ride height is computed with respect to a reference plane that is attached to the vehicle chassis; this zero-height datum is shown as a dot-dash line in the sketch below:



Below the reference plane is a ‘plank’ (shown brown), which must be 10 mm thick (drawing 7 in [271]). The lower surface of the plank is at a height of +10 mm, which is still above the road surface. As soon as the car pitches forward, through angle φ , say, the reference plane can lie ‘under’ the road at the front axle, but the car’s bodywork is designed to avoid physical contact with the road under these circumstances. A ride height of zero does not mean that the front of the car is under the road.

cars and motorcycles respectively), and model predictive control (MPC) (e.g. [275] and [276, 277] for cars and motorcycles respectively) have been shown to be effective for the simulation of the path-following task. Indeed, the driver/rider action of these controllers consists of a feedforward component and a feedback component. While the feedforward component is open loop, whose frequency content can reach significant values, the feedback component has limited bandwidth (1–2 Hz) due to the brain processing time [278]. It is likely that the vehicle driver uses the noisy sensed signals to estimate the current vehicle state in order generate the feedback control. An attempt at modelling the effect of human sensory noise on path-following steering control has been reported in [279]. Another option is to deal with the cognitive response using a nonlinear optimal control framework; such approach is discussed in Chapters 8 and 9. Proportional integral derivative (PID) controllers have been used as well [280], but are generally not suitable for demanding manoeuvres, where path following is combined with significant speed variations (e.g. hard braking into a curve), especially in the case of motorcycles.

The driver stretch reflex response and the passive response—the so-called neuromuscular-system dynamics (NMSD)—are important when it comes to both vehicle stability (especially in the case of two-wheeled vehicles) and to the study of sophisticated steering manoeuvres (especially in the case of four-wheeled vehicles). In the case of motorcycles, NMSD describe the effects of holding the handlebars. Driver–vehicle stability properties ‘hands-on’ are different from driver–vehicle stability properties ‘hands-off’, especially in the case of motorcycles, as will be discussed in Section 7.7.9. In [281] and [200] the NMSD of car drivers and motorcycle riders have been identified in terms of transfer functions $\mathbf{H}(s)$ between the steering torque $T(s)$ and the steering angle $\delta(s)$; $\mathbf{H}(s) = \delta(s)/T(s)$. In the frequency range of interest (up to 10 Hz), the driver–car system $\mathbf{H}_c(s)$ exhibits one resonance, while the rider–motorcycle system $\mathbf{H}_m(s)$ presents two resonances. For cars, a single-degree-of-freedom system model is deemed sufficient (the steering rotation being the only significant degree of freedom), while in the case of motorcycles a model with at least two degrees of freedom is required (steering and the rotation of the torso about the spine; see Figure 7.29). The following expressions can be used

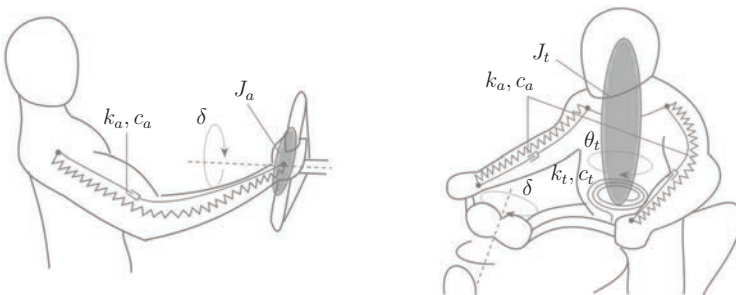


Figure 7.29: Car driver (left) and motorcycle rider (right).

$$\mathbf{H}_c(s) = \frac{1}{J_a s^2 + c_a s + k_a} \quad \mathbf{H}_m(s) = \frac{J_t s^2 + (c_t + c_a) s + (k_t + k_a)}{(J_t s^2 + c_t s + k_t)(c_a s + k_a)}. \quad (7.160)$$

The steering torque is computed at the interface between the driver's hands and the steering wheel/handlebar and so the inertia of the steering system is not included in (7.160). Moreover, in \mathbf{H}_c all the driver inertia involved in the vibration dynamics (mainly that of the arms and hands) is accounted for in J_a , which experiences the steering rotation δ , while in \mathbf{H}_m all the rider's inertia (mainly the torso) is accounted in J_t , which experiences rotation θ_t . Average driver properties are available for both cases, both in relaxed and tensed condition for the car driver, and only in the relaxed condition for the motorcycle rider [199, 200, 281]; Table 7.3. When comparing the transfer functions, it is evident that both systems have spring-like behaviour at low frequency, although the static gains ($1/k_a$ and $(k_t + k_a)/k_t k_a$) are significantly different; the gain of the car driver in a tensed condition is close to that of the motorcycle rider in a relaxed state. Different muscles are involved in each system; the car driver is mainly excited in the roll axis, while the motorcycle rider is mainly excited in the yaw axis (Figure 7.29). Also, the radius of the steering wheel is smaller than the distance between the hand grips on the handlebar and the steering axis. The main $\mathbf{H}(s)$ resonance, for the given dataset, is at 0.81 Hz for the relaxed car driver and 3.89 Hz for the tensed driver, while the motorcycle rider has a damped resonance at 1.62 Hz.

It is possible to separate the stretch-reflex response from the passive response. It is evident that when the driver is completely relaxed, there is no control input from the limb dynamics; think of an unconscious person whose arms can be moved without significant resistance. In contrast, a conscious person is able to control the position of their limbs, by activating the cognitive and stretch-reflex responses. The reflex response is related to the difference between the desired and current limb configurations, with a limit in the reconfiguration bandwidth of approximately 3 Hz [278]. It is assumed that the reflex response is activated by the difference between the desired and current steering angles. The investigation in [278] highlights the fact that the passive (intrinsic) muscle response is damper-like. Putting aside the cognitive control, it is assumed that all of the spring-like limb responses arise from stretch-reflex action, while the rest is passive. A general structure for a vehicle-driver model can be found in [199].

In the case of motorcycles, an additional stretch-reflex/passive element of the rider's response is related to the lateral and roll dynamics. Following the above arguments, these dynamics can again be modelled restraining the rider's lateral and roll motions with (properly tuned) spring-damper elements. Further details appear in Section 7.7.4.

Table 7.3 Average driver and rider parameters.

car driver (relaxed)	car driver (tense)	parameter	motorcycle rider (relaxed)
0.094	0.094	J_a (kgm ²)	-
0.59	1.12	c_a (Nms/m)	19.28
3.4	59.6	k_a (Nm/rad)	1053.4
-	-	J_t (kgm ²)	0.644
-	-	c_t (Nms/m)	4.79
-	-	k_t (Nm/m)	75.8

In sum, when simulating a manoeuvre with no unexpected driver responses, the stretch-reflex dynamics are not involved, while the passive dynamics and brain are contributory. When unexpected motion and vibration are present, the stretch-reflex response is involved. In practice, when aiming at the estimation of the stability properties of a vehicle in a hands-on configuration, the (properly tuned) spring-damper elements depicted in Figure 7.29 should be included in the mathematical model; see Section 7.7.9.

An extensive review on car driver modelling can be found in [282], while bicycle and motorcycle driver modelling are reviewed in [283]. A recent review on NMSD modelling is reported in [284].

7.7 Motorcycle modelling

From a mathematical modelling perspective single-track vehicles are multibody systems and include bicycles, motorcycles, and motor scooters, all of which have broadly similar dynamic properties. Some of the early contributions to the subject are discussed in Chapter 5. While this historically important work represented a promising start, these early models are only usable in straight running at low speed, and they fail to reproduce a number of important dynamic phenomena. We will now review a number of two-wheeled vehicle modelling enhancements.

7.7.1 Tyre contact geometry

Tyre contact geometry in the context of bicycles and motorcycles is complex. This complexity stems largely from the fact that motorcycle and bicycle tyres are profiled and may operate through a large range of roll angles.

In Section 5.2.1 we showed that the pitch angle of a rigid-wheel single-track vehicle model is determined by the solution of a closed kinematic loop that derives from the need to have both wheels in contact with the ground. We will now study this kinematic loop in detail and show that the pitch angle is a function of both the roll and steer angles. This combination of rolling and steering means that the tyre contact point can move laterally and well as circumferentially over the tyre's surface. The need to solve this closed kinematic loop for the pitch angle does, in a sense, 'disappear' when suspension systems and/or tyre carcass flexibility is considered. Various tyre carcass models are discussed at the end of this section.

Rigid tyres: pitch angle kinematic loop. If the vehicle is deemed to have a stiff suspension and stiff tyres, one may wish to neglect these compliances. We will now consider the pitch-determining closed kinematic loop in detail in the case of a toroidal tyre. The 'thin disc' wheel model is captured as a special case.

Suppose that the front and rear tyres are toroidal with crown radii ρ_F and ρ_R respectively. Other parameters that determine the closed kinematic loop conditions are the front and rear tyre radii r_F and r_R , the distance u_R between the rear-wheel centre and the steer axis given by (7.186), the distance u_F between the front-wheel centre and the steer axis given by (7.185), and the distance d between the wheel centres projected on to the steer axis (7.187); Figure 7.30. The yaw-roll-pitch convention (Section 2.5) will be used for the chassis orientation.

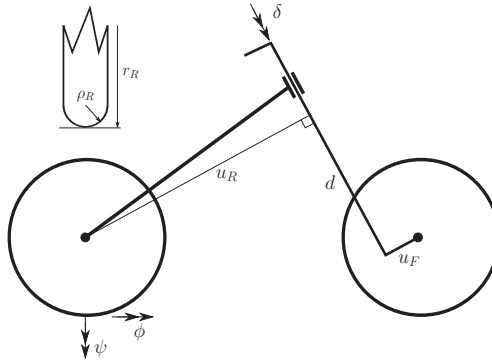


Figure 7.30: Bicycle geometry with toroidally profiled tyres.

The position of the front-wheel centre relative to the rear-wheel ground-contact point can be expressed in terms of the following eight 4×4 transformation matrices; see (Section 2.5)

$$\mathcal{T}_R = \mathcal{T}_1 \mathcal{T}_2 \mathcal{T}_3 \mathcal{T}_4 \mathcal{T}_5 \mathcal{T}_6 \mathcal{T}_7 \mathcal{T}_8 \quad (7.161)$$

where

$$\begin{aligned} \mathcal{T}_1 &= \begin{bmatrix} 1 & 0 & 0 & x_R \\ 0 & 1 & 0 & y_R \\ 0 & 0 & 1 & -\rho_R \\ 0 & 0 & 0 & 1 \end{bmatrix} & \mathcal{T}_2 &= \begin{bmatrix} \mathcal{R}(e_z, \psi) & 0 \\ 0 & 1 \end{bmatrix} & \mathcal{T}_3 &= \begin{bmatrix} \mathcal{R}(e_x, \varphi) & 0 \\ 0 & 1 \end{bmatrix} \\ \mathcal{T}_4 &= \begin{bmatrix} 1 & 0 & 0 & 0 \\ 0 & 1 & 0 & 0 \\ 0 & 0 & 1 & -(r_R - \rho_R) \\ 0 & 0 & 0 & 1 \end{bmatrix} & \mathcal{T}_5 &= \begin{bmatrix} \mathcal{R}(e_y, \chi) & 0 \\ 0 & 1 \end{bmatrix} & \mathcal{T}_6 &= \begin{bmatrix} 1 & 0 & 0 & u_R \\ 0 & 1 & 0 & 0 \\ 0 & 0 & 1 & 0 \\ 0 & 0 & 0 & 1 \end{bmatrix} \\ \mathcal{T}_7 &= \begin{bmatrix} \mathcal{R}(e_z, \delta) & 0 \\ 0 & 1 \end{bmatrix} & \mathcal{T}_8 &= \begin{bmatrix} 1 & 0 & 0 & u_F \\ 0 & 1 & 0 & 0 \\ 0 & 0 & 1 & d \\ 0 & 0 & 0 & 1 \end{bmatrix}. \end{aligned}$$

The transformation \mathcal{T}_1 is a pure translation and locates the rear-wheel crown centre vertically above the rear-wheel contact point x_R, y_R . The rotations \mathcal{T}_2 and \mathcal{T}_3 describe the vehicle's yaw ψ and roll φ , respectively.²⁰ The translation \mathcal{T}_4 positions the rear-wheel centre in an arbitrary vehicle configuration; the rear-wheel radius is r_R . The rotation in \mathcal{T}_5 recognizes the pitch rotation χ of the vehicle. The translation \mathcal{T}_6 locates the steer axis, \mathcal{T}_7 introduces a steering rotation δ , and \mathcal{T}_8 is a translation to the front-wheel centre. The rotation matrices $\mathcal{R}(\cdot, \cdot)$ have been defined in (2.156)–(2.158).

²⁰ There is no loss of generality in assuming that the rear frame is aligned with the inertial x -axis resulting in $\psi = 0$; the \mathcal{T}_2 rotation can thus be ignored.

Alternatively, starting from the front-wheel contact point, the following sequence of four 4×4 transformation matrices

$$\mathcal{T}_F = \mathcal{T}_9 \mathcal{T}_{10} \mathcal{T}_{11} \mathcal{T}_{12} \quad (7.162)$$

where

$$\begin{aligned} \mathcal{T}_9 &= \begin{bmatrix} 1 & 0 & 0 & x_F \\ 0 & 1 & 0 & y_F \\ 0 & 0 & 1 & -\rho_F \\ 0 & 0 & 0 & 1 \end{bmatrix} & \mathcal{T}_{10} &= \begin{bmatrix} \mathcal{R}(e_z, \psi_F) & 0 \\ 0 & 1 \end{bmatrix} \\ \mathcal{T}_{11} &= \begin{bmatrix} \mathcal{R}(e_x, \varphi_F) & 0 \\ 0 & 1 \end{bmatrix} & \mathcal{T}_{12} &= \begin{bmatrix} 1 & 0 & 0 & 0 \\ 0 & 1 & 0 & 0 \\ 0 & 0 & 1 & -(r_F - \rho_F) \\ 0 & 0 & 0 & 1 \end{bmatrix} \end{aligned}$$

locates the front-wheel crown centre in an arbitrary configuration. As before, the translation \mathcal{T}_9 locates the centre of the front-tyre crown, \mathcal{T}_{10} describes the yaw rotation ψ_F of the front wheel, \mathcal{T}_{11} represents the roll rotation φ_F of the front wheel, and \mathcal{T}_{12} represents the translation to the front-wheel centre.

The orientation of the front-wheel spin axis can be determined by the vector $[0, 1, 0]^T$ in frame \mathcal{T}_R , or in frame \mathcal{T}_F . These expressions must be equivalent and so

$$\mathcal{T}_R \begin{bmatrix} 0 \\ 1 \\ 0 \\ 0 \end{bmatrix} = \mathcal{T}_F \begin{bmatrix} 0 \\ 1 \\ 0 \\ 0 \end{bmatrix}. \quad (7.163)$$

The z -axis component (third row) of the two alternative vector expressions gives

$$f_1 = \sin \varphi_F = c_1 \sin \chi + c_2 \cos \chi + c_3, \quad (7.164)$$

in which

$$c_1 = \cos \varphi \sin \delta \quad (7.165)$$

$$c_2 = 0 \quad (7.166)$$

$$c_3 = \sin \varphi \cos \delta, \quad (7.167)$$

as a first constraint equation.

The height of the front-wheel centre can be computed from the (3,4) entries of the matrices \mathcal{T}_F in (7.162) and \mathcal{T}_R in (7.161). This provides a second loop constraint equation, which can be written in the form

$$f_2 = \cos \varphi_F = c_4 \sin \chi + c_5 \cos \chi + c_6 \quad (7.168)$$

where

$$c_4 = \frac{\cos \varphi (u_R + u_F \cos \delta)}{r_F - \rho_F} \quad (7.169)$$

$$c_5 = \frac{-d \cos \varphi}{r_F - \rho_F} \quad (7.170)$$

$$c_6 = \frac{\rho_R - \rho_F + \cos \varphi (r_R - \rho_R) - u_F \sin \varphi \sin \delta}{r_F - \rho_F}. \quad (7.171)$$

Following [285], the two loop equations can be combined as $(7.164)^2 + (7.168)^2$ to eliminate the left-hand-side terms in φ_F ; a quadratic expression in $\sin \chi$ and $\cos \chi$ is thereby obtained. We then use the trigonometric identities $\cos \chi = (1 - \tan^2 \frac{\chi}{2})/(1 + \tan^2 \frac{\chi}{2})$ and $\sin \chi = 2 \tan \frac{\chi}{2}/(1 + \tan^2 \frac{\chi}{2})$ to obtain

$$a_4 \left(\tan \frac{\chi}{2} \right)^4 + a_3 \left(\tan \frac{\chi}{2} \right)^3 + a_2 \left(\tan \frac{\chi}{2} \right)^2 + a_1 \left(\tan \frac{\chi}{2} \right) + a_0 = 0 \quad (7.172)$$

where

$$a_4 = (c_3 - c_2)^2 + (c_6 - c_5)^2 - 1 \quad (7.173)$$

$$a_3 = 4(c_1(c_3 - c_2) + c_4(c_6 - c_5)) \quad (7.174)$$

$$a_2 = 4(c_1^2 + c_4^2) + 2(c_3^2 - c_2^2 + c_6^2 - c_5^2 - 1) \quad (7.175)$$

$$a_1 = 4(c_1(c_3 + c_2) + c_4(c_6 + c_5)) \quad (7.176)$$

$$a_0 = (c_3 + c_2)^2 + (c_6 + c_5)^2 - 1. \quad (7.177)$$

The ‘thin’ wheel case is easily recovered from the above by setting $\rho_F = 0$ and $\rho_R = 0$ to obtain

$$c_4 = \frac{\cos \varphi (u_R + u_F \cos \delta)}{r_F} \quad (7.178)$$

$$c_5 = \frac{-d \cos \varphi}{r_F} \quad (7.179)$$

$$c_6 = \frac{r_R \cos \varphi - u_F \sin \varphi \sin \delta}{r_F}. \quad (7.180)$$

One of the earliest expressions for the pitch angle is reported in [286] that considered a single-track vehicle with ‘thin’ (knife-edge) wheels—the resulting expression was again quartic. A number of other simplified expressions have been proposed over the years. In [287] both the pitch²¹ and steer angles are assumed ‘small’, and [288, 289] assumed that the pitch angle variation is ‘small’.

Following [285], an approximated expression that is valid for small pitch variation can be obtained by expanding f_1 and f_2 as power series around the pitch angle in

²¹ More precisely, the pitch variation with respect to the nominal value.

the nominal configuration χ_0 . It follows from the loop closure expressions (7.164) and (7.168) that

$$f_1 \approx f_1|_{\chi=\chi_0} + \left. \frac{\partial f_1}{\partial \chi} \right|_{\chi=\chi_0} (\chi - \chi_0) = \sin \varphi_F \quad (7.181)$$

$$f_2 \approx f_2|_{\chi=\chi_0} + \left. \frac{\partial f_2}{\partial \chi} \right|_{\chi=\chi_0} (\chi - \chi_0) = \cos \varphi_F. \quad (7.182)$$

This gives

$$\chi = \chi_0 - \left. \frac{f_1^2 + f_2^2 - 1}{2 \left(f_1 \frac{\partial f_1}{\partial \chi} + f_2 \frac{\partial f_2}{\partial \chi} \right)} \right|_{\chi=\chi_0}. \quad (7.183)$$

Under the additional assumption that the steering angle is ‘small’, (7.183) reduces to (5.1).

Example 7.6 A numerical example is given in Figure 7.31, where the exact expression (obtained from the solution of the quartic (7.172)) is compared with the linearized expression (7.183). An inspection of Figure 7.31 shows that there is a reduction in the pitch angle χ (i.e. a lowering of the front frame), when steering in the upright position ($\varphi = 0$). When steering at a positive roll angle, the pitch angle has a minimum χ_{\min} at a positive steer angle (δ). The results have been obtained using the dataset in Table 5.1 with $\rho_R = 0.020 \text{ m}$, $\rho_F = 0.015 \text{ m}$, and $\chi_0 = 0.1\pi$.

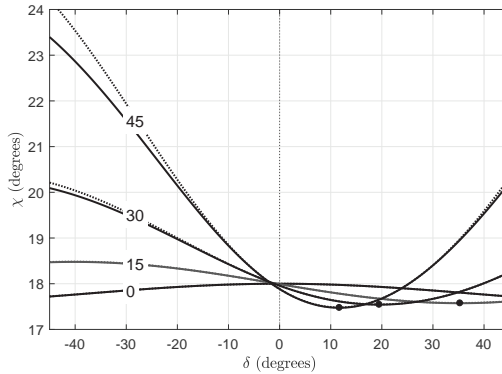


Figure 7.31: Pitch angle as a function of the steer angle δ for different roll angles φ . The exact expression given in (7.172) is shown as a continuous line, while the approximate solution (7.183) is shown dotted. The black points represent minima.

Simple relationships. In the case of the upright bike, analytical expressions for some important dependent parameters can be computed in terms of the parameters given in Table 5.1 and the sketch given in Figure 7.32.

The *normal trail* t_n is the perpendicular distance from the front-wheel ground-contact point to the steering axis and is given by

$$t_n = t \cos \lambda \quad (7.184)$$

in the vehicle's nominal configuration. The perpendicular distance between the front-wheel centre and the steering axis, sometimes called the *wheel offset*, is given by

$$u_F = r_F \sin \lambda - t_n. \quad (7.185)$$

The perpendicular distance between the rear-wheel centre and the steering axis is given by

$$u_R = (w + t) \cos \lambda - r_R \sin \lambda. \quad (7.186)$$

The distance between the wheel centres projected onto the steering axis is given by

$$d = (r_R - r_F) \cos \lambda + w \sin \lambda, \quad (7.187)$$

with a closely related parameter given by

$$p = d + r_F \cos \lambda + t \sin \lambda. \quad (7.188)$$

In the following analysis we will assume that u_r and u_F remain fixed under telescopic front fork compression/extension movements, while d and p both vary. It is clear from Figure 7.32 that

$$u_R \sin \lambda - p \cos \lambda + r_R = 0, \quad (7.189)$$

which can be solved for the angle λ , assuming a variable p , using (7.80):

$$\lambda = \arcsin \left(\frac{-r_R}{\sqrt{u_R^2 + p^2}} \right) + \arctan(p, u_R). \quad (7.190)$$

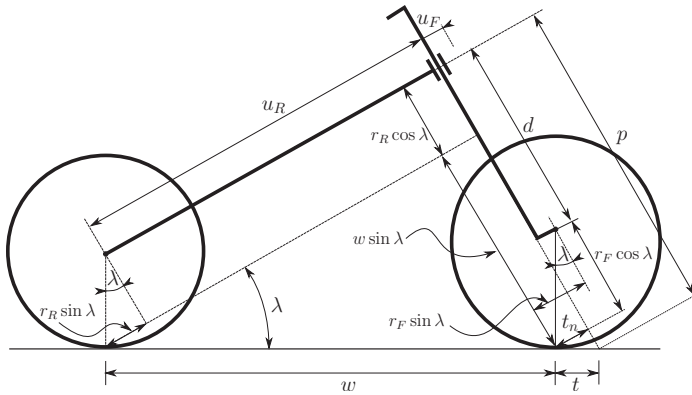


Figure 7.32: Telescopic suspension.

The resulting changes in the trail and wheelbase are given by

$$t = (r_F \sin \lambda - u_F) / (\cos \lambda) \quad (7.191)$$

and

$$w = u_r \cos \lambda + p \sin \lambda - t \quad (7.192)$$

respectively.

It is also possible to compute analytically an expression of the front-wheel yaw angle in terms of the handlebar steer angle δ and the vehicle roll angle φ . As the machine rolls and steers, the front wheel yaw angle varies according to

$$\psi_F = \arctan \left(\frac{\cos \lambda \sin \delta}{\cos \varphi \cos \delta - \sin \varphi \sin \lambda \sin \delta} \right), \quad (7.193)$$

which can be derived from the three-dimensional analysis given in Section 7.7.1 using the ratio of the (1, 1) and (2, 1) entries of (7.163).²²

Example 7.7 Using the parameters in Table 5.1, we will study the effect of telescopic fork length variations. In the vehicle's nominal configuration it is easily checked using (7.185)–(7.187) and (7.190) that $p = 0.6252$ m, $u_r = 0.9535$ m, $u_F = 0.0321$ m, $\lambda = 18^\circ$, and $d = 0.2676$ m. Figure 7.33 illustrates the effect of p variations on the steering tilt angle (a), the trail (b), and the wheelbase (c). As one would expect, each of the three variables increase, as the telescopic forks increase in length. Figure 7.33(d) shows the influence of the suspension on the kinematic steering angle, which was computed using (7.193).

Flexible tyres. The introduction of force-generating tyres marked a major advance in the modelling of road vehicles. As explained in Chapter 3, tyre force-generating properties are heavily influenced by the tyre's normal load and so in high-fidelity vehicle models these loads and their points of application (see Section 3.5.1 and Figure 3.11 (b)) have to be computed step by step as the equations of motion are solved.

There are two main modelling options when it comes to representing tyre carcass geometry and flexibility. The first introduces a spring k_n (and possibly a damper in parallel) to account for the tyre compliance in a direction normal to the road plane [290]; see Figure 7.34 (a). The second method makes use of two springs: one in the tyre radial direction k_r and one in the tyre lateral direction k_l [291]; see Figure 7.34 (b). In this case an equivalent spring stiffness k_n in a direction normal to the road surface, when the tyre has a camber angle φ , can be computed as a combination of the radial and lateral stiffness²³

$$k_n = k_r (\cos \varphi)^2 + k_l (\sin \varphi)^2. \quad (7.196)$$

²² In the case that $\lambda = 0$, (7.193) reduces to the expression of the kinematic steering angle Δ obtained with the Timoshenko–Young model in (4.76). Another commonly used expression is obtained by neglecting the second term in the denominator of (7.193) to give $\psi_F \approx \arctan \left(\frac{\cos \lambda \tan \delta}{\cos \varphi} \right)$ —the steering ‘gain’ is attenuated ($\psi_F < \delta$) when $\varphi < \lambda$, and amplified when $\varphi > \lambda$.

²³ This equivalence is readily obtained from a potential energy balance

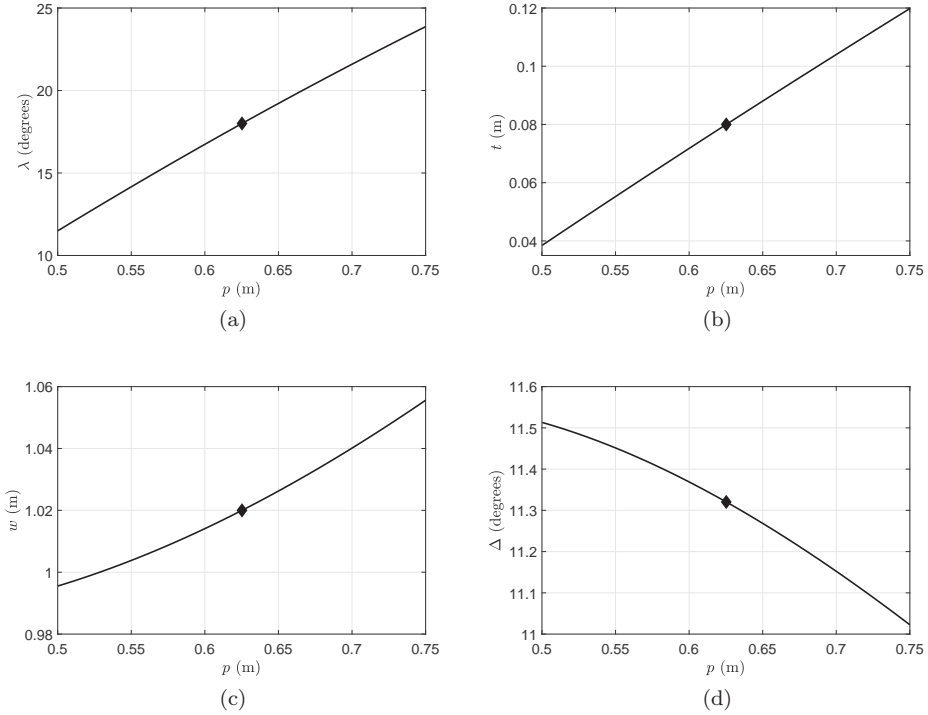


Figure 7.33: Influence of variations in p on the steering tilt angle λ (a), the trail t (b), the wheelbase w (c), and kinematic steering angle Δ for $\delta = 10^\circ$ and $\phi = 30^\circ$ (d); the nominal values are marked with a diamond. The p parameter is varied by $\pm 20\%$ of its nominal value.

In Figure 7.34 the tyre's crown centre is labelled r_{cc} , while r_{tc} represents an extensible string that represents the tyre carcass compliance; the compressed length of this spring is indicative of the normal load. It is evident that the ground-contact point r_{tc} will move to the outer extremity of the tyre as it is rolled over into a corner. In advanced models the normal load (the spring extension) is computed step by step with the aid of force and moment balances on the wheel.

To help appreciate the tyre-contact geometry in three dimensions, we make use of Figure 7.35, which shows a motorcycle tyre with lean angle φ . Point O_n is the original

$$\frac{1}{2}k_n s_n^2 = \frac{1}{2}k_r s_r^2 + \frac{1}{2}k_l s_l^2, \quad (7.194)$$

where s_r, s_l, s_n are the spring deflections in the radial, lateral, and normal directions. These deflections are related by

$$s_r = s_n \cos \varphi \quad s_l = s_n \sin \varphi, \quad (7.195)$$

which can be introduced into (7.194) to give (7.196).

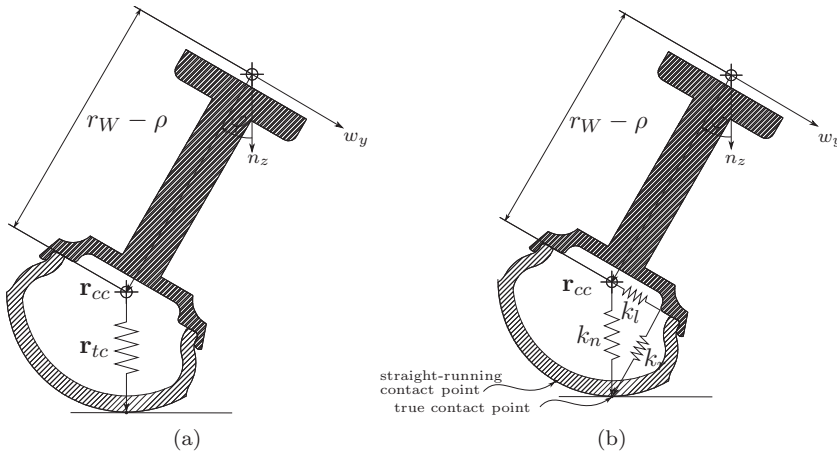


Figure 7.34: Two-dimensional tyre-to-ground contact geometry showing the lateral movement of the ground-contact point around the tyre carcass together with (a) the tyre structure represented by a vertical flexibility and (b) with radial and lateral flexibilities.

of an inertial coordinate system, with the associated orthogonal basis vectors given by \mathbf{n}_x , \mathbf{n}_y , and \mathbf{n}_z . Vector \mathbf{w}_y is a unit vector in the wheel spindle direction, while \mathbf{r}_{wl} is a vector that represents the line of intersection between the ground plane and the wheel's plane of symmetry. The first thing to observe is that

$$\mathbf{r}_{wl} = \frac{\mathbf{w}_y \times \mathbf{n}_z}{\|\mathbf{w}_y \times \mathbf{n}_z\|} \quad (7.197)$$

is a unit vector along the ground plane line of intersection; although \mathbf{w}_y and \mathbf{n}_z are unit vectors $\mathbf{w}_y \times \mathbf{n}_z$ is not. The tyre's crown centre is located by

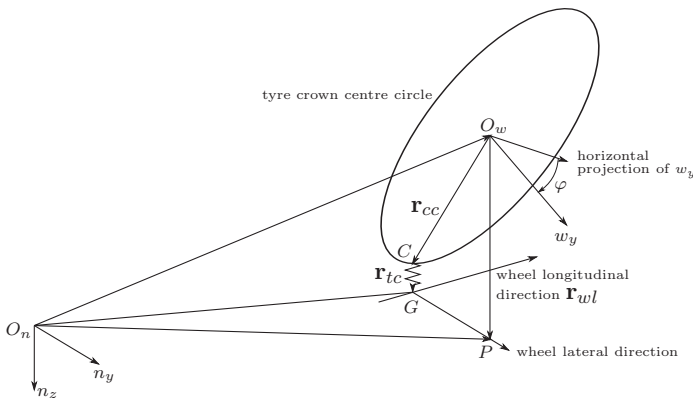


Figure 7.35: Flexible tyre ground-contact geometry.

$$\begin{aligned}
\mathbf{r}_{cc} &= (r_W - \rho)(\mathbf{r}_{wl} \times \mathbf{w}_y) \\
&= (r_W - \rho) \frac{(\mathbf{w}_y \times \mathbf{n}_z) \times \mathbf{w}_y}{\|\mathbf{w}_y \times \mathbf{n}_z\|},
\end{aligned} \tag{7.198}$$

with the ground-contact point directly below it;²⁴ this expression will be familiar from the car suspension study in (7.153).

Once the normal load and the longitudinal and lateral tyre slips are known (at each integration step), tyre models of the type given in Chapter 3 can be used to compute the tyre's force and moment system. It is important to note that with a model of the type shown in Figure 7.34 (b), there is no need to include a relaxation equation in order to account for the lagging behaviour of lateral forces. This behaviour arises automatically from the lateral spring as explained in Section 3.8.

7.7.2 Side-slipping relaxed tyres

An early attempt to introduce side-slipping and force-generating tyre models into the bicycle literature appears in [186]. Side-slipping tyres facilitate the reproduction of an important oscillatory phenomenon known as 'wobble', which is the name given to shimmy (see Section 4.5 and the discussion therein) in single-track vehicles. Relaxed tyres (Section 5.6.3), as opposed to instantaneous force-generating tyres, make an additional contribution to the accurate modelling of shimmy, allowing these oscillations to become unstable in the normal speed range [292]. Relaxed side-slipping tyres predict correctly the experimentally measured frequency of hands-off wobble, but at low and intermediate speeds (<100 kph) wobble instability is not correctly captured due to poor damping predictions. The accurate predictions of experimentally measured hands-off shimmy damping is better obtained by including frame compliance, as will be discussed in Section 7.7.3. The motorcycle model in [292] provides the minimum level of complexity required for predicting the capsize, weave, and wobble modes.²⁵ Sharp's model is reminiscent of Whipple's analysis in terms of rider modelling and the frame degrees of freedom.

7.7.3 Structural flexibility

Motivated by the known deterioration in the steering behaviour resulting from torsional compliance between the wheels, [293] extends the model of [292] by allowing the rear wheel to camber relative to the rear frame. In this model the frame flexibility freedom is constrained by a parallel spring-damper arrangement. It was found that swingarm flexibility had very little influence on the capsize and wobble modes, but reduces the weave mode damping at medium and high speeds. The removal of the damping associated with the swingarm flexibility made no material difference to these findings.

Low- and intermediate-speed-wobble mode damping has been associated with front fork compliance and shows improved behaviour with stiffer forks [294]. It is also shown

²⁴ Vectors \mathbf{r}_{wl} and \mathbf{w}_y are always orthogonal to each other and so no new normalization is required.

²⁵ The general characteristics of weave and capsize were discussed in Section 5.4.3, and those of wobble in Section 5.6.3.

in [294] that stiffening the rear frame increased the damping of the weave mode. The discrepancy between theory and experiment, with respect to the damping of the wobble mode as a function of speed, is substantially removed by the results in [295] and [296], where mathematical models are extended to include front frame compliances. The compliance of the front frame, which is a combination of the lateral bending of the fork and the torsional compliance of main frame close to the steering head, plays a key role in the stability characteristics of wobble. Stiff configurations, such as those found in sports machines, are prone to high-speed (straight-running) wobble instability, while compliant configurations are prone to low-speed wobble instability. The gyroscopic effects introduced by the frame flexibility appear to be the main wobble-stabilizing influence [84]. The analysis can be extended to include rear-frame flexibility. Bending compliance of the rear of the machine may be beneficial to high-speed weave stability, while torsional compliance is in general detrimental.

Additional contributions relating to the effect of chassis structural flexibilities on motorcycle dynamics can be found in [291, 297–299]. To model the structural properties of a motorcycle, a single lumped torsional flexibility between the front frame and the main chassis is usually employed [290, 300].

The engine-to-rear-wheel slip dynamics (i.e. the powertrain dynamics) may be influenced by structural flexibilities. These are especially important when seeking to model chatter phenomena in racing motorcycles [301–303]. These dynamics may also affect the performance of traction control systems [304, 305].

7.7.4 Rider

Unlike in cars, the rider is a substantial component of a two-wheeled vehicular system, since the ratio of the rider weight to the motorcycle weight is typically in the range 0.25–0.35. Rider movement can therefore be expected to influence the vehicle dynamics. The way the rider moves is related to the dynamics discussed in Section 7.6. In early bicycle and motorcycle models, rider dynamics were neglected and the rider is represented as an inert mass rigidly attached to the rear frame [2, 292].

One of the earliest attempts to include the rider's stretch-reflex/passive response is reported in [306, 307], where the rider's lower body is represented as an inert mass attached to the rear frame, while the upper body is represented as an inverted pendulum that has a single roll freedom constrained by a parallel spring damper arrangement.

This model has been extended to include a lateral degree of freedom in [308], which includes experimentally identified parameters of the spring-damper elements. Values vary from rider to rider, but the average values of [308] have become a reference for successive stability analyses. The results are given in terms of natural frequencies f_l and f_r , and the damping ratios ζ_l and ζ_r , from which the values of the spring k_l and k_r , and the damping constants c_l and c_r , are obtained given the rider mass and inertia:

$$k_l = (2\pi f_l)^2 m \quad c_l = 4\pi f_l \zeta_l m \quad (7.199)$$

$$k_r = (2\pi f_r)^2 (J_u + m_u h_u^2) + m_u g h_u \quad c_r = 4\pi f_r \zeta_r (J_u + m_u h_u^2). \quad (7.200)$$

The subscripts l and r are related to the lateral and roll motions respectively. The mass of the rider is m , m_u is the mass of the rider's upper body (from head to hip), J_u is the roll moment of the inertia of the rider's upper body with respect to its centre of

mass, h_u is the distance between the roll axis of the upper body and the upper-body mass centre, and g is gravity. The average frequency and damping ratio for the lateral motion are 4.0 Hz and 0.321, while for roll they are 1.27 Hz and 0.489. It is suggested that $m_u/m \approx 0.33$ and $h_u \approx 0.4 m$, although different values have been suggested by various authors.

The straight-running stability of a combined motorcycle–rider model, which focuses on the frame flexibilities and the rider’s dynamic characteristics, is studied in [308]. The frequency and damping ratios of the wobble and weave modes are calculated at various speeds and compared with results obtained from experiments conducted with four motorcycles of various sizes. It was found that the rider’s oscillatory characteristics influence both wobble and weave. The parameters relating to the rider’s upper body motion are most influential on weave, while the parameters associated with the rider’s lower body influence primarily the wobble mode. In design, given the variabilities in rider parameters that can be expected, it is important that the machine be designed to be insensitive to changes in these parameters.

Additional experimental data are reported in [309], where thirty-five different riders were tested to find the locations of their mass centres (both in normal and forward-leaning configurations), their related moments of inertia, and typical resonant frequencies and damping ratios. Natural frequencies and damping ratios for the lateral motion are in the range 3.5–4.0 Hz and 0.1–0.3 respectively, while for the roll motion the ranges are 0.8–1.5 Hz and 0.3–0.6. It was also found that the vertical location of the whole rider mass centre is (on average) 0.26 m–0.20 m from the seat surface in normal/leaned position, and from 0.09 m–0.23 m from the rider’s trochanter in a normal/leaned position. Finally, the roll moment of inertia of the whole rider is roughly proportional to the rider’s mass, the proportionality constant being in the range 0.114–0.077 for the normal/leaned configuration. In the case of the yaw moment of inertia, the proportionality constant is between 0.040 and 0.042 for the normal/leaned configuration.

An alternative to the one- or two-DOF passive rider models discussed above is the use of more sophisticated multibody models. An example is the complex rider model introduced in [310], which comprises twelve rigid bodies representing the upper and lower body, the upper and lower arms, and the upper and lower legs, with appropriate mass and inertia properties. The various rider model masses are restrained by linear springs and dampers so that rider motions such as steering, rolling, pitching, weight shifting, and knee gripping are possible. Rider control actions associated with these degrees of freedom are also modelled, using proportional control elements.

When it comes to the role of the rider as an active controller, the main input in bicycles/motorcycles is the steering torque (as opposed to the steering angle), while the body motion provides slower responses (it is used as a secondary input to assist with steering) [283, 311, 312]. At very low speeds, a stabilizing knee motion in bicycles has been observed [313].

7.7.5 Aerodynamic forces

The importance of aerodynamic forces on the performance and stability of motorcycles at high speeds was demonstrated in [314]. Wind tunnel data were obtained for the steady-state aerodynamic forces acting on a wide range of motorcycle–rider configu-

rations. It appears that the effects of aerodynamic side forces, yawing moments, and rolling moments on the lateral stability of production motorcycles are minor. However, the drag, lift, and pitching moments contribute significantly to changes in the posture of the machine on its suspension and to the tyre loads.

In [315] the effect of a handlebar fairing was examined experimentally; positive aerodynamic damping is obtained and a stabilizing effect on wobble stability was thus postulated. The effect of top boxes was investigated experimentally in [316]: the tests show that top boxes shed eddies of a fairly well-defined frequency. Resonance with the wobble frequency is possible for speeds of approximately 35 m/s, while the weave frequency is generally too low to be affected. In [317] the aerodynamic characteristics of different motorcycles were compared, while in [318] the effect of the rider was discussed.

In addition to the contributions mentioned above, there are several other more recent studies on motorcycle aerodynamics, for example [319–322]. The rider's posture usually has a significant effect on drag. In advanced applications it is common to use different drag coefficients when the vehicle accelerates (rider leaning on the tank), and when the vehicle is under braking (rider in upright position). When simulating motorcycle dynamics and stability, typically only steady-state forces are modelled. These forces significantly affect the tyre loads, which in turn influence the tyre responses and thus the vehicle stability.

7.7.6 Suspensions

The addition of suspension systems introduces two degree of freedom and two related modes, which are usually called *bounce* and *pitch*. The former is mainly a vertical translation of the chassis, while the latter is mainly a chassis pitch mode.²⁶ Adding tyre radial flexibilities into the model introduces a further two modes: *front hop* and *rear hop*. The former is mainly a front-wheel vibration along on its radial stiffness, while the latter is mainly an oscillation of the rear wheel on its radial stiffness; see Chapter 6. These modes are relatively insensitive to speed variations, and are decoupled from the out-of-plane modes (weave, wobble, and capsize) described in Chapter 5 under straight running. Variabilities, such as they are, in these in-plane modes derive from speed-dependent aerodynamic loading.

The kinematics of common motorcycle suspensions will be analysed in this section. Rear suspensions are two-dimensional single-degree-of-freedom mechanisms, while front suspensions are three-dimensional two-degree-of-freedom mechanisms. Suspension systems can be modelled directly link and joint by joint, or with the aid of a separate kinematic ‘pre-analysis’. This pre-analysis gives accurate analytic (or numerical) relationships between the suspension position and velocity, and changes in the length (and rate of change of length), of the suspension strut. Once this kinematic relationship is known, changes in the suspension position, and changes in the suspension velocity, can be used to find the restoring force/moment being applied to the wheel carrier. The relationship found in the pre-analysis can usually be replaced by

²⁶ It can be shown that the bounce is a purely vertical motion, and that the pitch is a pure rotation around the centre of mass when $k_f(w - b) - k_rb = 0$, where k_f and k_r are the front and rear suspension stiffnesses at the contact points; see Chapter 6.

an approximate functional relationship tailored to the suspension's expected range of movement; a low-order polynomial will often suffice. Direct literal modelling is the simpler approach, but it will provide equations of motion that will integrate slowly, since the simulation will have to solve the closed kinematic loop equations at each integration step.

In the case of motorcycle rear suspensions, the key issue is to determine the moment M_s applied to the swingarm pivot generated by the spring-damper force F of the suspension strut. The relationship between M_s and F can be obtained using the virtual power principle. This gives

$$M_s \dot{\theta} = F \dot{l}, \quad (7.201)$$

where θ is the swingarm rotation and l is the suspension-strut travel. Thus

$$M_s = F \left(\frac{\dot{l}}{\dot{\theta}} \right) = F \tau, \quad (7.202)$$

where τ is the *velocity ratio*. The steering of the front wheel has to be factored into the analysis when analysing the front suspension.

Cantilever rear suspension. In the simple cantilever rear suspension the suspension strut is attached between the swingarm and the chassis; see Figure 7.36. The kinematic analysis is carried out using the closed kinematic loop $p_2 p_3 p_4$. It follows from the cosine rule that

$$\begin{aligned} l_{34} &= \sqrt{l_{23}^2 + l_{24}^2 - 2l_{23}l_{24} \cos(\theta + \gamma_0 + \pi - \theta_{24})} \\ &= \sqrt{l_{23}^2 + l_{24}^2 + 2l_{23}l_{24} \cos(\theta + \gamma_0 - \theta_{24})}. \end{aligned} \quad (7.203)$$

The velocity ratio is obtained by differentiating (7.203) to obtain

$$\tau = \frac{\dot{l}_{34}}{\dot{\theta}} = -\frac{l_{23}l_{24}}{l_{34}} \sin(\theta + \gamma_0 - \theta_{24}). \quad (7.204)$$

Unitrack-like rear suspension. The Unitrack-like rear suspension is illustrated in Figure 7.37. The key feature is that the spring-damper unit (monoshock) is attached to the chassis and to the rocker $p_2 p_3 p_4$ of the four-bar linkage $p_4 p_3 p_5 p_6$.

Referring to Figure 7.37, one observes that points p_4 , p_6 , and p_7 are fixed in the main frame. The constant lengths l_2 and l_5 , and the constant angle ϕ_0 describe the geometry of a swinging link (rocker), l_3 is the length of a connecting rod that connects the swingarm to the swinging link, and l_4 is a fixed length determined by the swingarm design. The monoshock spring-damper unit has (variable) length l_1 . The angle between the swingarm axis $p_1 p_6$ and the horizontal is θ , γ_0 is the (constant) angle between l_4 and the swingarm axis, while δ describes the angular position of the swinging link.

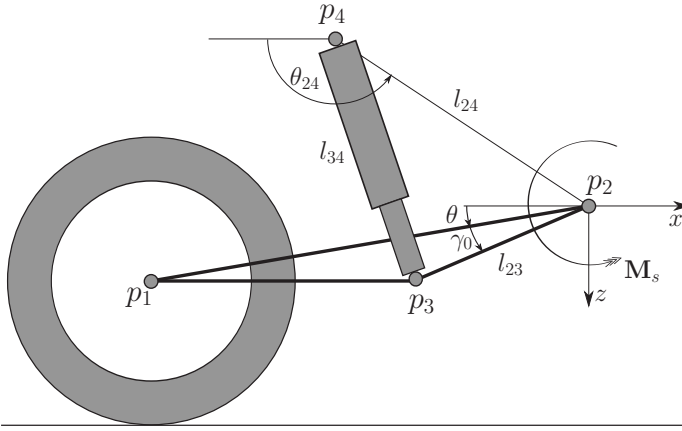


Figure 7.36: Cantilever rear suspension with the spring-damper unit connected between the chassis and swingarm.

For the closed loop $p_6-p_4-p_3-p_5-p_6$, both the x and z displacements must sum to zero. This means that

$$0 = x_4 - x_6 - l_2 \cos \delta - l_3 \cos \xi + l_4 \cos (\theta + \gamma_0) \quad (7.205)$$

$$0 = z_4 - z_6 + l_2 \sin \delta - l_3 \sin \xi - l_4 \sin (\theta + \gamma_0). \quad (7.206)$$

Also, the position of p_2 relative to the fixed point p_4 is determined by

$$x_2 = x_4 - l_2 \cos \delta + l_5 \cos (\phi_0 + \delta) \quad (7.207)$$

$$z_2 = z_4 + l_2 \sin \delta - l_5 \sin (\phi_0 + \delta). \quad (7.208)$$

Setting

$$c_1 = x_4 - x_6 + l_4 \cos (\theta + \gamma_0) \quad (7.209)$$

$$c_2 = z_4 - z_6 - l_4 \sin (\theta + \gamma_0) \quad (7.210)$$

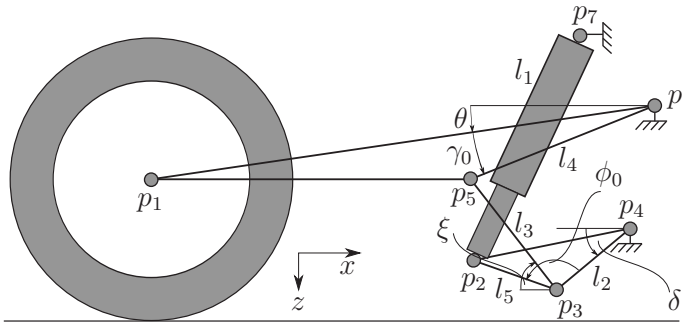


Figure 7.37: Unitrack-like rear suspension with the spring-damper unit between the chassis and the rocker of a four-bar linkage.

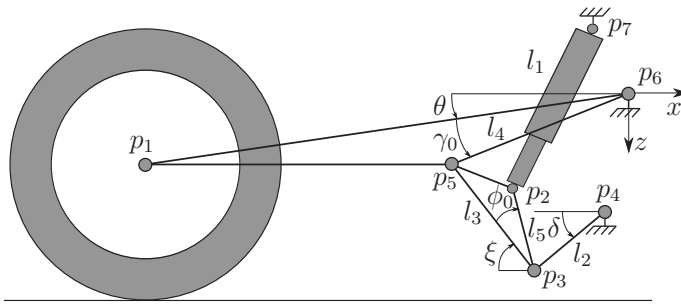


Figure 7.38: Pro-Link-like rear suspension with the spring-damper unit between the chassis and the connecting rod of a four-bar linkage.

in (7.205) and (7.206) respectively, and then squaring and adding in order to eliminate the ξ terms, gives

$$0 = c_1^2 + c_2^2 + l_2^2 - l_3^2 + 2c_2l_2 \sin \delta - 2c_1l_2 \cos \delta, \quad (7.211)$$

which can be solved using (7.80) to give the rocker angle δ as a function of the swingarm angle θ

$$\delta = \arcsin \left(\frac{-c_1^2 - c_2^2 - l_2^2 + l_3^2}{2l_2\sqrt{c_1^2 + c_2^2}} \right) + \arctan(c_1, c_2). \quad (7.212)$$

The corresponding suspension length is given by

$$l_1 = \sqrt{(x_2 - x_7)^2 + (z_2 - z_7)^2}, \quad (7.213)$$

with x_2 and z_2 given by (7.207) and (7.208) respectively; l_1 is thus a function of θ — $l_1 = l_1(\theta)$, say. The velocity ratio $\tau = \dot{l}_1(\theta)/\dot{\theta}$ can be computed by differentiating (7.213).

Example 7.8 Suppose a Unitrack suspension has the following link lengths: $l_2 = 0.040$ m, $l_3 = 0.025$ m, $l_4 = 0.051$ m, $l_5 = 0.016$ m, with point locations $x_4 = 0$, $z_4 = 0.030$ m, $x_6 = z_6 = 0$, $x_7 = 0$, $z_7 = -0.030$ m, and fixed angles $\phi_0 = 0.675$ rad, $\gamma_0 = 0.197$ rad. When the swingarm rotation is $\theta = 0$, $c_1 = 0.050$, $c_2 = 0.020$ and the swingarm link rotation (7.212) is $\delta = 0.072$ rad. The related suspension-strut length (7.213) is $l_1 = 0.059$ m, with $x_2 = -0.028$ m, $z_2 = 0.022$ m given by (7.207) and (7.208). The suspension travel can be fitted (e.g. for θ in the range 0–0.3 rad) with the second-order polynomial $l_1 \approx 10^{-2}(5.913 + 3.771\theta - 0.980\theta^2)$ to give a norm of residuals 0.002×10^{-2} m. The velocity ratio is $\tau \approx 10^{-2}(3.771 - 1.960\theta)$. The linkage is thus slightly progressive.

Pro-Link-like rear suspension. This suspension is illustrated in Figure 7.38. Its key feature is a spring-damper unit attached to the chassis and to the connecting rod $p_2p_3p_5$ of the four-bar linkage $p_4p_3p_5p_6$. The Pro-Link-like suspension system represents a variation on unitrack-like designs. The closed kinematic loop $p_6p_4p_3p_5p_6$ is identical to that of the previous suspension and (7.205) and (7.206) remain valid. In

this case, the position of attachment point p_2 relative to the fixed point p_4 is determined by

$$x_2 = x_6 - l_4 \cos(\theta + \gamma_0) + l_3 \cos \xi - l_5 \cos(\phi_0 + \xi) \quad (7.214)$$

$$z_2 = z_6 + l_4 \sin(\theta + \gamma_0) + l_3 \sin \xi - l_5 \sin(\phi_0 + \xi). \quad (7.215)$$

Squaring and adding (7.205) and (7.206) in order to eliminate the δ terms gives

$$0 = c_1^2 + c_2^2 + l_3^2 - l_2^2 - 2c_2 l_3 \sin \xi - 2c_1 l_3 \cos \xi \quad (7.216)$$

in which c_1 and c_2 are again given by (7.209) and (7.210). Equation (7.216) can be solved using (7.80) to obtain the connecting-rod angle ξ as a function of the swingarm angle θ

$$\xi = \arcsin \left(\frac{-c_1^2 - c_2^2 - l_3^2 + l_2^2}{2l_3 \sqrt{c_1^2 + c_2^2}} \right) + \arctan(c_1, -c_2). \quad (7.217)$$

The length of the spring-damper unit is again given by (7.213), with x_2 and z_2 given by (7.214) and (7.215). The suspension unit extension is thus a known function of the swingarm rotation θ , and the velocity ratio can be computed by differentiation as before.

Example 7.9 Consider a Pro-Link suspension with the same link lengths (l_2, l_3, l_4, l_5), point locations (p_4, p_6, p_7), and fixed angles ϕ_0, γ_0 as used in Example 7.8. When the swingarm rotation is $\theta = 0$, $c_1 = 0.050$ and $c_2 = 0.020$, to give a connecting-rod rotation, using (7.217), of $\xi = 1.155$ rad. The corresponding suspension length (7.213) is $l_1 = 0.059$ m, with $x_2 = -0.036$ m, $z_2 = 0.017$ m given by (7.214) and (7.215). A second-order polynomial fitting the curve with norm of residuals 0.002×10^{-2} m is $l_1 \approx 10^{-2} (5.940 + 3.813 \theta - 1.251 \theta^2)$. The related velocity ratio is $\tau \approx 10^{-2} (3.813 - 2.502 \theta)$.

Unit-Pro-Link/Full-Floater-like rear suspension. The key feature of this suspension type is a spring-damper unit that has no chassis attachment points and usually appears in the two variants illustrated in Figure 7.39.

In the case of Unit-Pro-Link-type suspensions the monoshock unit is attached between the connecting rod and the swingarm, and the kinematic analysis is almost identical to that of the Pro-Link-like suspensions. The suspension-strut length l_1 is again given by (7.213), with p_2 given by (7.214) and (7.215) and ξ given by (7.217). The only difference with respect to the Pro-Link layout is related to the point p_7 , which is no longer fixed to the chassis, but attached to the swingarm point p_7 , and this can be computed in terms of the swingarm angle as follows:

$$x_7 = x_6 - l_6 \cos(\eta_0 - \theta) \quad (7.218)$$

$$z_7 = z_6 - l_6 \sin(\eta_0 - \theta), \quad (7.219)$$

where l_6 is a constant length and η_0 is a constant angle. The velocity ratio is computed by differentiating $l_1(\theta)$ with respect to θ .

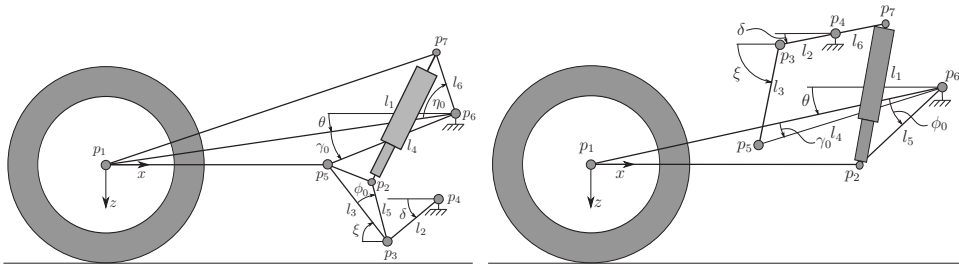


Figure 7.39: Left: rear suspension with the spring-damper unit between the swingarm and the connecting rod of a four-bar linkage (Unit-Pro-Link). Right: spring-damper between the swingarm and the rocker of a four-bar linkage (Full Floater).

In the case of fully floating rear suspension systems the suspension strut is attached between a rocker and the swingarm, and the rocker angle δ is given by (7.212). The suspension travel l_1 is defined using (7.213) with p_2 (on the swingarm) and p_7 (on the rocker) given by

$$x_2 = x_6 - l_5 \cos(\theta + \phi_0) \quad (7.220)$$

$$z_2 = z_6 + l_5 \sin(\theta + \phi_0) \quad (7.221)$$

$$x_7 = x_4 + l_6 \cos \delta \quad (7.222)$$

$$z_7 = z_4 - l_6 \sin \delta. \quad (7.223)$$

$$(7.224)$$

Equations (7.220)–(7.224) depend on the swingarm angle θ and rocker angle $\delta(\theta)$ only. Thus the spring-damper unit length l_1 is a function of θ . The velocity ratio is computed by derivation as in the previous cases.

Telescopic front suspension. Unlike the rear suspensions of two-wheeled vehicles, the front suspensions of bicycles and motorcycles are three-dimensional mechanisms; their three-dimensionality derives from the steering freedom.

An important property of motorcycle front suspensions is their *anti-dive* characteristic; see Section 7.2.2. Figure 7.40 shows the dive characteristics of the telescopic fork under study. For illustrative purposes the steering tilt angle has been increased to $\lambda = 25^\circ$ with the chassis held fixed; P is fixed in the chassis and is thus stationary. Point P_c represents the front-wheel spin axis, which moves as the suspension compresses. The variation in the front-wheel ground-contact point position is also shown. When the motorcycle undergoes braking, a load-transfer force \mathbf{F}_l and a braking force \mathbf{F}_x are produced with \mathbf{F}_R the resultant; the load-transfer angle is (7.10) (in the case that aerodynamic forces are neglected). The resultant force can be decomposed into a dive-producing force \mathbf{F}_d , which acts along the suspension's sliding axis (inclined by the support angle β_{sa}), and an orthogonal force component \mathbf{F}_\perp . This compression effect is more pronounced as the sliding axis becomes more closely aligned with the resultant force \mathbf{F}_R .

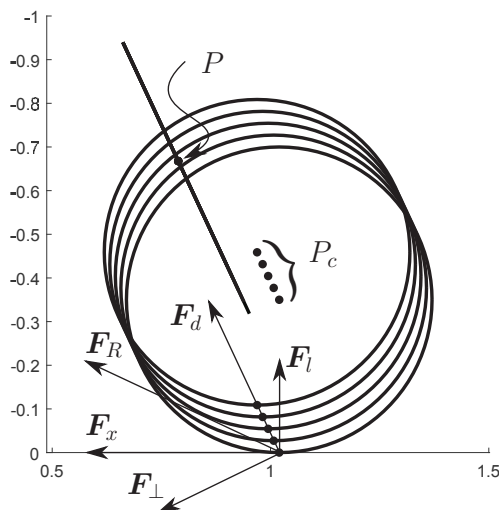


Figure 7.40: Telescopic suspension compression for $\lambda = 25^\circ$. Point P is fixed in the frame, while P_c locates the wheel centre as the suspension compresses. The load-transfer force is \mathbf{F}_l , the braking force is \mathbf{F}_x , and their resultant is \mathbf{F}_R . The diverging force is \mathbf{F}_d , and $\mathbf{F}_R = \mathbf{F}_d + \mathbf{F}_\perp$.

Duolever front suspension. The BMW Duolever front-wheel suspension is essentially a four-bar linkage, in which two trailing links are attached via revolute joints to the chassis, and by spherical joints to the wheel carrier. The suspension scheme is illustrated in Figure 7.41; R and S denote revolute and spherical joints respectively.

The trailing links steer the wheel carrier. A central suspension strut is linked to the lower trailing link at T_2 and the main chassis at T_1 . A second linkage mechanism is used to attach the four-bar linkage that supports the wheel carrier to the handlebars [323], a feature originally patented by the British inventor Norman Hossack in the 1980s. The

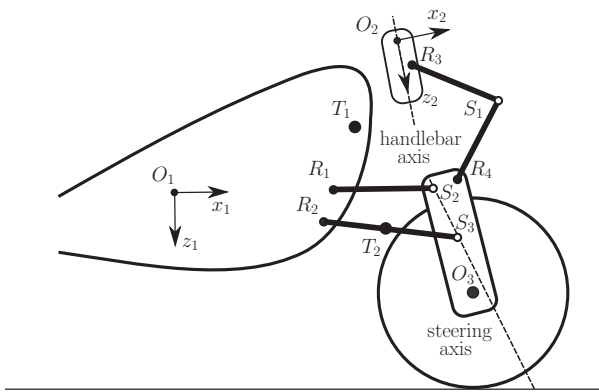


Figure 7.41: Duolever suspension scheme.

Duolever is a three-dimensional mechanism that consists of $n_B = 7$ bodies (chassis, wheel carrier, handlebar, lower rocker between R_2 and S_3 , upper rocker between R_1 and S_2 , and upper links between R_4 and S_1 and between R_3 and S_1), $n_R = 5$ revolute joints; the steering freedom represents a fifth revolute joint. There are $n_S = 3$ spherical joints as marked in Figure 7.41. The Chebychev–Grübler–Kutzbach formula [324] shows that the system has two degrees of freedom (suspension travel and steering)

$$n_{DOF} = 6(n_B - 1) - 5n_R - 3n_S = 2. \quad (7.225)$$

The idea is to ‘separate’ the steering and suspension actions, improve the torsional rigidity of the front wheel carrier, and, with a proper design layout, improve the anti-dive properties of the suspension system.

A kinematics analysis can be carried out using a chassis-fixed reference frame with origin O_1 , in which the x - and z -coordinates of R_1 and R_2 are fixed. We will also make use of a handlebar-fixed frame with origin O_2 , in which the x - and z -coordinates of R_3 are fixed, and a wheel-carrier-fixed reference frame with origin O_3 , in which the x - and z -coordinates of S_2 , S_3 , and R_4 are fixed. The point S_1 can be defined using a rotation α_3 of the constant length vector R_4S_1 in the wheel carrier frame, or with a rotation α_2 of the constant length vector R_3S_1 in the handlebar frame. The frames are defined using the yaw-roll-pitch (ψ - ϕ - μ) convention; (2.159). The position and orientation of the chassis frame are given, the position and rotation of the handlebar frame are given, but the handlebar steer angle δ and the position and orientation of the wheel carrier frame are unknown. At this stage there are nine unknowns, namely $\delta, x_3, y_3, z_3, \psi_3, \phi_3, \mu_3, \alpha_2, \alpha_3$, and as many constraints are necessary to solve the kinematic problem:

- (1) the length of the lower rocker of the four-bar linkage is constant, that is $(\mathbf{S}_3 - \mathbf{R}_2) \cdot (\mathbf{S}_3 - \mathbf{R}_2) = L_{R_2S_3}^2$; \mathbf{S}_3 and \mathbf{R}_2 are position vectors;
- (2) the lower rocker of the four-bar linkage operates in the chassis x - z plane, that is, $(\mathbf{S}_3 - \mathbf{R}_2) \cdot \mathbf{y}_1 = 0$;
- (3) a constant length for the upper rocker of the four-bar linkage, that is $(\mathbf{S}_2 - \mathbf{R}_1) \cdot (\mathbf{S}_2 - \mathbf{R}_1) = L_{R_1S_2}^2$;
- (4) the upper rocker operates in the chassis x - z plane, that is $(\mathbf{S}_2 - \mathbf{R}_1) \cdot \mathbf{y}_1 = 0$;
- (5) the absolute x -component of S_1 defined in the wheel carrier using α_3 must coincide with the absolute x -component of S_1 defined in the handlebar using α_2 ;
- (6) the absolute y -component of S_1 defined in the wheel carrier using α_3 must coincide with the absolute y -component of S_1 defined in the handlebar using α_2 ;
- (7) the absolute z -component of S_1 defined in the wheel carrier using α_3 must coincide with the absolute z -component of S_1 defined in the handlebar using α_2 ;
- (8) the steer angle δ is given;
- (9) the rotation of the lower rocker is given (alternatively the length of the suspension strut between T_1 and T_2 is given).

The resulting system of nine algebraic equations is now solved with a typical dataset, in order to highlight the main features of this suspension. Figure 7.42 (a) shows the duolever suspension in its nominal configuration. The (b) part of the figure shows

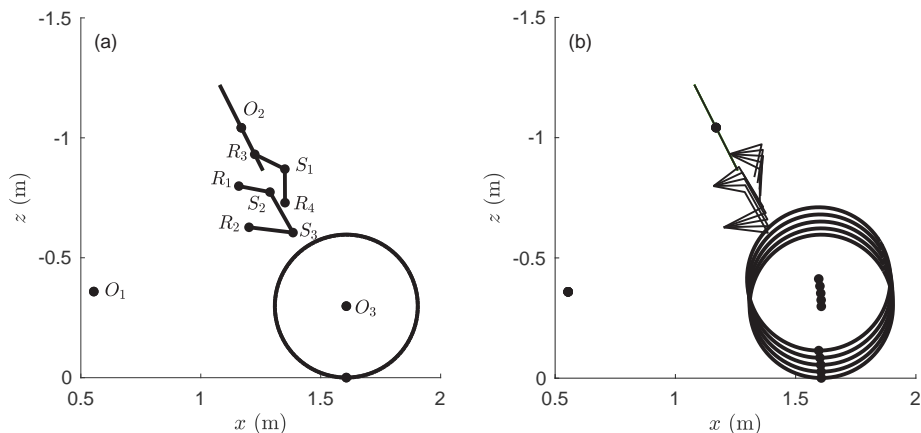


Figure 7.42: Duolever: (a) nominal configuration, (b) anti-dive effect.

the behaviour of the suspension when the steering is fixed straight ahead and the lower rocker angle is varied by 0.6 rad from the nominal configuration. The inspection of the motion of the front-tyre contact point shows an almost vertical displacement as the suspension compresses, which is related to some anti-dive behaviour—a full anti-dive configuration is achieved in the case that the direction of travel is normal to the load-transfer angle, that is, the load-transfer angle β_{lt} has the same inclination as the anti-dive line β_{sa} ; Section 7.2.2. With the duolever suspension, the steering axis is determined by S_1 and S_2 , and its castor angle increases when the suspension is compressed.

The bump steer behaviour of the Duolever is highlighted in Figure 7.43. While keeping the handlebar steer angle fixed at a prescribed value (10° in this example), a variation in the suspension travel (due to a bump or pothole, for example), results in a variation of the kinematic steer angle of the front wheel (herein defined as the yaw of

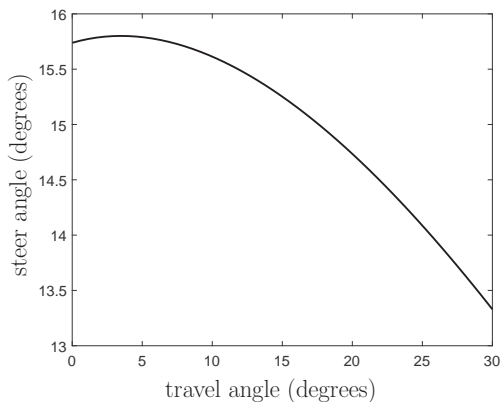


Figure 7.43: Duolever: bump steer effect at a steering angle of 10° .

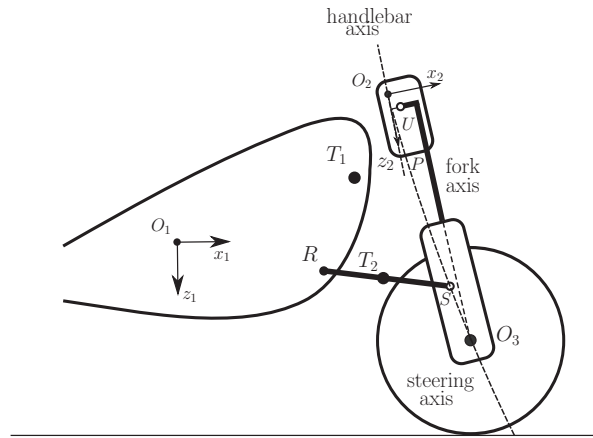


Figure 7.44: Telelever suspension scheme.

the front wheel). In a standard telescopic fork suspension, the kinematic steering angle does not vary with suspension travel when the handlebar steer angle is held fixed.

Telelever front suspension. The BMW Telelever front wheel suspension is illustrated in Figure 7.44, where R , S , P , and U ²⁷ denote revolute, spherical, prismatic, and universal joints respectively. A central suspension strut is linked to the trailing link at T_2 and the main chassis at T_1 [323].

As with a more conventional machine, wheel guidance is performed by the handlebars and fork legs. A trailing link attached to the main frame supports the forks and front wheel. A central strut (like a monoshock) is used for sprung-mass suspension and damping. This arrangement allows for an anti-dive characteristic using a simpler layout than the one required for the duolever. The telelever geometry can be designed so that the forks and front section respond minimally in dive under braking. The anti-dive properties of the suspension system and the vehicle's stability under braking result from an increase in the steering castor angle when the suspension compresses. With the telelever suspension the trail increases during braking, instead of decreasing as it does with traditional telescopic forks.

The Telelever is a spatial mechanism which consists of $n_B = 5$ bodies (chassis, lower fork, upper fork, handlebar, rocker between R and S), $n_R = 2$ revolute joints (one denoted by R , and one related to the handlebar steer axis between the handlebars and the chassis), $n_P = 1$ prismatic joint (between the upper and lower forks), $n_U = 1$ universal/Hooke joint, and $n_S = 1$ spherical joint. The Chebychev–Grübler–Kutzbach formula [324] shows that the system has two degrees of freedom (travel and steer):

$$n_{DOF} = 6(n_B - 1) - 5n_R - 5n_P - 4n_U - 3n_S = 2. \quad (7.226)$$

²⁷ The universal joint between the spherical joints connecting the upper forks and the steering assembly is introduced to simulate the kinematics of the telelever using a rigid body analysis. To work properly the 'real system' relies on the structural compliance of the wishbone–fork system.

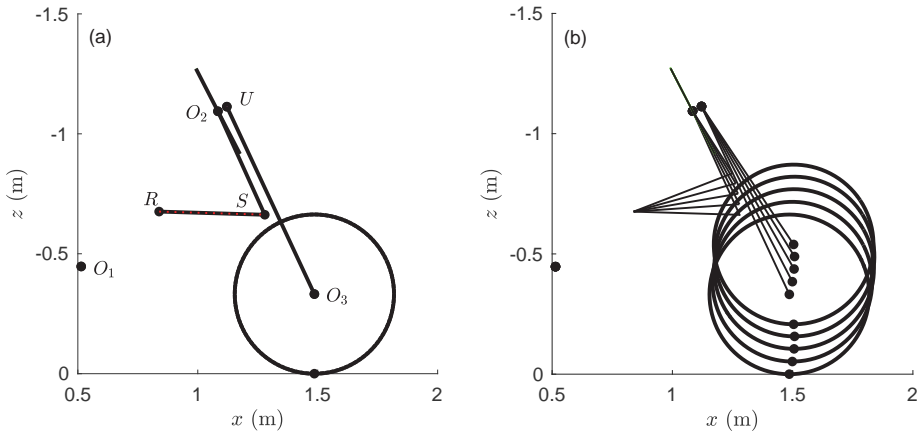


Figure 7.45: Telelever: (a) nominal configuration, (b) anti-dive effect.

A kinematics analysis can be carried out using a chassis-fixed reference frame with origin O_1 , in which the x - and z -coordinates of R and T_1 are fixed, a handlebar-fixed frame with origin O_2 , in which the x - and z -coordinates of U are fixed, and a lower-fork-fixed reference frame with origin O_3 (z_3 is aligned with the fork travel axis), in which the x - and z -coordinates of S and x -coordinate of U are fixed. The frame's angular positions are related using the yaw-roll-pitch (ψ - ϕ - μ) convention; (2.159).

The position and orientation of the chassis frame are given, the position and rotation of the handlebar frame are given, but the handlebar steer angle δ and the position and orientation of the wheel carrier frame are unknown. At this stage there are seven unknowns, namely δ , x_3 , y_3 , z_3 ; the coordinates of O_3 , ψ_3 , ϕ_3 , μ_3 and as many constraints are necessary to solve the kinematic problem:

- (1) the rocker length $(S - R) \cdot (S - R) = L_{RS}^2$ is constant;
- (2) the rocker operates in the chassis x - z plane, that is, $(S - R) \cdot y_1$ is constant;
- (3) the x -component of U in the lower-fork frame coordinate system is fixed;
- (4) the y -component of U in the lower-fork frame is fixed (and equal to zero);
- (5) universal joint U enforces $x_3 \cdot y_2 = 0$;
- (6) the steer angle δ is assumed given;
- (7) the rotation of the rocker is given (or the length of the suspension strut between T_1 and T_2 is known).

The resulting system of seven algebraic equations is now solved for a typical dataset, in order to highlight the main features of this suspension. The nominal configuration is illustrated in Figure 7.45(a). The (b) part of the figure shows the behaviour of the suspension when the steering is fixed straight ahead and the lower rocker angle is varied by 0.4 rad from the nominal configuration. The front-tyre contact point moves along an almost vertical path as the suspension compresses, which relates to the suspension's anti-dive properties; the same conclusion was drawn for the duolever suspension. In the case of the telelever, the steer axis passes through the spherical joint S and the

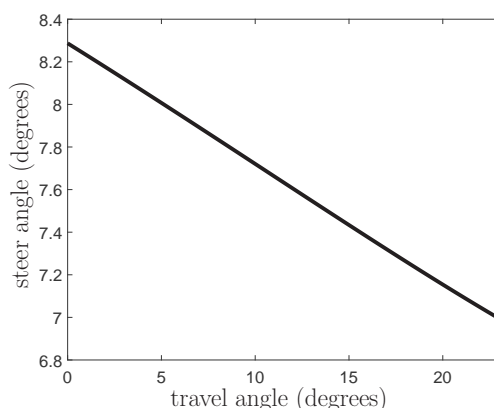


Figure 7.46: Telelever: bump steer effect at a steering angle of 10° .

projection of the point U on the steer axis. In common with the duolever, the castor angle increases when the suspension compresses.

The bump-steer effect is illustrated in Figure 7.46. When the handlebar steer angle is fixed at a given value (10° in this example), suspension travel (due to a bump or pothole) results in a variation of the kinematic steer angle of the front wheel (also defined as the yaw of the front wheel).

7.7.7 Power transmission

In motorcycles the engine power ‘flows’ from the engine crankshaft to a drive sprocket on a chassis-mounted gearbox, then to a driven sprocket that is fixed to the rear wheel, either through a chain or belt drive, or a drive shaft. Chain/belt drive transmissions are most common in the case of a transverse engine layout (crankshaft axis aligned with wheel spin axes), while shaft-drive transmission is most common with longitudinal engine layout (crankshaft axis in the symmetry plane of the vehicle). It was shown in Section 7.2.2 that these two different transmission layouts have some dynamic implications on the trim of the vehicle.

An analysis of the chain-drive transmission will be carried out in some detail, in order to obtain expressions for the contact angles of the upper and lower chain runs, which are required in order to apply chain forces in the correct direction in simulation models. These expressions are also necessary to compute the squat angles discussed in Section 7.2.2. A motorcycle chain/belt drive operates between the gearbox drive sprocket and a driven sprocket that is rigidly attached to the rear wheel; see Figure 7.47. When the chain is under tension, it places a secondary load on the swingarm and rear-wheel suspension thereby influencing the swingarm equilibrium angle and thus vehicle’s pitch angle.

Referring to Figure 7.48, it can be seen that the chain drive functions as a tension link between the points p_6 on the gearbox sprocket and the point p_4 on the rear-wheel drive sprocket when the engine is driving the rear wheel. Under engine overrun conditions (engine braking), the tension link operates between p_7 on the gearbox sprocket

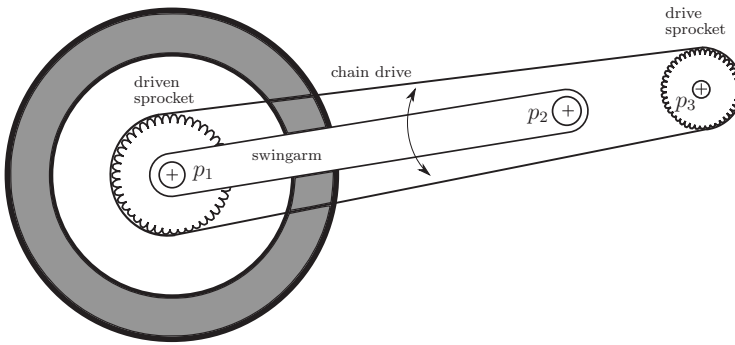


Figure 7.47: Chain drive and swingarm rear suspension. The point p_1 is the centre of the rear-wheel driven sprocket, p_2 is the swingarm pivot, and p_3 is the centre of the drive sprocket.

and p_5 on the rear-wheel sprocket. Some slack, or clearance, is allowed between driving and overrunning, and the chain is treated as elastic and damped. When building a computer model, the transmitted forces will require logic that determines whether the chain is operating under driving or overrun conditions. The points p_4 to p_7 need to be considered as moving points in the sprocket bodies, since they will rotate around their respective sprockets as the chain loading varies. When a chain section is under tension, it is perpendicular to the radial vectors defining the chain–sprocket contact points.

In the kinematic analysis it is convenient to make use of the following six vector relationships:

$$\mathbf{r}_{sa} = r_{sa} \begin{bmatrix} -\cos \theta \\ \sin \theta \end{bmatrix} \quad \mathbf{r}_{su} = r_w \begin{bmatrix} -\sin \mu_u \\ -\cos \mu_u \end{bmatrix} \quad \mathbf{r}_{du} = r_d \begin{bmatrix} -\sin \mu_u \\ -\cos \mu_u \end{bmatrix} \quad (7.227)$$

$$\mathbf{r}_{s0} = \begin{bmatrix} x_3 - x_2 \\ z_3 - z_2 \end{bmatrix} \quad \mathbf{r}_{sl} = r_w \begin{bmatrix} \sin \mu_l \\ \cos \mu_l \end{bmatrix} \quad \mathbf{r}_{dl} = r_d \begin{bmatrix} \sin \mu_l \\ \cos \mu_l \end{bmatrix}, \quad (7.228)$$

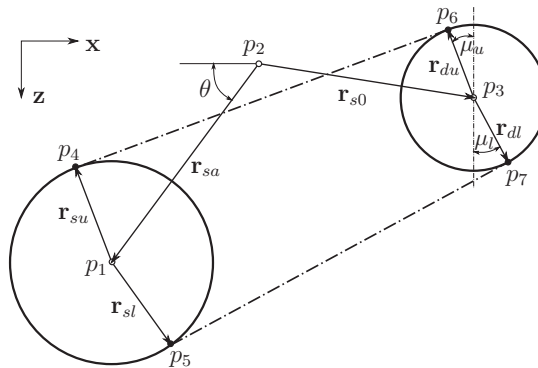


Figure 7.48: Kinematics of the chain drive and swingarm suspension. The points p_4 to p_7 represent the chain–sprocket contact points.

where r_d and r_w are the radii of the drive and driven sprockets respectively. The coordinates of point p_i are denoted (x_i, z_i) ; the coordinate y_i need not be considered, since this is a two-dimensional analysis. The top chain section is described by $\mathbf{r}_{s0} + \mathbf{r}_{du} - \mathbf{r}_{sa} - \mathbf{r}_{su}$, while the bottom chain section is described by $\mathbf{r}_{s0} + \mathbf{r}_{dl} - \mathbf{r}_{sa} - \mathbf{r}_{sl}$, and so

$$(\mathbf{r}_{s0} + \mathbf{r}_{du} - \mathbf{r}_{sa} - \mathbf{r}_{su}) \cdot \mathbf{r}_{du} = 0 \quad (7.229)$$

and

$$(\mathbf{r}_{s0} + \mathbf{r}_{dl} - \mathbf{r}_{sa} - \mathbf{r}_{sl}) \cdot \mathbf{r}_{dl} = 0. \quad (7.230)$$

It follows by direct calculation that

$$(x_3 - x_2 + r_{sa} \cos \theta) \sin \mu_u + (z_3 - z_2 - r_{sa} \sin \theta) \cos \mu_u - r_d + r_w = 0 \quad (7.231)$$

and

$$(x_3 - x_2 + r_{sa} \cos \theta) \sin \mu_l + (z_3 - z_2 - r_{sa} \sin \theta) \cos \mu_l + r_d - r_w = 0. \quad (7.232)$$

Equations (7.231) and (7.232) are in the form $A \sin(x) + B \cos(x) + C = 0$ and can be solved for μ_u and μ_l , in terms of the swingarm angle θ using (7.80). Once μ_u and μ_l have been determined, the points p_4 , p_5 , p_6 , and p_7 can be computed. When the location of the chain-sprocket contact points are known, the chain/belt force direction can be fully described.

Example 7.10 Consider the chain drive arrangement given in Figure 7.48 and suppose that the origin of the analysis coordinate system is p_2 . Suppose also that the drive sprocket has radius $r_d = 0.040$ m, and is located at $x_3 = 0.113$ m, $z_3 = 0.041$ m. The driven sprocket has radius $r_w = 0.100$ m, and is located by the vector \mathbf{r}_{sa} , which has magnitude 0.305 m and inclination $\theta = 0.552$ rad. The chain angles are determined using (7.80); (7.231) gives the angle of the upper chain run as $\mu_u = 0.155$ rad, while (7.232) gives the angle of the lower chain run as $\mu_l = 0.463$ rad. In addition, the coordinates of points p_4, p_5, p_6, p_7 are $x_4 = -0.275$ m, $z_4 = 0.061$ m, $x_5 = -0.215$ m, $z_5 = 0.249$ m, $x_6 = 0.107$ m, $z_6 = 0.002$ m, $x_7 = 0.131$ m, $z_7 = 0.077$ m.

The chain/belt force magnitude can be computed as follows. If φ_w and φ_d are respectively the wheel and gearbox sprocket angular positions, the upper chain run is in tension if $r_d \varphi_d - r_w \varphi_w > 0$. It then follows that $\delta l_u = r_d \varphi_d - r_w \varphi_w$ is the increase in separation between p_4 and p_6 , and $\delta l_u K_c + \delta l_u D_c$ determines the chain/belt force in terms of the chain/belt stiffness K_c and damping D_c . In the same way the lower chain run is in tension if $r_w \varphi_w - r_d \varphi_d > s_l > 0$, in which s_l represents the chain slack. In the overrun case the tension in the lower chain run can be determined in much the same way.

In an alternative simplified approach, when the engine torque M_e is propulsive, the upper chain run is assumed tight and the force is computed using $F_{cu} = M_d/r_d$, where $M_d = M_e \tau$ with M_d the torque at the drive shaft and τ the velocity ratio between the engine crankshaft and the drive-sprocket spin velocities. Under engine braking, the lower run is assumed tight and the related force magnitude is computed as $F_{cl} = M_d/r_d$.

7.7.8 Motorcycle multibody model

All high-fidelity motorcycle models are an evolution of the Whipple bicycle model described in Chapter 5. The new features include such things as relaxed force-generation tyres, a flexible chassis, aerodynamic forces, a rider model, front and rear suspension systems, and a chain- or shaft-drive.

A typical advanced multibody model [290, 291] has the degree of freedom shown in Figure 7.49, with the corresponding tree structure given in Figure 7.50. The tree structure describes the way in which the various model components move relative to each other. The main frame of the motorcycle is given six degrees of freedom relative to an inertial (road-fixed) reference frame. The rotational and translation freedoms are measured with respect to the inertial \mathbf{n}_x , \mathbf{n}_y , \mathbf{n}_z reference frame given in Figure 7.49. The main body has three children. The first is the swingarm that is allowed to rotate around the y -axis of a main-body-fixed reference frame at the swingarm pivot point p_6 ; see Figure 7.49. The rear wheel is allowed to spin around a y -axis fixed in the swingarm body at p_1 . Next, the upper body of the rider is allowed to rotate around the x -axis of a main-body-fixed reference system at p_9 . The third branch of the tree is a little more complicated and describes the frame flexibility, the front suspension, and the front wheel. The steered front assembly is allowed to rotate around the x' -axis of the main-body-fixed reference system x' , y' , z' at p_8 . The z' -axis is aligned with the steer axis, with the y' -axis pointing out of the page. The front-frame compliance motion around the x' axis is usually opposed by the stiff linear rotational spring and a small parallel rotational damper. Steering occurs around the z' axis and the upper and lower parts of the front suspension can translated relative to each other along the z' axis. The front wheel rotates relative to the lower steered assembly at p_7 . With this or any other model, the accuracy of the predicted behaviour will depend on effective conceptual modelling and multibody analysis, and on good parameter values [98, 200, 297, 325, 326].

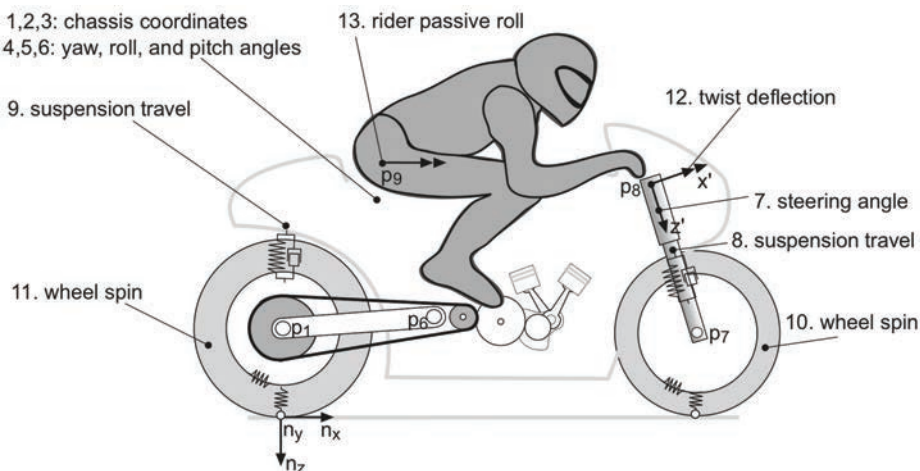


Figure 7.49: Freedoms in a typical multibody motorcycle model; the thirteen degrees of freedom are shown numbered.

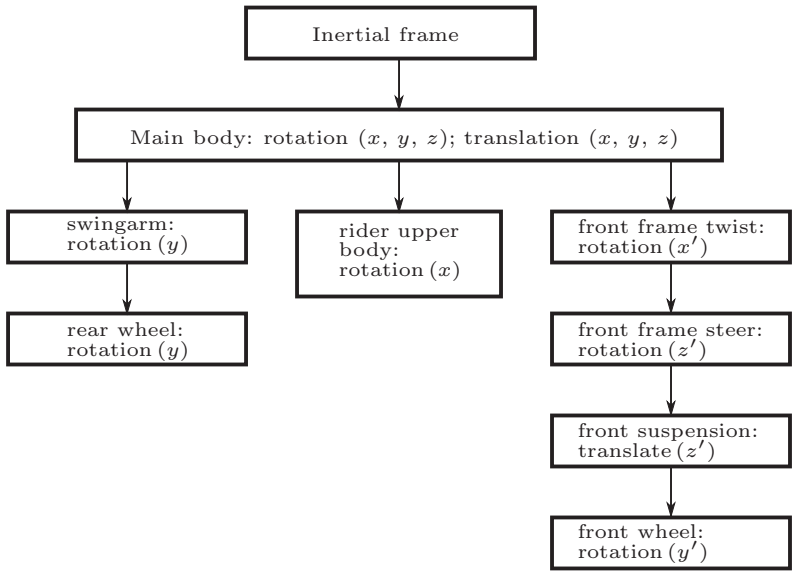


Figure 7.50: Tree structure of the multibody model depicted in Figure 7.49.

The construction of complex vehicle models is a common application of multibody codes. An example of motorcycle hands-off modes in straight running is shown in Figure 7.51 (a) for speeds from 1 to 75 m/s. The speed-dependent modes (eigenvalues) were obtained using the multibody code described in [291], and the dataset of the 1,000cc sport motorcycle reported in [290].

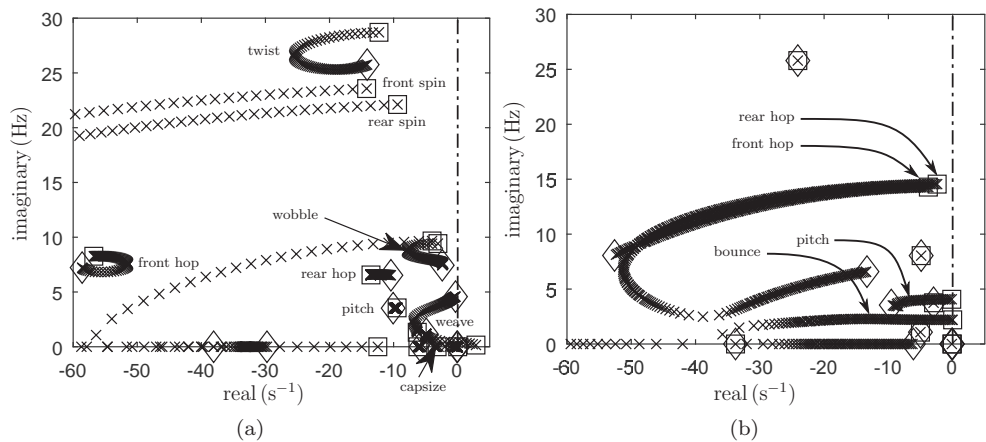


Figure 7.51: Modes of a 1,000cc motorcycle: (a) straight running when the speed is varied from 1 (squares) and 75 m/s (diamonds); (b) straight running at 35 m/s, with the suspension damping varied from zero (squares) to the baseline value (diamonds).

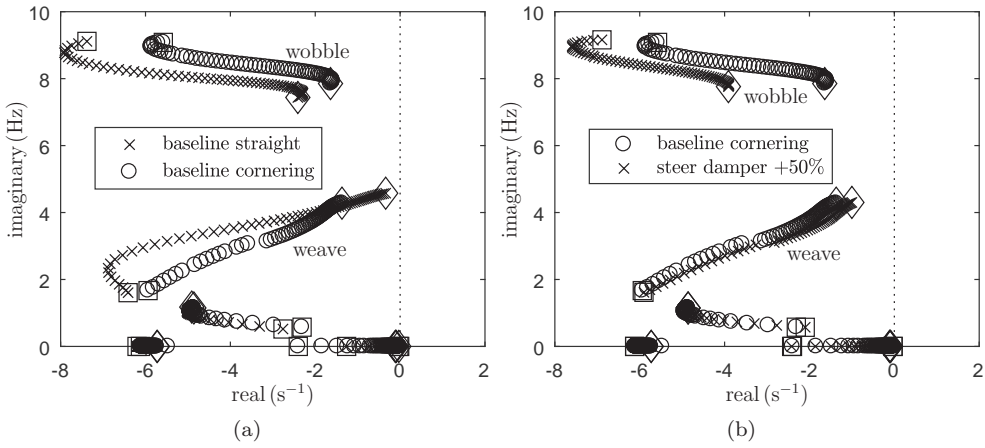


Figure 7.52: Modes of a 1,000 cc motorcycle: (a) cornering with a lateral acceleration of 0.4 g (roll angle $\approx 25^\circ$) as the speed is varied between 10 m/s (squares) and 75 m/s (diamonds); (b) cornering with a lateral acceleration of 0.4 g, with the steer damper set at baseline and 50% over baseline.

The model differential equations are a set of implicit differential equations

$$f(\dot{x}, x, u) = 0. \quad (7.233)$$

Under steady-state, these equations become

$$f(0, x_0, u_0) = 0. \quad (7.234)$$

The algebraic equations given in (7.234) can be solved to find the trim state x_0 in terms of the steady-state inputs u_0 as a function of the vehicle speed and lateral acceleration (under steady-state cornering). The equations in (7.233) can be linearized about the trim state to give the descriptor state-space equations

$$E\dot{x} = Ax + Bu, \quad (7.235)$$

where

$$E = \left. \frac{\partial f}{\partial \dot{x}} \right|_{x_0, u_0}; \quad A = \left. \frac{\partial f}{\partial x} \right|_{x_0, u_0}; \quad B = \left. \frac{\partial f}{\partial u} \right|_{x_0, u_0}. \quad (7.236)$$

The speed-dependent eigenvalues of the matrix pencil $\lambda E - A$ are shown in Figure 7.51 (a).

As shown in Figure 7.51 (a), the weave mode has a natural frequency that increases with speed from 0 to 4.5 Hz; it is unstable for speeds below 7 m/s. The damping of the weave mode then increases up to 17 m/s, and then reduces as the speed increases further. It is worth noting that the weave locus appears to separate into two branches; this is caused by the rider's roll motion in the saddle [84]. The wobble mode has modal

frequencies in the range 7.5–9.5 Hz, with minimum damping occurring at a speed of approximately 65 m/s. In this motorcycle the frequency reduces as the speed increases, but opposite trends are possible in other machines. Vehicles with minimum wobble-mode damping below 30 m/s are common. The capsize mode in this vehicle is always stable with the related locus on the negative x -axis. The front frame structural twist mode (the twelfth degree of freedom in Figure 7.49) has frequencies in the 25–28 Hz range. The front- and rear-tyre spin modes are related to circumferential vibrations in the tyre carcass coupled with the slip dynamics.²⁸ The damped natural frequency of the front-tyre spin mode decreases with speed from around 23.5 Hz (at zero speed) to approximately 22 Hz since the tyre behaves like a spring element at low speed and then like a damper when the speed increases; Section 3.8.1.

Figure 7.51 (b) focuses on the response of the four most important in-plane modes, as the front and rear suspension damping is varied from zero to the baseline value, at a speed of 35 m/s (these modes are not strongly speed dependent when the vehicle is operating in straight running). The front- and rear-wheel hop modes have low-speed frequencies of 14 and 14.5 Hz respectively, which then reduce to 8 and 6.5 Hz respectively. As the same time their damping increases as the suspension damping is increased. The bounce and pitch modes begin with frequencies of 2.2 and 4.1 Hz. The pitch frequency reduces to 3.5 Hz as the speed increases, while the bounce becomes over-damped as the damping is increased to its baseline value.

The cornering situation is considerably more complex, since in this case the in-plane and out-of-plane motions are coupled, with these interactions more prominent at large roll angles. As a consequence, several straight running modes merge together to form combined ‘cornering modes’ that require study. The early literature [327] discusses the existence of a modified weave mode that occurs under cornering conditions, when the suspension system plays an important role in its initiation and maintenance. To investigate the effect of suspension damping on cornering weave, [327] benchmarks several front and rear suspension dampers in laboratory experiments and riding tests. Motorcycle stability is found to be sensitive to suspension damping characteristics, and cornering weave instability is to some extent controllable through rear suspension damper settings. The influence of suspension damping on the weave mode is also studied both analytically and experimentally in [311]. A separate study [328] demonstrates, using a simple analysis, the possibility of interaction between pitch and weave modes at high speeds, where the lightly damped weave-mode natural frequency approaches that of the pitch mode. Although for straight running the coupling of in-plane and out-of-plane motions is weak, for steady-state cornering the coupling between the two modes increases with increased roll angle, indicating that the inclusion of pitch and bounce freedoms in motorcycle models is essential for handling studies involving cornering. The cornering experiments described in [311] quantify the influences of various motorcycle design parameters and operating conditions on wobble and weave. Tests with a range of motorcycles and riders were carried out for both straight running and

²⁸ When the engine inertia is included, the frequency of the rear-wheel spin mode reduces, because of the increase in the referred moment of inertia. The referred inertia changes with the engaged gear ratio, being maximum in first gear. A detailed analysis of these dynamics is reported in [304].

steady-state cornering. It is shown that reduced rear suspension damping, increased rear loading, and increased speed increase the tendency for the motorcycle to weave. As predicted by theory, the frequency of wobble varies little with speed, while that of weave increases with speed. Significant steps in the theoretical analysis of motorcycle cornering behaviour are documented in [306, 307, 329]. The model developed therein considers small perturbations about straight-running conditions, but also for the first time about steady-state cornering. The model is used to calculate the eigenvalues of the small-perturbation linearized motorcycle, where the results for straight running are consistent with the conventional wisdom. The way the weave- and wobble-mode characteristics are predicted as varying with speed is as expected, with front- and rear-suspension pitch and wheel-hop modes appearing that are almost independent of speed. Under cornering conditions, the interaction of these otherwise uncoupled modes produces more complicated modal behaviours. The cornering weave and combined wheel hop/wobble modes are illustrated, and root loci are plotted to observe the sensitivity of the results to parameter variations. Surprisingly, it is predicted that removing the suspension dampers hardly affects the stability of the cornering weave mode, contrary to the experiences of [311] and [327].

Under cornering, the wobble mode involves suspension movement and the previously speed-independent suspension-pitch and wheel-hop modes now vary markedly with speed. In general, interactions between weave and suspension modes, or wobble and suspension modes, occur when these modes are close in terms of their natural frequency. The coupling of the in-plane and out-of-plane motions also suggests the possibility of road excitation signals being transmitted into the lateral motions of the vehicle, causing steering oscillations [330].

An example of cornering modal behaviour is given in Figure 7.52 (a) for speeds between 10 m/s and 75 m/s and a lateral acceleration of 0.4 g. The equilibrium roll angle is approximately 25° , which is greater than the theoretical 22° because of the ‘thick’ tyres used; see Section 7.2.4. Again the dataset of [290] simulated with the multibody code [291] has been employed. Figure 7.52 (b) highlights the effect of increasing the steering damper on the cornering modes, which stabilizes the wobble whereas it destabilizes the weave mode.

In addition to the multibody code FastBike [291] used in this section, there are a number of other codes specifically designed for the analysis of motorcycle dynamics, such as BikeSim[®] and MotorcycleMaker[®]. Alternatively, the motorcycle model can be created using general-purpose multibody software such as Adams[®] and Virtual.Lab Motion[®]. While time domain simulations are possible within all of the codes mentioned above, the computation of vibration modes is sometimes laborious, since most codes cannot compute the trim configuration given the speed and acceleration as was performed in this section using [291].

7.7.9 Remarks on vibration modes

Early models such as that proposed in [2], which have no suspension and non-slipping tyres, only produce weave and capsize modes. Weave involves a fishtailing motion of the whole vehicle, with frequency typically between 2 and 5 Hz, while capsize represents a non-oscillatory rolling of the vehicle. The introduction of side-slipping tyres produces

the shimmy/wobble mode, which is a steering vibration with frequency typically in the range 5–10 Hz. Modelling the relaxation behaviour of the tyres reduces significantly the stability of the wobble mode, which can now become unstable at high speeds [292]. The introduction of a twist compliance between the front frame and the chassis causes the wobble mode to become unstable at low speed (in case of high compliance) or high speed (in case of high stiffness) [84, 296]. The introduction of a frame compliance also introduces a structural mode, with frequency typically in the range 20–30 Hz. The inclusion of a passive rider roll freedom ‘breaks’ the weave mode locus into two branches and stabilizes the high-speed weave [84, 307, 308].

The introduction of suspension introduces two more degrees of freedom, which are associated with the bounce (primarily a vertical motion of the chassis) and pitch (mainly a pitch motion of the chassis plane) that have undamped natural frequencies in the range 2–4 Hz. Radial tyre flexibility adds two more modes to the model: the front and rear wheel-hop modes that have undamped natural frequencies in the range 12–24 Hz.

Powertrain compliance, between the engine crankshaft and the rear wheel, introduces a transmission chatter mode with a frequency of approximately 20 Hz. The transmission chatter mode, which involves an oscillation of the rear end of the vehicle, has been compared with experimental data in [301, 302]. In [331] chatter is associated with the structural mode arising from the twist compliance between the front frame and the chassis—in this case the oscillation is confined to the machine’s front end. In [303] the various chatter modes are modelled and simulated in a single model.

The weave and wobble modes discussed so far are ‘hands-off’ modes. When modelling the effect of rider’s hands on the handlebar, the wobble mode stabilizes significantly, while the weave mode destabilizes—recent supporting experimental findings are reported in [332] and [84].

In straight running, the out-of-plane modes (weave and wobble), and the in-plane modes (bounce, pitch, and hops) are decoupled. The out-of-plane freedoms include lateral translation, yaw, roll, and steer, while the in-plane freedoms comprise front- and rear-suspension travel, and front- and rear-tyre radial deflection.²⁹ Under cornering, the out-of-plane modes and the in-plane modes interact. In particular, the weave mode may gain a significant rear-suspension travel component, while wobble, which usually involves steer, may gain a front-suspension travel component. In addition, the in-plane modes, which are essentially independent of speed in straight running (with any variability coming from speed-dependent aerodynamic loading), become speed dependent under cornering.

We conclude with a remark relating to typical root locus patterns for a motorcycle accelerating gently from standstill. At standstill, the vehicle is unstable due to the body-capsize, and steering-capsize modes; see Section 5.4.3. Indeed, riders must put their feet on the road to prevent the vehicle from falling over. For speeds up to 6–8 m/s³⁰ the uncontrolled motorcycle is still unstable due to the unstable weave mode;

²⁹ An informative although dated video by Dunlop on weave and wobble vibration modes is available online at <https://www.youtube.com/watch?v=z3OQTU-kE2s>.

³⁰ This low critical weave speed range reflects typical motorcycle datasets.

in this speed range rider control is needed to stabilize the vehicle. In this low-speed range the weave frequency is typically between 0.2 and 0.4 Hz [333]. Above 6–8 m/s the vehicle enters a stable speed range that requires no active rider intervention; the machine remains stable with the rider's hands off the handlebars, and even with the rider out of the saddle! At increased speeds, the dynamic capsize mode may become slightly unstable (with hands off the handlebars), but this instability is easily stabilized by passive rider action. If the vehicle is properly designed, set up, and loaded, there should be no weave or wobble instability under normal riding conditions. At high speed inappropriate cargo distributions may promote poorly damped weave, while wobble may be triggered by wheel imbalance, rough road surfaces, or the absence of a steering damper. As a general rule, most parameters variations improving the stability of either the wobble or weave mode, while destabilizing the other. For example, a steer damper stabilizes wobble but destabilizes weave. In the same way hands-on riding introduces damping into the wobble mode but destabilizes the weave mode [332].